UNIVERSITÄT ZU LÜBECK

From the Institute of Medical Engineering
of the University of Lübeck
Director: Prof. Dr. rer. nat. Thorsten M. Buzug

Combining Magnetic Particle Imaging and Magnetic Fluid Hyperthermia

A novel hyperthermia insert for preclinical MPI scanners

Dissertation
for Fulfilment of
Requirements
for the Doctoral Degree
of the University of Lübeck

from the Department of Computer Sciences and Engineering

Submitted by

Huimin Wei
from Wuhan, China

Lübeck 2024

First referee: Prof. Dr. rer. nat. Thorsten M. Buzug
Second referee: Prof. Dr. Christian Hübner
Date of oral examination: November 19th, 2024
Approved for printing. Lübeck, November 28th, 2024

Abstract

Magnetic particle imaging (MPI) is a rapidly developing imaging modality, which determines the spatial distribution of magnetic nanoparticles. Magnetic fluid hyperthermia (MFH) is a promising therapeutic approach where magnetic nanoparticles are used to transform electromagnetic energy into heat. The similarities in the physical principle of MPI and MFH give rise to the potential of integration of MFH and MPI in a single device to allow for seamless switching between imaging and therapeutic modes. In an MPI-MFH platform, the field free region of an MPI scanner can serve not only for imaging diagnostics but, by adding a radio-frequency magnetic field, also for therapeutic use of the magnetic particles by heating. It enables precisely localized heating to a specific target temperature deep in the tissue via MFH. In addition, MPI provides visualization and temperature information of systemically injected magnetic nanoparticles. In this work, the design process, the manufacturing process and the integration process of a hyperthermia insert which is capable of extending a commercial magnetic particle imaging scanner with the functionality of magnetic fluid hyperthermia are presented.

The first part of this work defines the requirements and challenges of the hyperthermia insert coil topology design. The great challenge of building a hyperthermia insert for a MPI system lies in minimizing the mutual coupling effect between both systems. The electronics of the MPI system needs to be protected against the signal induced by the hyperthermia insert in the MPI receive chain. A coil topology design with self-compensation effect is proposed. The coil is composed of a heating coil and a compensation coil connected in series but wound in opposite direction. The position of the compensation winding needs to be optimized according to the field profile of the MPI scanner to achieve the optimal decoupling result. A hybrid particle swarm optimization (PSO) algorithm

with a differential evolution (DE) operator is developed for this purpose. It introduces random mutations to the particle swarm to increase the population variety, which gives it a better performance than the original PSO algorithm. An optimized winding profile of the hyperthermia insert is obtained with the hybrid method, which has 5 heating turns at −12.5 mm, −6.25 mm, 0 mm, 6.25 mm, 12.5 mm and 4 compensation turns at −58 mm, −9 mm, 60 mm, 91 mm to the FFP along the MPI scanner bore axis.

The second part of this work focuses on the construction of the hyperthermia insert from the prototype, the cooling unit to the impedance matching network. The outer diameter of the hyperthermia insert is 117 mm to fit the bore size of the MPI scanner; the inner diameter is 61 mm to fit a small rat cassette. The inductance and resistance of the insert coil is 2.9 µH and 44 mΩ respectively. At 700 kHz, the attenuation of the induced MFH signal in the MPI receive chain is −67 dB, −63 dB and −82 dB for the x, y and z channel, respectively, due to the self-compensation effect of the insert coil topology. The results of the high power tests show that the insert is capable of generating up to 10 mT magnetic field at around 700 kHz at full working power 600 W with 160 A current through the coil. The working time of the hyperthermia insert is limited by the cooling efficiency of the heating coil. Cooling capability tests show that up to 475 W the insert can work stably for 180 s. For long term working, interleaved heating is adopted with 60 s/240 s heating/cooling cycle. At 600 W, a specific absorption rate (SAR) of 190 W/g is reached with Synomag-D 70 nm nanoparticles.

The third part of this work discusses the integration process. The hyperthermia insert and the impedance matching network together with a radio-frequency power amplifier, a send filter and a receive filter are installed. For controlling and monitoring of the MFH system, inter-system commutation is established. The transfer function of the integrated system is evaluated to ensure the proper integration of all components. High power tests on the integrated system confirms that the hyperthermia insert is successfully integrated and the MFH signal in the MPI chain is handled by passive compensating and filtering. Localized MFH is validated on a phantom by selectively heating the MNP samples locates at different positions. The thermal resolution of the localized MFH is determined by the full-width-at-half-maximum (FWHM) of the spatial-dependent SAR result of a single vial MNP sample, which is 4.4 mm, 4.7 mm and 2.4 mm for the x, y and z direction. To implement the MPI-MFH system the capability of continuous

heating is extended to maximum 25 minutes for future clinical application experiments.

Kurzfassung

Die Magnetpartikel-Bildgebung (MPI) ist ein sich rasch entwickelndes bildgebendes Verfahren, mit dem die räumliche Verteilung von magnetischen Nanopartikeln bestimmt werden kann. Magnetische Hyperthermie (MFH) ist ein vielversprechender therapeutischer Ansatz, bei dem magnetische Nanopartikel verwendet werden, um elektromagnetische Energie in Wärme umzuwandeln. Aufgrund der Ähnlichkeiten von MPI und MFH besteht die Möglichkeit, MFH und MPI in einem einzigen Gerät zu integrieren, um einen nahtlosen Wechsel zwischen Bildgebung und Therapie zu ermöglichen. In einer MPI-MFH-Plattform kann der feldfreie Bereich eines MPI-Scanners nicht nur für die bildgebende Diagnostik, sondern durch Hinzufügen eines hochfrequenten Magnetfeldes auch für die therapeutische Nutzung der magnetischen Partikel durch Erwärmung genutzt werden. Sie ermöglicht eine präzise lokalisierte Erwärmung auf eine bestimmte Zieltemperatur tief im Gewebe mittels MFH. Darüber hinaus bietet MPI eine gezielte Visualisierung und Temperaturinformation von systemisch injizierten magnetischen Nanopartikeln. In dieser Arbeit werden der Designprozess, der Herstellungsprozess und der Integrationsprozess eines Hyperthermie-Einsatzes vorgestellt, der in der Lage ist, einen kommerziellen MPI-Scanner mit der Funktionalität der magnetischen Hyperthermie zu erweitern.

Der erste Teil dieser Arbeit definiert die Anforderungen und präsentiert die Herausforderungen des Designs der Spulentopologie des Hyperthermieeinsatzes. Die große Herausforderung beim Bau eines Hyperthermie-Einsatzes für ein MPI-System liegt in der Minimierung des gegenseitigen Kopplungseffekts zwischen den beiden Systemen. Die rauscharme Elektronik des MPI-Systems muss vor dem von den Hyperthermieeinsätzen in der MPI-Empfangskette induziertem Signal geschützt werden. Um dies zu erreichen wird eine Spulentopologie mit Selbstkompensationseffekt vorgeschlagen. Die Spule besteht aus einer Heizspule

und einer Kompensationsspule, die in Reihe geschaltet, aber in entgegengesetzter Richtung gewickelt sind. Die Position der Kompensationswicklung muss entsprechend dem Feldprofil des MPI-Scanners optimiert werden, um ein optimales Entkopplungsergebnis zu erzielen. Zu diesem Zweck wurde ein hybrider Algorithmus zur Particle Swarm Optimization (PSO) mit einem Operator der Differential Evolution (DE) entwickelt. Er führt zufällige Mutationen in den Partikelschwarm ein, um die Populationsvielfalt zu erhöhen, was ihm eine bessere Leistung als dem ursprünglichen PSO-Algorithmus verleiht. Mit der hybriden Methode wird ein optimiertes Windungsprofil des Hyperthermie-Einsatzes erhalten, das 5 Heizwindungen bei -12,5 mm, -6,25 mm, 0 mm, 6,25 mm, 12,5 mm und 4 Kompensationswindungen bei -58 mm, -9 mm, 60 mm, 91 mm zum FFP entlang der Bohrungsachse des MPI-Scanners aufweist.

Der zweite Teil dieser Arbeit konzentriert sich auf die Konstruktion des Hyperthermie-Einsatzes vom Prototyp über die Kühleinheit bis hin zum Impedanzanpassungsnetzwerk. Der Außendurchmesser des Hyperthermie-Einsatzes beträgt 117 mm, um der Bohrungsgröße des MPI-Scanners zu entsprechen; der Innendurchmesser beträgt 61 mm, damit eine kleine Rattenkassette hineinpasst. Die Induktivität und der Widerstand der Einsatzspule betragen 2.9 µH bzw. 44 mΩ. Bei 700 kHz beträgt die Dämpfung des induzierten MFH-Signals in der MPI-Empfangskette -67 dB, -63 dB bzw. -82 dB für den x-, y- und z-Kanal aufgrund des Selbstkompensationseffekts der Einschubspulentopologie. Die Ergebnisse der Hochleistungstests zeigen, dass der Einsatz in der Lage ist, bei voller Arbeitsleistung von 600 W und 160 A Strom durch die Spule ein Magnetfeld von bis zu 10 mT bei etwa 700 kHz zu erzeugen. Die Betriebszeit des Hyperthermie-Einsatzes wird durch die Kühleffizienz der Heizspule begrenzt. Kühlleistungstests zeigen, dass der Einsatz bei einer Leistung von bis zu 475 W 180 s lang stabil arbeiten kann. Für den Langzeitbetrieb wird eine verschachtelte Heizung mit einem Heiz- und Kühlzyklus von 60 s bis 240 s eingesetzt. Bei 600 W wird eine spezifische Absorptionsrate (SAR) von 190 W/g mit Synomag-D 70 nm Nanopartikeln erreicht.

Der dritte Teil dieser Arbeit befasst sich mit dem Integrationsprozess. Der Hyperthermieeinsatz und das Impedanzanpassungsnetzwerk werden zusammen mit einem Hochfrequenz-Leistungsverstärker, einem Sende- und einem Empfangsfilter installiert. Zur Steuerung und Überwachung des MFH-Systems wird eine systemübergreifende Kommutierung eingerichtet. Die

Übertragungsfunktion des integrierten Systems wird evaluiert, um die ordnungsgemäße Integration aller Komponenten sicherzustellen. Hochleistungstests mit dem integrierten System bestätigen, dass der Hyperthermie-Einsatz erfolgreich integriert ist und das MFH-Signal in der MPI-Kette durch passive Kompensation und Filterung verarbeitet wird. Die lokalisierte MFH wird an einem Phantom durch selektive Erwärmung der MNP-Proben an verschiedenen Positionen validiert. Die thermische Auflösung der lokalisierten MFH wird durch die Halbwertsbreite (FWHM) des ortsabhängigen SAR-Ergebnisses einer einzelnen MNP-Probe bestimmt, die 4,4 mm, 4,7 mm und 2,4 mm für die x-, y- und z-Richtung beträgt. Um das MPI-MFH-System zu implementieren, wird die Fähigkeit der kontinuierlichen Erwärmung auf maximal 25 Minuten für zukünftige klinische Anwendungsexperimente erweitert.

Contents

1 Introduction

Contents

1.1 Motivation

As an emerging imaging technique, Magnetic Particle Imaging (MPI) has shown great potential in a wide variety of fields in the last two decades since its invention. MPI makes use of the nonlinear magnetization properties of the magnetic nanoparticles (MNPs) and a selection-field concept in time-varying magnetic fields to map their spatial distribution in tissue. MPI has several advantages over the currently established imaging techniques: it is non-invasive, high spatial resolution, high sensitivity, produces real-time quantifiable images and does not rely on any ionizing radiation. Potential application scenarios including

such as oncology imaging [1], cell tracking [2], drug delivery [3] and microrobotics [4]. The first MPI scanner was built in Hamburg at the Philips Research Laboratories in 2005 [5]. In 2014, the first commercially available preclinical FFP MPI scanner (Bruker BioSpin, Germany) was presented. Recently, efforts have been made in scaling MPI to human size and multimodal applications [6, 7]. In 2019, an MPI scanner for human brain application was presented with a bore size of 19 cm to 25 cm and a field of view (FOV) of 100 mm × 140 mm [8]. As for the multimodal applications, MPI with hyperthermia has becoming an interesting research topic. Magnetic fluid hyperthermia heats nanoparticles by driving them with an alternating magnetic field. Here, MNPs are used to couple magnetic energy into the body to heat tissue via hysteresis power loss. Magnetic fluid hyperthermia is very promising for biomedical applications, which reaches from cancer treatment [9] to controlled drug delivery [10, 11, 12]. In cancer treatment, MNPs are injected into tumors and then the alternating magnetic field is applied, aiming at increasing the tissue temperature to 40–43 °C. Tumor cells have little tolerance against a sudden difference in the temperature and can consequently be destructed [13]. Besides, the temperature increase can induce cancer cell death by raising the cytotoxic effects of chemotherapy and radiotherapy [14]. Magnetic fluid hyperthermia is not only a preclinical modality but has already clinical applications [15]. MFH has recently been approved in Europe for treatment of glioblastoma (GBM) and further clinical trials have been conducted by MagForce (Berlin, Germany) to study the application of MFH for treating prostate and pancreatic cancer [16]. In the case of controlled drug delivery MFH is used as an external stimulus to trigger the drug release. The drug molecule is either attached to MNP through a linker [17] or encapsulated with MNPs in a polymeric matrix [18, 19]. When applying alternating magnetic fields, the heat generated by MNPs breaks the linker attached to the drug or formats crevices or cracks within the polymeric matrix and release the drug. Magnetic hyperthermia induced controllable drug delivery helps to minimize side effects and improving treatment efficacy [20].

The physical principles of MFH and MPI are similar, and the magnetic nanoparticles are used for both. The two modalities can be integrated in a single device to enable a new therapeutic approach which combines therapy and diagnostic imaging. Such theranostic settings can help play out the advantages of both sides and overcome the current limitation of MFH as a clinical technique. First, localized MFH can be realized with the MPI selection field. The principle

used for spatial encoding in MPI can be used to apply spatial selectivity in MFH. In other words, the MFH can be focused with previously unavailable precision through the electronically controllable field-free region (FFR) of an MPI scanner. In MFH, MNPs generate heat via hysteresis loss and the amount of heat released is defined by the area of their hysteresis loop [21]. MNPs within the FFR experience the major hysteresis loop and generate heat. MNPs outside the FFR are driven to the saturated state by the strong static field and suppress the change in magnetization of the MNPs, therefore the area of hysteresis loop vanishes and no heat will be generated. MFH is confined to smaller regions in a tunable manner. For cancer treatment, magnetic heating can be applied solely to the malignant regions and sparing healthy surrounding tissues, which may result in minimizing thermal shock in surrounding regions without affecting the beneficiary thermal outcome in the focusing region [22]. For drug delivery, an accurate manipulation of the drug release location can be achieved with localized MFH. Second, MPI serves as a guidance of the MFH treatment by providing the spatial distribution of the MNPs and enabling non-invasively temperature measurement during heating [23]. MPI allows imaging and tracking of systemically injected drug delivery vehicle—MNPs, which helps to apply MFH for initiating drug release at the correct time. The temperature deep in tissue can be determined using a multicolor MPI reconstruction approach [24]. Accurate temperature measurement is necessary in MFH therapy to prevent under- and over-treatment of tissue to ensuring successful treatment and protection of healthy tissue by avoiding overheating [25]. In short, combining an MPI-MFH platform enables a complete theranostic workflow that combines imaging, treatment prescription, and application of therapy [26].

This work dedicates to develop a MPI-MFH platform by extending a commercial preclinical MPI scanner with MFH capabilities. The specific MFH application motivates this work is the brain drug delivery. Almost every drug therapy of a disease originating in the brain faces a particular challenge: the highly specialized structure of intracerebral blood vessels hinders the effective distribution of drugs to their desired site of action in the brain. In contrast to the rest of the body, blood vessels that supply the brain with nutrients have a structure, namely the blood brain barrier (BBB) that allows extremely selective access to the brain parenchyma for only a few substances. BBB consists of endothelial cells, pericytes and astrocytes with particularly stable connections (tight junctions). As its name indicates, BBB forms a dense boundary layer around each brain blood vessel that

only very few, usually very small molecules such as glucose, can pass through it [27]. The integrity and selectivity of this blood-brain barrier is of immense physiological importance to the brain, but limits the effective delivery of drugs to a desired site of action. Systemically applied cytostatic drugs that work well elsewhere are prevented from penetrating the parenchyma, so that brain tumors are particularly difficult to treat and have a very poor prognosis.

There are a number of approaches to make the BBB permeable by chemical modifications or physical manipulations [28], for example the use of focused ultrasound. But their mechanical or chemical effect raises doubts about the integrity of the tissue, the blood vessels and the reversibility of BBB opening, which have not yet been fully dispelled. To ensure effective and gentle treatment, the overcoming of the blood-brain barrier should be noninvasive and reversible. It has recently been shown that their permeability can be reversibly altered in a temperature-dependent manner: mild heating of a few Kelvin attenuates BBB's blocking effect [29, 30]. Temperature increases of this type could be achieved by MFH in the brain. Actually, magnetic heating of the brain for cancer therapies called thermotherapy have long used oscillating magnetic fields and invasively infiltrated MNPs to induce hyperthermia in tumors [31]. By rapidly and periodically changing the magnetization of the MNPs, the MNPs release energy through the hysteresis losses into their environment in the form of heat. This control mechanism of BBB permeability using MFH is therefore considered to have a very high potential in drug dissemination in the brain [32]. Figure 1.1 shows the reversible opening of the BBB of rat brain by magnetic fluid hyperthermia.

Ideally, the opening of the blood-brain barrier with MFH should be localized as well. Once the BBB is opened, the brain is exposed to the blood, from which it is normally isolated. An accurate control of the heating area helps to minimize the entry of opportunistic pathogens to the brain and lower the immune reaction. There are not many researches report magnetic heating of brain in spatially targeted or focused manner. One method has been demonstrated is the localized opening of BBB by illuminating the skull with infrared laser, thus causing punctual heating and heat diffusion into the cortex (Figure 1.2). However, the method is invasive and the heated location is restricted to the cortical region. Another targeted method of BBB opening currently under investigation is the use of intense focused ultrasound. Here, high-energy sound waves cause microbubbles of the ultra sound contrast agent to

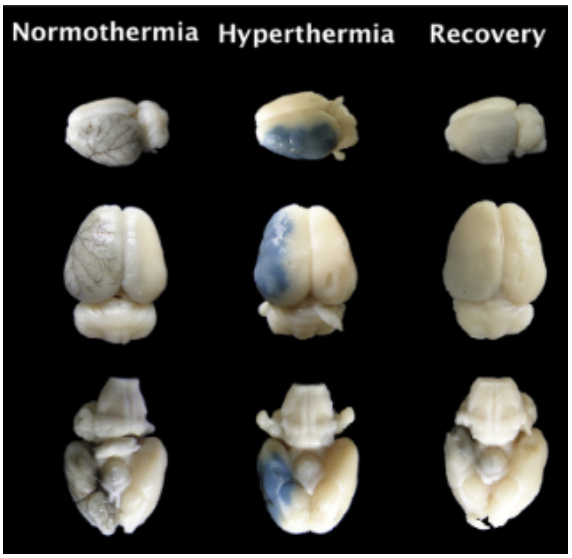

Figure 1.1: The reversible opening of the blood brain barrier when treated with hyperthermia. MNPs are injected into the brain through a catheter placed in the internal carotid artery. Normothermia: the animal was kept alive under anesthesia for 30 minutes then sacrificed, without being exposed to RF field. Hyperthermia: the animal was exposed to RF field for 30 minutes and sacrificed for brain extraction. Recovery: the animal was first exposed to RF field and recovered for 2 hours before being sacrifices. The animals received Evans Blue dye intravenously after the treatment. In normothermia group, the MNPs (black) remained inside the vasculature. In the hyperthermia group, the blue part in the brain was Evans Blue diffused into the target area, depicting a BBB breakdown. In the recovery group, there is no indication of dye diffusion nor MNP residue in the brain, showing that the BBB is able to naturally redeem full functionality and recover from magnetic heating [29].

cavitate, thereby creating mechanical stress on the tight junctions of the endothelial cells and rendering the BBB permeable there [33]. However, the nonlinear effects of sound waves radiating through the tissue and shock waves occurring at hard cranial structures are not yet fully understood [34]. Thus, the current techniques are not yet suitable for clinical applications.

The localized MFH provided by the MPI-MFH platform is an ideal solution in this scenario, it is intended to heat capillary vessels in which the nanoparticles are suspended with unprecedented precision and reversibly open the BBB at the field-free region. Along with this focused and non-invasive opening of the BBB, other substances, such as cytostatics, can then penetrate the parenchyma for a short

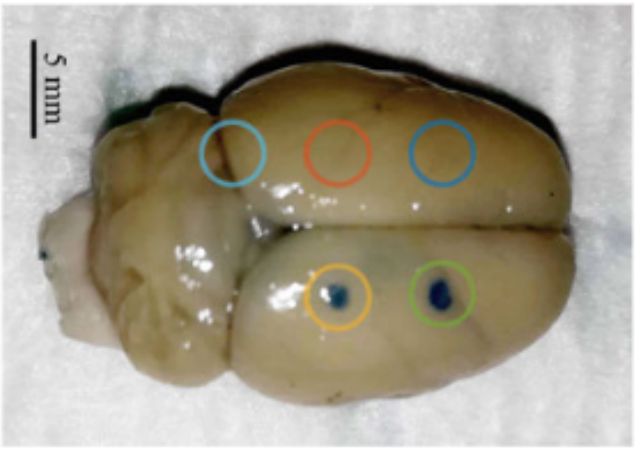

Figure 1.2: Localized opening of the blood brain barrier using IR laser [35]. The rats' cranial skull bone was exposed by incision of the skin. Five skull locations were illuminated with different laser output power (marked with circles of different color in the picture). The laser illumination procedure was completed within 5-7 minutes, after which the rat was maintained under anesthesia for one hour prior to intracardiac perfusion and brain extraction. Only the locations with the highest achieved skull temperatures (yellow and green) Evans Blue was found in the brain, indicating the BBB is opened.

period of time until tightness is restored. Furthermore, a 3D measurement of the local concentration distribution of the nanoparticles allows for accurate planning or prediction of the heating. In this work, the realization of a MPI- MFH platform and the localize MFH is presented.

1.2 Organization of this thesis

This thesis is divided into seven chapters. After this introduction, the physical principle, the signal generation and spatial coding of MPI as well as a detailed introduction into MFH are described in chapter 2. The concept of a MPI-MFH platform to combine the two modalities is proposed and discussed. This chapter provides the theory background of the work in this thesis.

Chapter 3 deals with the coil topology design of the hyperthermia insert. A special coil to generate the magnetic field for MFH with self-compensation effect is

introduced. An optimal topology of the hyperthermia insert coil is calculated according to the field characteristics of the MPI system. To optimize the coil topology, a hybrid optimization algorithm is developed based on the original particle swarm optimization. Finally, the proposed algorithm is evaluated and used to obtain the winding profile of the hyperthermia insert.

The implementation of the hyperthermia insert is discussed in Chapter 4. The manufacture of the hyperthermia insert starts with the simulation study. Afterwards, the prototype, the cooling unit as well as the impedance matching network are designed and implemented. Small signal tests are performed to evaluate the decoupling effect of coil topology and electrical properties of the and high power tests are performed to evaluate the cooling efficiency and validate the magnetic field for MFH.

Chapter 5 introduces the integration of the hyperthermia insert into the MPI system. The signal chain of the MPI-MFH system is presented at first to provide a view of all the components. The manufacture, installation of components and the inter-system communication between the MFH system and MPI scanner are discussed. The localized MFH is validated by phantom experiments with the integrated system.

The presented thesis closes with a summary, a discussion and an outlook.

1.3 Published work

Parts of this thesis have been published. The design and compatibility test of the hyperthermia insert as welll as the manufacture process of the hyperthermia insert are discussed in [P1, P2, P3]. The integration process of the hyperthermia insert is presented in [P4]. Moreover, the optimization algorithm has been presented at a conference [P5]. Further experiments on localized MFH using the MPI-MFH platform are presented in [P6]. The concept and application of the MPI-MFH platform using a hyperthermia insert is presented in review journals as well [P7, P8, P9].

2

Basic principles and background

Contents

2.1 Electromagnetism

To understand and analyze the magnetic field generated by an electrical current, the fundamentals of electromagnetism need to be discussed. In this section, the electromagnetic basics which related to the work in this thesis are introduced. The four Maxwell equations under the quasi-static approximation and the Biot-Savart law are presented. Furthermore, the interaction between coils is discussed.

2.1.1 Maxwell equations

Maxwell's equations combine three laws proposed by Gauss, Faraday and Ampére, extended by the displacement current. The four equations are:

Gauss's law:

$$\nabla \cdot \boldsymbol{D} = \rho^f \tag{2.1}$$

Gauss's law of magnetism:

$$\nabla \cdot \boldsymbol{B} = 0 \tag{2.2}$$

Faraday's law of induction:

$$\nabla \times \boldsymbol{E} = -\frac{\partial \boldsymbol{B}}{\partial t} \tag{2.3}$$

Ampére's circuital law:

$$\nabla \times \boldsymbol{H} = j^f + \frac{\partial \boldsymbol{D}}{\partial t} \tag{2.4}$$

with **D** the electric displacement, **E** the electric field strength, **H** the magnetic field strength, **B** the magnetic flux density, ρ^f the free charge density and $\mathbf{j}^f$ the free current density.

In MPI, the conditions are fulfilled that quasi-static approximation can be applied when computing the electromagnetic field as discussed in [36]. Thus, Maxwell's displacement current is neglected and Ampére's law becomes:

$$\nabla \times \boldsymbol{B} = \mu_0 \boldsymbol{j}, \tag{2.5}$$

which significantly simplifies the computation.

2.1.2 Magnetic fields

When a current flows through a wire a magnetic field is generated. Within the quasi-static approximation, the magnetic field strength $\boldsymbol{H}$ can be computed using Biot-Savart law:

$$\boldsymbol{H}(\boldsymbol{r}, t) = \frac{1}{4\pi} \int_{\mathbb{R}^3} \frac{\boldsymbol{j}^f(\boldsymbol{r'}, t) \times (\boldsymbol{r} - \boldsymbol{r'})}{\| \boldsymbol{r} - \boldsymbol{r'} \|_2^3} d^3 r' \tag{2.6}$$

Therefore the static field generated by a conductor with unit current $\widehat{I} = 1\,\text{ampere}$ and current density $\widehat{\boldsymbol{j}}^f(\boldsymbol{r})$ is given by

$$\boldsymbol{p}(\boldsymbol{r}) = \frac{1}{4\pi}\int_{\mathbb{R}^3} \frac{\widehat{\boldsymbol{j}}^f(\boldsymbol{r}) \times (\boldsymbol{r} - \boldsymbol{r'})}{\| \boldsymbol{r} - \boldsymbol{r'} \|_2^3} d^3r', \tag{2.7}$$

$\boldsymbol{p}(\boldsymbol{r})$ is defined as the coil sensitivity and can characterize the field-generating properties of an electromagnetic coil. The magnetic field strength generated by the coil can be expressed in terms of the coil sensitivity as

$$\boldsymbol{H}(\boldsymbol{r}, t) = I(t)\boldsymbol{p}(\boldsymbol{r}). \tag{2.8}$$

Since $\boldsymbol{p}(\boldsymbol{r})$ is only dependent of the coil geometry, this can be pre-calculated to realize the efficient magnetic field strength calculation at different time points.

2.1.3 Coil induction

Faraday's law of induction (Equation 2.3) indicates that the change of the magnetic field generates an electric field thus will cause a voltage induced in the coil. The voltage u^M induced by the time varying magnetization $\boldsymbol{M}(\boldsymbol{r}, t)$ in a receive coil with sensitivity $\boldsymbol{p}(\boldsymbol{r})$ is given by

$$u^{\boldsymbol{M}}(t) = -\mu_0 \int_{V^M} \frac{\partial}{\partial t}\boldsymbol{M}(\boldsymbol{r}, t) \cdot \boldsymbol{p}(\boldsymbol{r}) d^3r, \tag{2.9}$$

where V^M is the volume containing the magnetizable material and μ_0 is the vacuum permeability.

Equation 2.9 is called the law of reciprocity because it shows the reciprocal relationship between the sensitivity pattern of a receive coil and the magnetic field this coil would generate with unit current. This means that a good send coil is a good receive coil as well.

Similarly, one coil will induce voltage in another coil through the change of magnetic field strength. The voltage $u^{\boldsymbol{H}}(t)$ induced by Q send coils with volumes V_q^S and current densities $\boldsymbol{j}_q^S(\boldsymbol{r}, t) = I_q(t)\widehat{\boldsymbol{j}}_q^S(\boldsymbol{r}), q = 0, ..., Q-1$ is given by

$$u^{\boldsymbol{H}}(t) = -\frac{d}{dt}\sum_{q=0}^{Q-1} I_q(t)\xi_q, \tag{2.10}$$

where

$$\xi_q = \frac{\mu_0}{4\pi} \int_{V^R} \left(\int_{V_q^S} \frac{\widehat{\boldsymbol{j}}_q^S(\boldsymbol{r}, t)}{\| \boldsymbol{r}' - \boldsymbol{r} \|_2} d^3r \right) d^3r' \tag{2.11}$$

are the coupling factors.

This means that the send coils directly couples into the receive coil. In MPI, the induced signal at the excitation frequencies has to be suppressed to extract the higher harmonics of the particle signal. In the application of this work, the hyperthermia insert behaves similar as a send coil but with different frequency, which induces signal in the MPI receive chain as well.

2.1.4 Eddy current and skin effect

When a conductor is placed in a alternating magnetic field, electric currents are induced in the material as explained by the Faraday's law of induction. These currents, like eddies in a stream of water, flow in closed loops rather than move in straight lines, therefore are named eddy current. Eddy current causes power loss and dissipate power in the form of heat.

When an alternating current is applied on a wire, a magnetic field is induced, which in turn induces eddy current in the wire and flows in the opposite directing of the applied current by Lenz's law. The magnitude of the eddy current is proportional to the strength of the magnetic field, there is large eddy current at the center of the wire as the magnetic field generated by the applied current is maximum at the center. As a result, the total current flows through the wire is restricted to a layer close to the outer surface. In other words, the electric current is not distributed uniformly over the conductor cross section, but flows mainly at the "skin" of the conductor. This phenomenon is called the "skin effect". The current density J in a conductor decreases exponentially with increasing depth d from the surface can be calculated with

$$J = J_S e^{-(1+j)d/\delta}, \tag{2.12}$$

where J_S is the current density at the conductor surface and δ is the skin depth. The skin depth is the distance at which the current density decreases to $\frac{1}{e}$ of J_S and the formula is usually given as

$$\delta = \sqrt{\frac{2\rho}{\omega\mu}}, \tag{2.13}$$

where ρ is the resistivity of the conductor, ω is the angular frequency of current and μ is the permeability of the conductor.

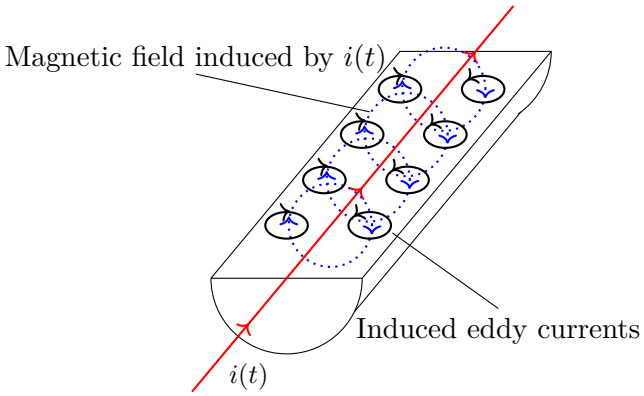

Figure 2.1: Eddy currents induced in a conductor carrying an alternating current $i(t)$.

The skin depth becomes smaller with increasing frequency, which results in a reduced conductor cross-section and therefore increases the effective resistance of the conductor for AC. At high frequencies, Litz wire is used to mitigate the skin effect. It consists of a number of single insulated wires which are twisted or braided into an uniform pattern. Each Litz wire strand has a diameter thinner than the skin depth and the strands are twisted in a way that each strand carries the same current. Therefore, Litz wire is able to minimize the high frequency losses exhibited in solid conductors caused by the skin effect and can be used in applications operating with frequencies up to hundreds of kHz [37].

2.2 Analog filters

A filter is a frequency-selective device that makes certain frequency components of a signal pass and greatly attenuates other frequency components. According to the nature of the filter signal processing, filters are divided into analog filters and digital filters. When building the MPI-MFH platform, analog filters which consists of inductors and capacitors play an important role in the signal chain of both MPI and MFH systems. The filters are used to suppress interference noise and unwanted signals in the systems using its frequency selection function. This section introduces the electrical behavior of the analog components and different types of the filters.

2.2.1 Inductor

An inductor consists of a coil by winding wire on a ferromagnetic or non-ferromagnetic core. In MPI, inductors wound on a non-ferromagnetic core (air-core) are mostly used to avoid the higher harmonics generated by the ferromagnetic core in the time varying magnetic field thus introduce distortion into the MPI signal.

The AC electrical behavior of coils is based on magnetic induction. The magnetic field generated by the current flowing through induces a reverse voltage in the coil winding. This behavior is known as self inductance. The result of self induction is that any change in the amount of current supplied to the coil is opposed by a self-induced current [38]. In practice, any conductor shows some inductance in response to the change of current. The inductance of the connection wire between components needs to be considered when designing the filters.

The inductance of a coil depends on the number of turns, radius of the coil and overall shape of the coil. The inductance of an inductor can be adjusted by changing the number of turns or the distance between each turns. The current carrying capacity of the inductor depends upon the material and thickness of the wire. The operating losses (in the form of heat) from an inductor largely depend on the material used as a core in the inductor.

Generally, for a coil of N turns, the self inductance L can be calculated with

$$L = \frac{\varepsilon}{dI/dt}, \tag{2.14}$$

where $\varepsilon = -N\frac{d\Phi}{dt}$ is the induced electromotive force in the coil.

Solenoid and toroid are two common form of inductors used in analog filters. Solenoid inductors are cylindrical coils wound around cores and thus are easy to construct. The self-inductance of a solenoid inductor of N turns can be calculated with

$$L_{\text{solenoid}} = \frac{\mu_0 N^2 A}{l}, \tag{2.15}$$

where A is the cross-section and the l is the length of the solenoid inductor.

Toroidal inductors have a donut-shaped core on which the coil is wound. The toroidal inductors can achieve the same inductance with fewer turns and smaller size compared to the solenoidal coils. Another major advantage with the toroidal inductors is that the flux is contained within the core which avoids any unwanted mutual inductance. Conventionally, the cross-section shape of a toroidal inductor is circular or rectangular, the properties of the inductor can be effected by varying the cross-section shape. The inductance of a toroidal inductor with rectangular cross-section can be calculated with

$$L_{\text{toroid}} = \frac{\mu_0 N^2 h}{2\pi} ln(\frac{b}{a}), \tag{2.16}$$

where a and b are the inner and outer radii of the toroid, h is the height of the toroid.

2.2.2 Capacitor

Capacitors store energy in the form of electric field. Most capacitors consist of at least two electrical conductors separated by a dielectric medium, with one conductor being positively charged and the other negatively charged. The capacitors used in this work use a thin plastic film as the dielectric material and have a configuration with self-healing properties, in that dielectric breakdowns or short circuits between the electrodes do not necessarily lead to the destruction of the component.

The capacitance of a capacitor is defined as the ratio of the charge on the separated conducting surfaces to the applied voltage.

$$C = \frac{Q_C}{U} \tag{2.17}$$

The capacitance is in dependence only of the geometry of the design (e.g. area of the plates and the distance between them) and the permittivity of the dielectric material. When building analog filters, the designed capacitance can be achieved by connecting different commercially available capacitors in series or parallel. In real circuits, capacitance exists as parasitic properties of other components.

2.2.3 Real components behavior

Ideal inductors would have no resistance and capacitance. However, real inductors have parasitic resistance due to the resistance of the wire and energy losses in

core material and parasitic capacitance due to the electric field between the turns of wire which are at slightly different potentials. Just like the real inductor, a real capacitor contains additional parasitic components. In an ideal capacitor, the dielectric to separate the conductive plate is perfectly insulated. In a real capacitor, however, there is a very small current "leaking" through the dielectric. This can be expressed as a high value leakage resistance connected in parallel with the capacitor. The other parasitic resistor in series with the capacitor is the equivalent series resistance (ESR). ESR includes the equivalent resistance of the capacitor plates, the resistance of the terminal leads and the AC impedance of the capacitor when used at high frequencies. The equivalent series inductance (ESL) represents the residual inductance of the lead wires and the capacitor plates. Real inductor and capacitor models are shown in Figure 2.2.

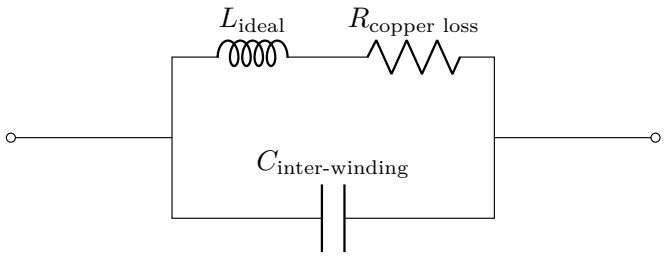

(a) The real inductor model.

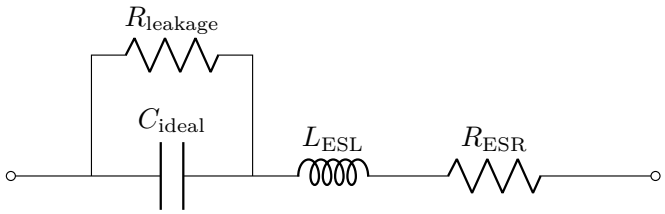

(b) The real capacitor model.

Figure 2.2: The electric model of the inductor and capacitor in a real circuit.

2.2.4 Quality factor

As shown in Figure 2.2a, a non-ideal inductor has series resistance. The impedance of an inductor consists of the resistance R as the real part and the

inductive reactance X_L as the imaginary part

$$Z_\mathrm{L} = R + X_\mathrm{L}, \tag{2.18}$$

where $X_L = \omega L$ is the reactance. The quality factor (or Q factor) of an inductor is the ratio of its inductive reactance to its resistance at a given frequency ω

$$Q = \frac{X_\mathrm{L}}{R} = \frac{\omega L}{R}. \tag{2.19}$$

The quality factor is a measure of the inductor efficiency, the higher the quality factor is, the closer the inductor approaches the behavior of an ideal, lossless inductor. The skin effect, proximity effect and core losses increase R with frequency, which will affect the value of the quality factor.

2.2.5 Resonant circuit

Capacitors and inductors are reactive components but their reactances have opposite signs. If these components are connected, the reactances can be eliminated exactly for a frequency f_r when $X_\mathrm{L} = X_\mathrm{C}$. Such circuits are called resonant circuits and f_r is the resonant frequency

$$f_\mathrm{r} = \frac{1}{2\pi\sqrt{LC}}. \tag{2.20}$$

Resonant circuits are often used as filters. There are series and parallel resonant circuits, which are shown in Figure 2.3.

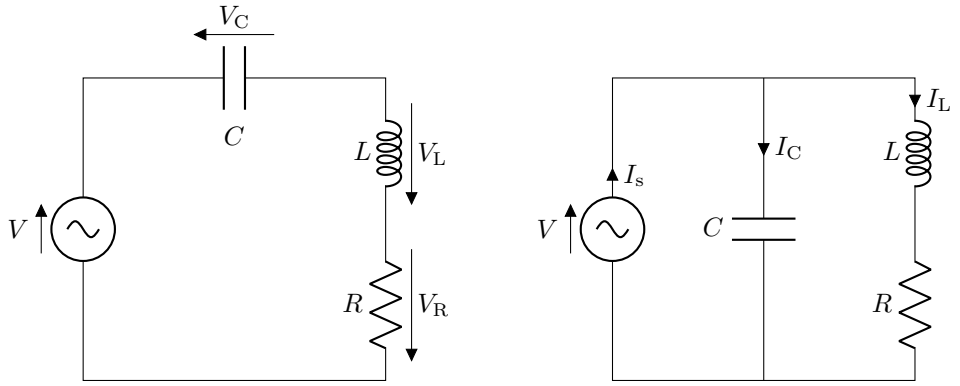

Figure 2.3: The series (left) and parallel (right) resonant circuit. Voltage and current direction is marked on each components.

Series resonant circuit

The series resonant circuit acts like it has no resistance at the resonant frequency. Only parasitic properties, like the series resistance of the coil, contribute to the total impedance. Due to this behavior, it is also called suction circuit, because it sucks off certain frequencies. In the series type, if the inductor is the primary coil of a transformer, then only one frequency will come out of the secondary coil. For frequencies far below the resonance frequency the circuit acts capacitively, for frequencies far above the resonance frequency inductively. Figure 2.4 shows a series resonant circuit with the corresponding impedance at different frequencies. In series resonant circuits a voltage increase occurs at the component. The voltage over the single component can be a multiple of the applied voltage. This voltage amplification can be described by the quality of the total circuit.

Parallel resonant circuit

In the parallel case, the impedance of the parallel circuit is at its maximum value and equal to the resistance of the circuit at the resonant frequency. There is a large circulating current between the inductor and the capacitor due to the energy of the oscillations. The currents I_{L} and I_{C} are equal and 180° of out phase thus canceling each other giving a net reactive current equal to zero. As a result, the overall circuit shows high resistance and low current, acting like an open circuit. The parallel resonant circuit can be used to short out everything except one particular frequency.

2.2.6 Filter classification

Filters can be classified based on their frequency selection properties, which can be described by their transfer characteristics in frequency domain. Figure 2.5 shows the ideal transfer function of different filters. Low pass filters (LPF) and high pass filters (HPF) are the two most basic forms of filters. Other filters can be divided into these two types of filters. For example, the series connection of a low pass filter and a high pass filter is a band pass filter (BPF), the parallel connection of a low pass filter and a high pass filter is a band stop filter (BSF).

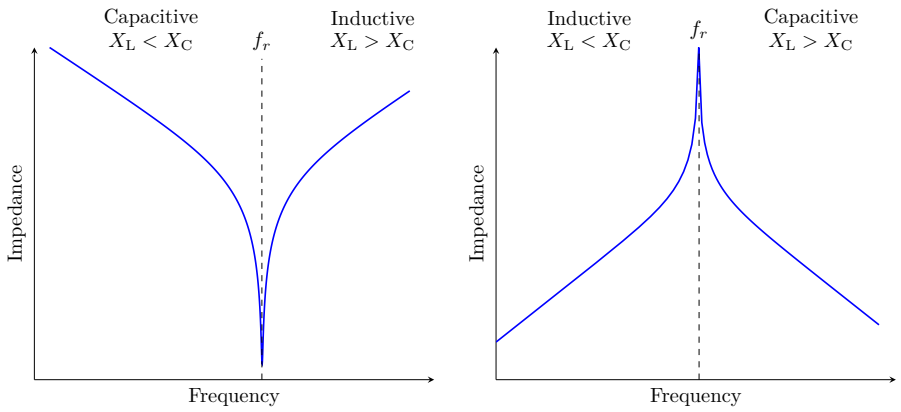

(a) Series (b) Parallel

Figure 2.4: Impedance of the series and parallel resonant circuits at different frequencies.

In reality, the filters show different properties as in Figure 2.5. For example, an ideal band pass filter would have a completely flat passband and would completely eliminate all frequencies outside the passband. In practice, the filters might have ripple either in passband or stopband and can not attenuate all frequencies outside the desired frequency range completely. Besides, a finite transition band always exists between the passband and the stopband, which is the filter roll-off. The frequency at which the response changes from passband to stopband is the cutoff frequency f_C and is defined as the frequency that is 3 dB below the maximum center or resonant peak. For the band pass and band stop filter there are lower cutoff frequency, f_L, and an upper cutoff frequency f_H. The frequency range exists between the two cutoff frequencies is commonly defined as the bandwidth.

$$BW = f_H - f_L \tag{2.21}$$

The resonant or center frequency f_0 is the geometric mean of f_L and f_H, which appears half way between f_L and f_H on a logarithmic scale.

$$f_0 = \sqrt{f_L \cdot f_H} \tag{2.22}$$

The selection of the filter type is based on the frequency range of the desired signal: passing those of interest, and attenuating the unwanted frequencies. For example, low pass filters can be used to stabilize amplifiers by rolling off the gain at higher

frequencies where excessive phase shift may cause oscillations. High pass filter can be used to block DC offset in high gain amplifiers or single supply circuits.

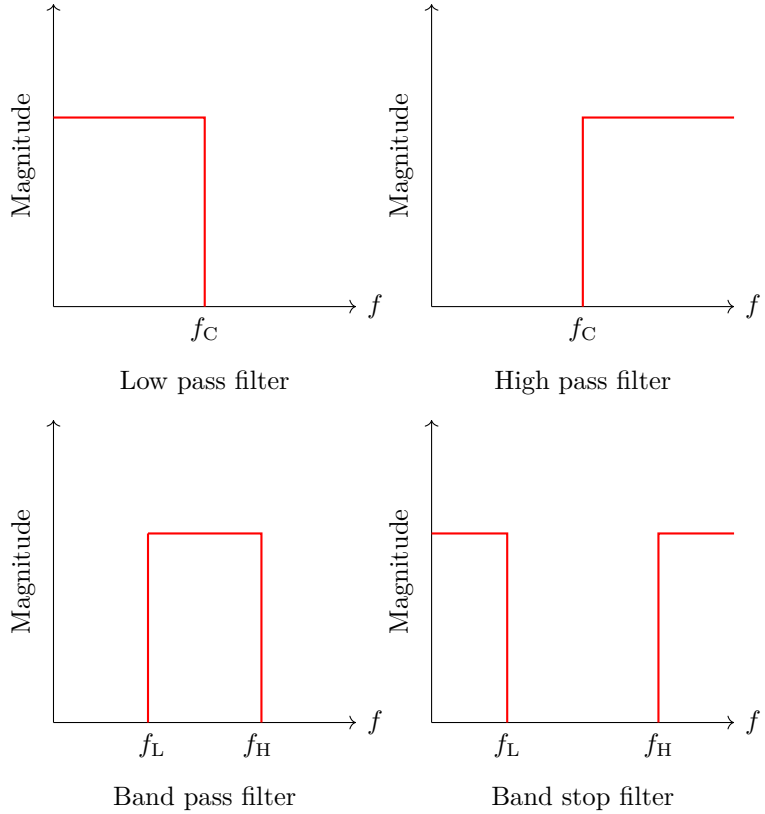

Figure 2.5: Ideal transfer characteristics of the four classes of analog filters according to frequency selection properties.

2.3 Magnetic particle imaging

The new imaging modality magnetic particle imaging (MPI) was presented by Gleich and Weizenecker in 2005 [5]. MPI allows the measurement of the spatial distribution of magnetic nanoparticles. MPI has several advantages over the currently established techniques: it is non-invasive, produces images from any position in the body, and does not rely on any damaging physical process (ionizing radiation). It is a tomographic imaging technique, which allows for real-time visualization. Finally, it is based on the use of magnetic nanoparticles tracers such as iron oxides, which are known to be biocompatible.

MPI has show a significant potential in applications including cardiovascular

imaging, cancer detection, cell imaging and a wide range of other fields [39, 40, 41, 42, 43, 44]. The development of a prototype for clinical application was started at Philips in 2011 [45]. After that commercial MPI scanners for preclinical applications were successfully developed by two independent vendors (Bruker Biospin MRI GmbH 2014, Magnetic Insight, Inc. 2017). These systems are especially important for allowing clinical experts to focus their research on the possible medical applications of MPI, and this requires reliable scanner hardware [46]. In this section a brief introduction of the physic principle behind MPI and how MPI works is given.

2.3.1 MPI signal generation

MPI utilizes tracers for imaging. In general, the basic principle of MPI is based on the nonlinearity of the magnetization of the MPI tracers. Considering the monodisperse superparamagnetic magnetite nanoparticles, which is an ideal MPI tracer, the magnetization curve when placed in an external magnetic field can be modeled by the Langevin function [47]:

$$M(t) = m_{\mathrm{s}} c \left(\coth(\xi) - \frac{1}{\xi} \right) \tag{2.23}$$

with

$$\xi = \frac{m_{\mathrm{s}} \mu_0 H(t)}{k_{\mathrm{B}} T}, \tag{2.24}$$

where $m_{\mathrm{s}} = \frac{1}{6}\pi D^3 M_{\mathrm{s}}$ is the magnetic moment as saturation of a single particle, c is the particle concentration. Note that this model only describes the ensemble magnetization of non-interacting superparamagnetic particles in thermal equilibrium. The physical behavior of realistic MNPs can be far more complicated and will not be discussed in this work.

In the absence of an external magnetic field, the directions of particle magnetic moments are randomly distributed due to Brownian motion, and the net magnetization of the ensemble will be zero. When an external magnetic field is applied, particles are aligned according to the direction and magnitude of the magnetic field. This alignment follows the magnetic field linearly up to a certain magnitude where the particles begin to exhibit magnetic saturation behavior.

This leads to a change in the slope of the magnetic flux density as a function of the magnetic field until the particles are completely saturated and the magnetic flux density stops increasing with the external magnetic field.

In MPI, the magnetic particles are driven by a homogeneous sinusoidal magnetic field, which is called the excitation field

$$H^D(x,t) = -A_{\mathrm{x}}^D \cos(2\pi f^t). \tag{2.25}$$

with the field amplitude A^D, frequency f. The signal generation principle by the excitation field is shown in Figure 2.6. According to Figure 2.3, the change of magnetization can be detected by receiving coils in the form of induce voltage. The non-linear magnetization response of magnetic particles creates a signal which has many spectral components apart from the excitation frequency, which is used for the image reconstruction.

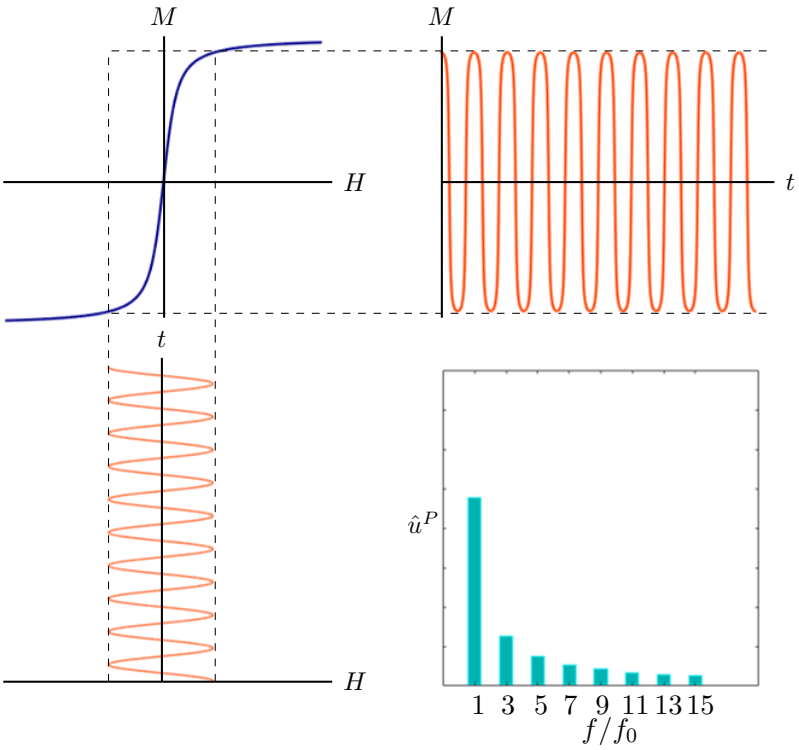

Figure 2.6: MPI signal generation. A sinusoidal excitation field (bottom left) drives the particles along the non-linear magnetization curve (top left). The response magnetization of the particles (top right) is measured by receive coils. The signal spectrum of the induced voltage in the receive coils (bottom right) contains higher harmonics apart from the excitation frequency.

2.3.2 MPI spatial encoding

Besides the excitation field, the so called selection field is used to achieve the spatial encoding in MPI. The selection field is a static field with a strong gradient and contains a special zero field location which is named field free region (FFR). When applying a gradient field to a volume containing magnetic nanoparticles, the particle magnetization will be saturated in most positions except the FFR. The saturated particles cannot react on the excitation field and behave like in Figure 2.7. As a result, only in the vicinity of the FFR, the particle magnetization will be in the dynamic range of the magnetization curve and induces MPI signal in the receive coil. There are two classes of MPI selection fields which generate different FFR shapes: the field free point (FFP) and the field free line (FFL). Just as the name indicates, location with a point- or line-shape which has zero field amplitude or zero field vector will be generated. The use of an FFL can also be seen in analogy to the imaging principles of CT. The MPI scanner used in this work features a FFP selection field, therefore only the FFP configuration will be discussed in this work.

The selection field with the FFP can be written as:

$$\boldsymbol{H}^S(\boldsymbol{r}) = \begin{pmatrix} G_\mathrm{x} & 0 & 0 \\ 0 & G_\mathrm{y} & 0 \\ 0 & 0 & G_\mathrm{z} \end{pmatrix} \mathbf{r} = g \begin{pmatrix} -\frac{1}{2} & 0 & 0 \\ 0 & 1 & 0 \\ 0 & 0 & -\frac{1}{2} \end{pmatrix} \boldsymbol{r}. \tag{2.26}$$

where $G_{\mathrm{x,y,z}}$ are the gradient strength of x,y and z direction respectively. $g = G_\mathrm{y}$ is the steepest gradient of the field [48].The gradient strength of the selection field varies in different directions: G_y is twice the value of G_x but with a different sign; G_z has the same value as G_x. Figure 2.8 shows a FFP created by the selection field in 2D scenario.

2.3.3 Moving of the FFP

The FFP or FFL has to be moved relative to the imaged object to not only cover one position but an entire area or volume which is defined as the field of view (FOV). Considering the 1D scenario, the FFP is moved back and forth along a line in direction of the field vector of the excitation field. The movement of FFP by the superposition of the selection field and the excitation field is shown in Figure 2.9.

For a sinusoidal homogeneous field directed in x-direction, the total magnetic field

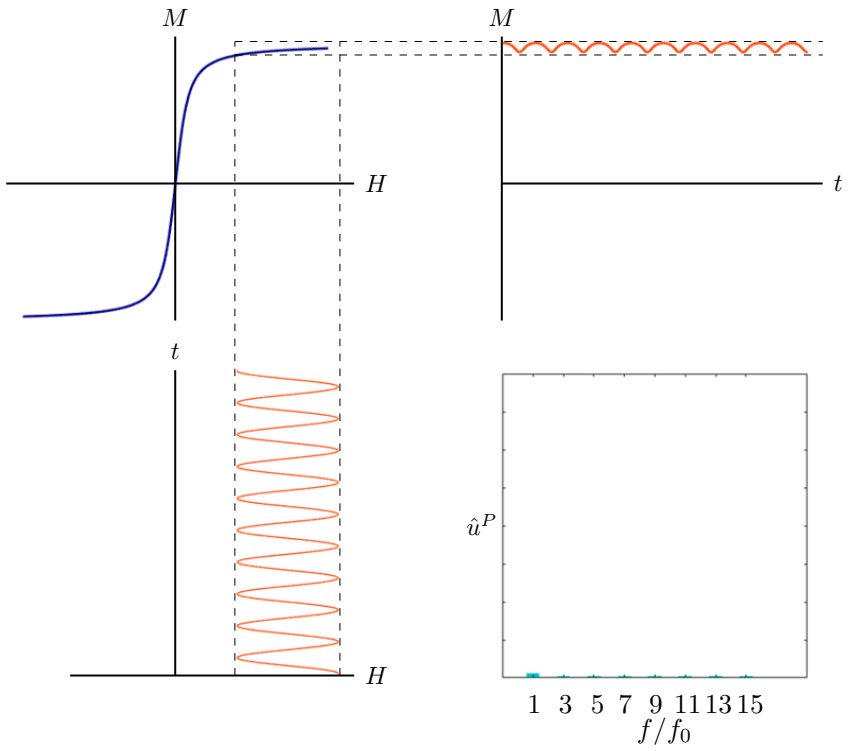

Figure 2.7: Signal generated by the particles out of the FFR. Due to the superposition of the selection field the particles are in the saturated region of the magnetization curve (upper left and bottom left). The particles magnetization do not follow the change of the excitation field and do not induce signal in the receive coils (upper right and bottom right).

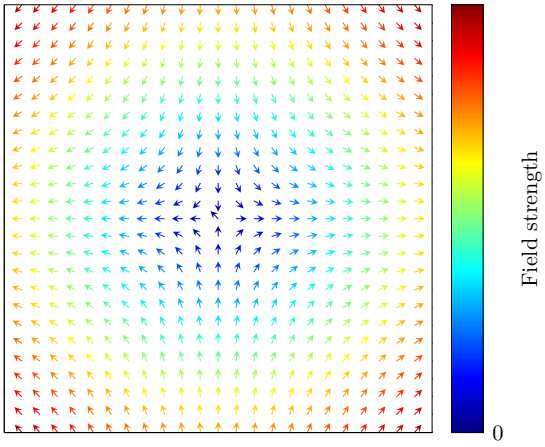

Figure 2.8: 2D selection field with the FFP.

in x-direction at time t is given by

$$H_x(x,t) = -A_x^D \cos(2\pi f^E t) + G_x x. \tag{2.27}$$

The FFP is the position where $H_x(x,t) = 0$, which locates at

$$x^{\mathrm{FFP}}(t) = \frac{A_x^D}{G_x}\cos(2\pi f^E t). \tag{2.28}$$

Therefore, the FFP oscillates along the x-axis within the interval

$$\left[-\frac{A_x^D}{G_x}, \frac{A_x^D}{G_x}\right]. \tag{2.29}$$

The so far mentioned alternating field provides only a shift of the FFP in one dimension. For the acquisition of multidimensional images the FFP has to pass every point within the field of view in sufficient proximity. By adding excitation from different directions, the FFP can be moved in 3D space. Figure 2.10 shows the 2D Lissajous trajectory of the FFP realized by using two similar frequencies in x and y directions. The path patterns along which the FFP scans the FOV, the trajectories, have a direct effect on the image properties. Besides the temporal resolution, which is determined by the repetition rate of these trajectories, they also influence the relaxation behavior of the particles.

2.3.4 MPI signal chain

A brief signal chain of an MPI system is shown in Figure 2.11. The sinusoidal signal to excite the MNPs is generated on a PC and then amplified by a power amplifier. For the fact that the excitation signal directly couples into the receive coils, the signal on the coils needs to have high spectral purity. However, the power amplifier introduces harmonic distortions into the signal. Therefore, the amplified signal needs to be filtered by a band pass filter to only carry the signal with the excitation frequency. The excitation signal together with the higher harmonics generated by the particles are received by the receive coils, but the higher harmonics are several orders of magnitude smaller than the excitation signal. Hence, the received signal has to pass a band stop filter to remove the excitation signal for the detection of higher harmonics. Since the remaining particle signals usually have very low amplitude in the pico- to nanovolt range, they are amplified by the low noise amplifier, which amplifies the signal without significantly degrading its signal-to-noise ratio. Afterwards the signal is digitized by the ADC and stored for signal processing and reconstruction.

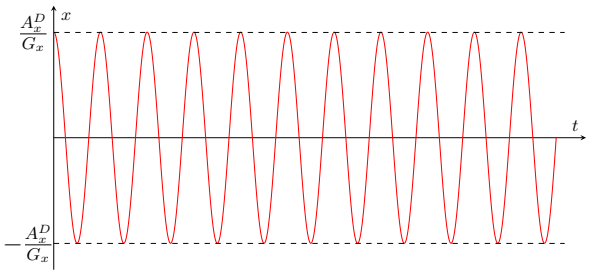

(a) 1D FFP trajectory over time.

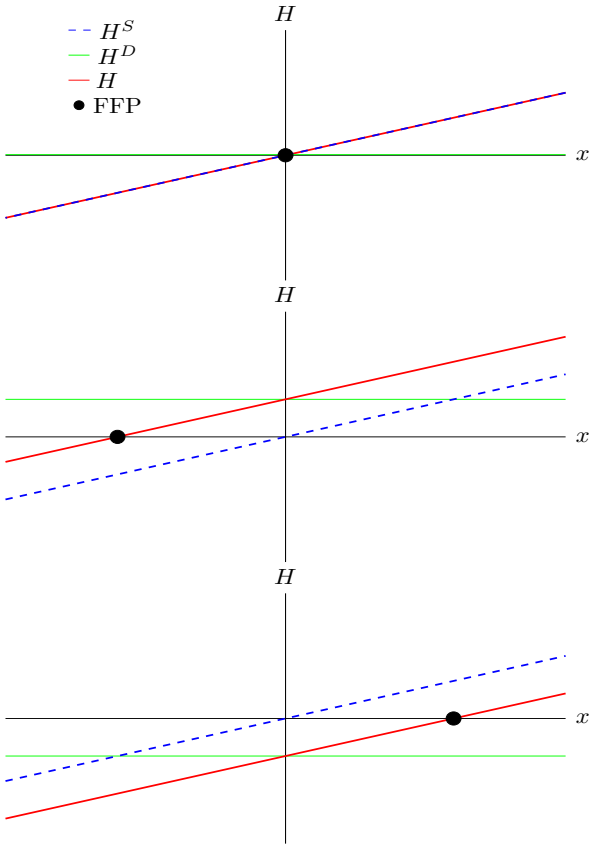

(b) Movement of FFP by the superposition of a homogeneous field.

Figure 2.9: FFP moved by the homogeneous excitation field in 1D scenario.

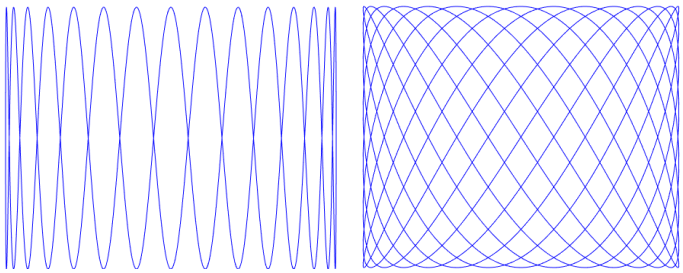

(a) Cartesian trajectory. (b) Lissajous trajectory.

Figure 2.10: Two types of FFP trajectory driven by sinusoidal excitation field.

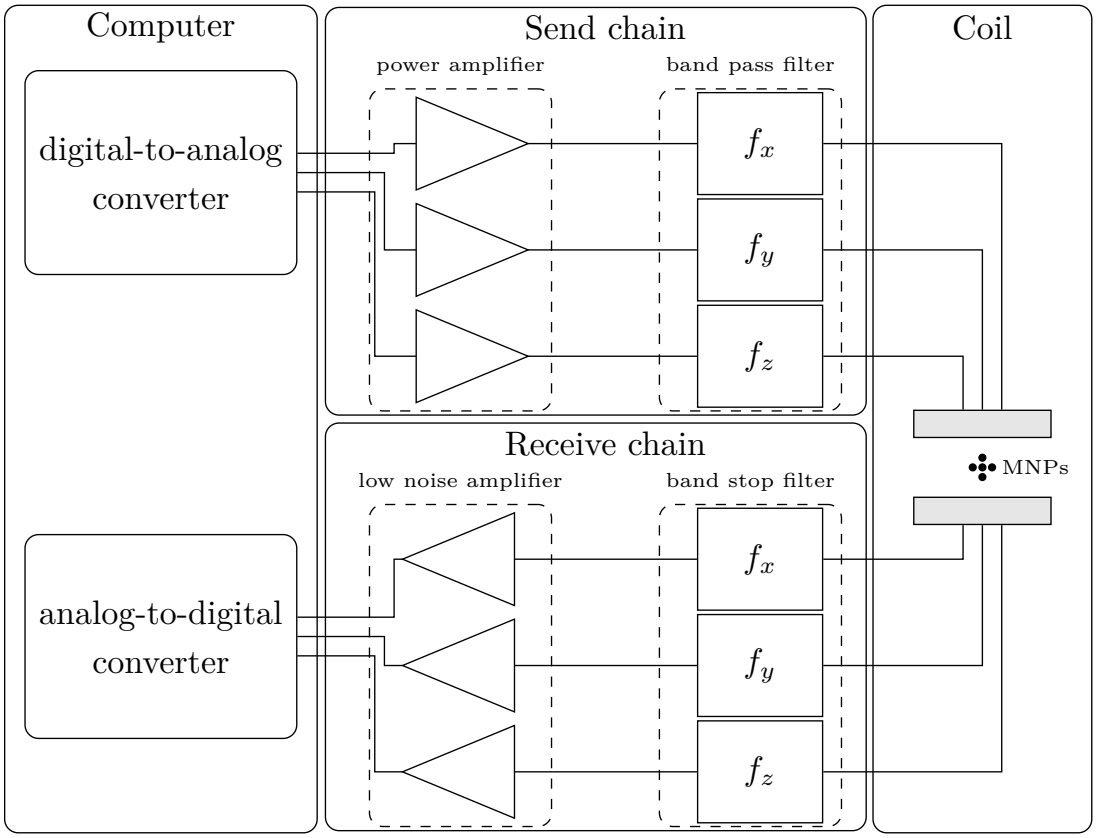

Figure 2.11: A brief diagram of the MPI signal chain of all three channels.

2.4 Magnetic fluid hyperthermia

Hyperthermia is a medical thermotherapy based on raising the temperature of a certain tissue above physiological values by different means[49]. The idea of what we currently call magnetic fluid hyperthermia was originally proposed in 1957 by Gilchrist [50]. In magnetic fluid hyperthermia, magnetic nanoparticles are utilized

as local heat sources to heat tissue, which are activated by an externally applied RF magnetic field.

2.4.1 Single-domain uniaxial nanoparticles in a magnetic field

Considering a single domain and uniaxial MNP placed in an external magnetic field ($\mu_0 H_{\max}$), its energy E is given by both the anisotropy energy (E_{A}) and the Zeeman energy (E_{Z}):

$$E = E_{\mathrm{A}} + E_{\mathrm{Z}} = K_{\mathrm{eff}} V \sin^2\theta - \mu_0 M_{\mathrm{S}} V H_{\max} \cos(\theta - \phi) \tag{2.30}$$

where K_{eff} is the effective uniaxial anisotropy, θ is the angle between the easy axis and the magnetization and ϕ is the angle between the easy axis and the magnetic field, $M_{\max}$ is the saturation magnetization. In MFH the magnetic energy is converted into thermal energy. If a magnetic material, like magnetic nanoparticles, is placed in an oscillating magnetic field the magnetic material will heat up during the reorientation of the magnetization and consequently heat up the surrounding tissue [51] [52].

2.4.2 Particle relaxation

When MNPs are exposed to an time-varying magnetic field, the magnetization lags behind the external field. There are two relaxation mechanisms: the Néel relaxation and Brownian relaxation. In Néel relaxation, the magnetic moment rotates within the magnetocrystal. The relaxation time of the Néel mechanism was first described by Néel [53] and later modified by Brown [54] to become

$$\tau N = \sqrt{\pi \frac{kT}{KV} e^{\frac{KV}{kT}}} \tag{2.31}$$

where K is the anisotropy constant, which may in general be due to either crystalline or shape effects, and V is the volume of the particle.

With the Brownian mechanism of relaxation the magnetic moment is locked to the crystal axis and when the magnetic moment aligns with the field, the particle

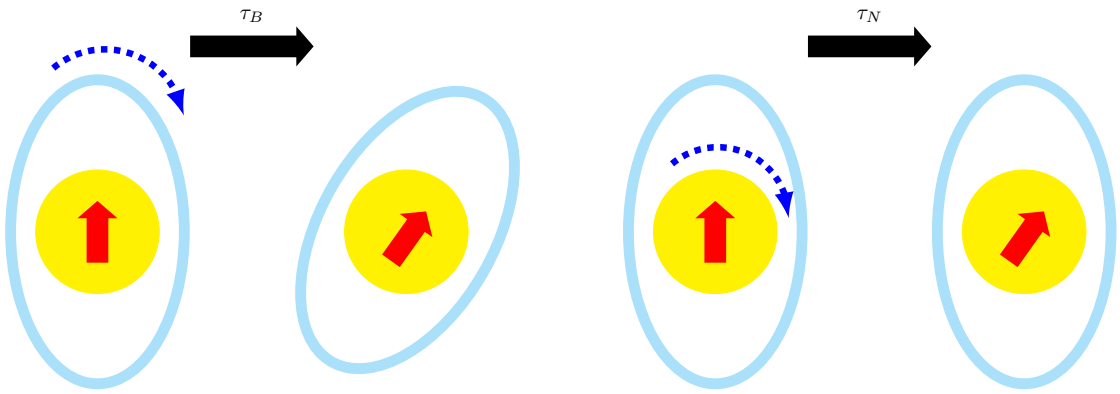

Figure 2.12: The brownian (left) and Néel (right) relaxation. Yellow circles indicate the magnetic single domain or the MNP in this case, red straight arrows indicate the magnetic moment direction, blue dashed arrows indicate the particle rotation or change in magnetic moment direction.

rotates as well. The characteristic time τ_B is strictly associated to their random hydrodynamic interaction with molecules of the liquid medium and their corresponding rotational diffusion time [16]:

$$\tau_B = \frac{3\eta V_H}{kT}. \tag{2.32}$$

Both relaxation processes are related by Shliomis' equation to give the effective relaxation times [55]:

$$\frac{1}{\tau} = \frac{1}{\tau_B} + \frac{1}{\tau_N}. \tag{2.33}$$

In practice, both mechanisms may occur simultaneously and the relative contributions are determined by the time scales at which each mechanism occurs.

2.4.3 Heat dissipation

To understand the heating process in MFH, different physical models of numerical calculations and analytical expressions of the dynamic response of MNPs in an alternating magnetic field (AMF) have been proposed [21]. The linear response theory (LRT) developed by Rosenweig in 2002 is one of the most used models, which is based on Néel–Brownian relaxation of single domain magnetic particles dispersed in a liquid matrix [56]. The volumetric energy dissipation (P) according to LRT is

$$P = \pi\mu_0\chi_0 H_0^2 f \frac{2\pi f\tau}{1+(2\pi f\tau)}, \tag{2.34}$$

where μ_0 is the permeability of free space, χ_0 is the initial susceptibility of the particles, H_0 is the magnetic field amplitude, f is the magnetic field frequency and τ is the effective relaxation time [56].

In the LRT model, it was assumed that the magnetization of the MNPs varies linearly with the applied magnetic field, therefore it is only suitable for the calculation of MNPs in the superparamagnetic regime at low magnetic field. When considering MNPs in other situations, different models should be used aiming at describing the hysteresis loop of MNPs. Knowing the magnetization of the MNP, The heat dissipation A released by the MNPs during one cycle of the alternating magnetic field can be given by the area enclosed by the corresponding hysteresis loop, which can be expressed as:

$$A = \int_{-H_{\max}}^{+H_{\max}} \mu_0 M(H) dH, \tag{2.35}$$

where $M(H)$ is the magnetization of the MNPs and $\mu_0 H_{\max}$ is the field amplitude [21].

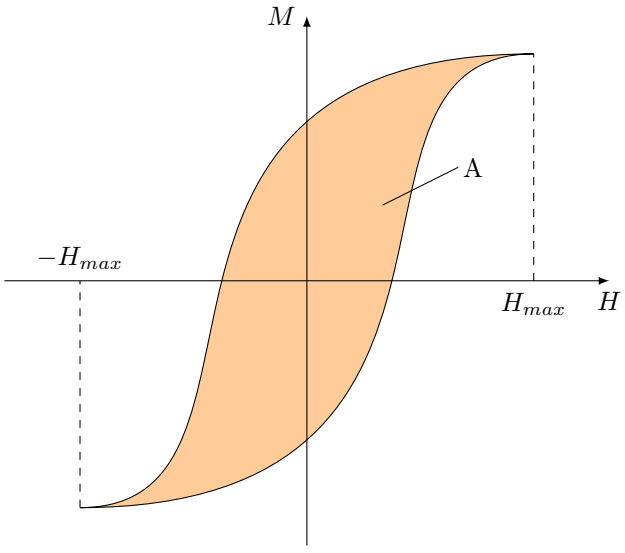

Figure 2.13: The hysteresis loop can be used to calculate the amount of heat released by the MNPs.

2.4.4 SAR

Typically, the specific absorption rate (SAR) is used to assess the potential of MNPs for magnetic fluid hyperthermia by measuring the heat dissipated by the particles, which is the absorbed energy per unit of nanoparticle mass.

In practice the SAR can be measured when assuming adiabatic conditions:

$$SAR = C_{\text{sample}} \frac{m_{\text{sample}}}{m_{\text{particle}}} \frac{\Delta T}{\Delta t} \tag{2.36}$$

where C_{sample} and C_{particle} stand for the specific heat of magnetic fluid and the MNP, Δt and ΔT corresponds respectively to time and temperature increments under the adiabatic conditions [57].

When the MNPs are dispersed in water, Equation 2.36 becomes:

$$SAR = \frac{C_{\text{water}} m_{\text{water}} + C_{\text{particle}} m_{\text{particle}}}{m_{\text{particle}}} \frac{\Delta T}{\Delta t} \tag{2.37}$$

where m_{water} and m_{particle} are the relative mass of water MNPs in the sample respectively. This parameter is quite dependent on magnetic field frequency and intensity as well as on nanoparticle size, shape, material, agglomeration rate and dispersion media.

2.4.5 Hardware setup

Solenoid coils are widely used in magnetic fluid hyperthermia applications. To heat up magnetic particle samples, an air-core solenoid coil can be used, which provides usable volume and homogeneous magnetic field. Figure 2.14 shows a simple electrical setup of a MFH device. The oscillating signal, normally in the frequency range from 100 kHz to 1 MHz, has to be generated and amplified to the desire amplitude. The solenoid coil is an inductive load thus has to be matched to the load of the amplifier to ensure the maximum power transmission. One simple method can be using two capacitors with the L network. The load seen by the amplifier is then a real load and the current on the coil is amplified at the working frequency.

The coil needs to be effectively cooled in order to ensure the proper working of the

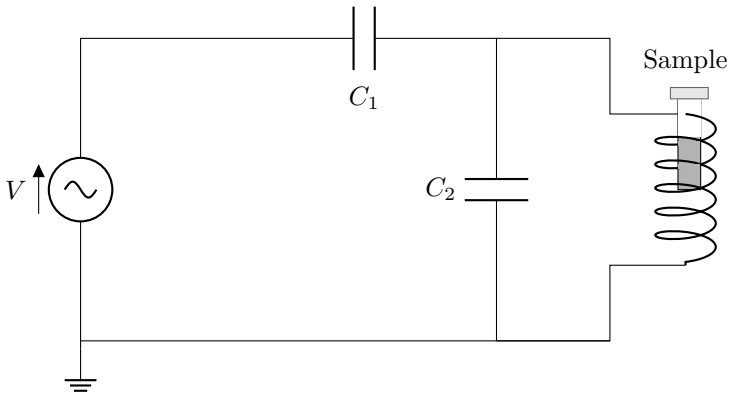

Figure 2.14: Air coil to generate a AMF with the sample placed in the center of the inductor.

setup and to prevent heat radiation from the coil to the sample. In practice, the hollow copper tube or the Litz wire are most used for the application.

2.5 Combination of MPI and MFH

So far, MPI is at beginning of the development from an imaging platform towards theranostic applications. However most setups apply either separate MPI and MFH systems or use a static selection field. In this section, the concept of a MPI-MFH platform using a dynamic selection field with a 3D FFP and the challenges in developing such a MPI-MFH platform are discussed.

2.5.1 Hyperthermia insert

In this work, the MPI-MFH platform is realized by designing an extension for an existing preclinical MPI scanner. The frequency of the alternating magnetic field generated by an MPI scanner is around 25 kHz, which is too low compared to the MFH frequencies (100 kHz–1 MHz) and cannot be directly used for MFH. Therefore, an extra alternating magnetic field with higher frequency is needed to enable the hyperthermia effect of the MNPs.

The work of Gräser et. al. presented a coil insert for the preclinical MPI scanner to improve the sensitivity of MNP detection [58]. Similarly, the MPI system can be equipped with a high-frequency heating coil, allowing excitation of magnetic

nanoparticles for MFH application. The solution in this work is to implement a hyperthermia insert, whcih can be placed in the MPI scanner bore and generate the hyperthermia usable magnetic field. 3D localized MFH and MPI imaging is realized through the preclinical MPI scanner.

2.5.2 Challenges

The coupling effect between the hyperthermia insert and the MPI scanner needs to be carefully treated. As described in section 2.1.3, the alternating magnetic field generate by one coil will induce voltage in another coil. In this case, the hyperthermia insert, which is essentially a solenoid coil, will induced voltage in all the coils of the MPI scanner around. This would be especially problematic in the MPI receive chain. Not only because of the distortion of the MPI signal spectrum, but also because of the damage it can bring to the LNAs. As introduces in section 2.3.4, the LNAs are used to amplify the MPI signal, which is in the pico to nanovolt range. When the induced signal exceeds the dynamic range of the LNA, the signal cannot be amplified properly and will damage the LNA in the worst case. Besides, eddy current will be induced in the metal parts in the scanner, which may result in significant induction heat at the high frequency of MFH. Therefore the challenge lies in minimizing the coupling between the hyperthermia insert and the MPI coils.

2.5.3 Clinical applications

As discussed in chapter 1, the MPI-MFH system can be used to non-invasively, spatial selectively open the blood-brain barrier. The targeted therapeutic opening of BBB allows new classes of long-acting or thermally activated drugs, antibiotics, neuropharmaceuticals or antiepileptics conceivable for neurological therapies. Multiple sclerosis and amyotrophic lateral sclerosis could finally be effectively put in the crosshairs because the known neuroprotective brain derived neurotrophic factor [59] could thus be made available in the neuropil. Brain tumors would not need to be punctured to deposit MNPs (for clinical thermotherapy) [60]. With the successful and precise opening of the BBB, a number of diseases could become treatable: Alzheimer's disease, ataxia, Huntington's disease, depression, epilepsy, fragile X syndrome, meningitis, encephalitis, Parkinson's disease, traumatic brain injury, and stroke. All diseases that are currently not treatable due to the

selective effect of BBB and the blockade of effective drugs.

3

Optimization algorithm for the coil topology design of the hyperthermia insert

Contents

3.1 Introduction

In chapter 1 it is demonstrated that a high gain comes from combining MPI and MFH in a theranostic platform, where the advantages of both sides can play out

and enable new therapeutic approaches in complex clinical settings. Chapter 2 proposes the concept of realizing such a platform by developing a hyperthermia insert for a preclinical MPI scanner. The two technologies are not easy to combine as typical MFH frequencies lie between 100 kHz and 1 MHz, which is in the MPI receive band. The MPI system has to be protected against the over voltage from the fast oscillating magnetic fields.

To limit the power transferred to the MPI system, the MFH signal can be suppressed by passive compensation. The chosen approach is to use a special coil topology design of the hyperthermia insert with self-compensation effect. Therefore apart from a solenoid coil for generating the radio frequency magnetic field for hyperthermia, an extra coil is needed to give the insert self-compensation property. In other words, the hyperthermia insert has a compensation winding, which creates a magnetic field opposing the primary heating field in a way where the primary heating field still is capable to heat up the particles but the MPI imaging system is not damaged by the induced voltage. The challenge is to determine the number of turns and the position of each single turn of the compensation winding to minimize the induced signal in the MPI receive chain.

This minimization problem is not analytically tractable since the coupling effect of a coil at different positions depends on the MPI scanner and can only be measured. In addition, the problem is of high dimension due to the multiplicity of the coil possible positions. Finally, there is no pre-knowledge of the solution space given that it highly depends on the recorded field profile.

In the field of engineering, metaheuristic methods can be used for optimization problems which are difficult to solve analytically to find a feasible optimal solution in a reasonable time. The advantage of metaheuristics is that they make few or no assumptions about the optimization problem and can search candidate solutions in very large spaces. Therefore, metaheuristics is used to analyze the optimization problem in this work. In this chapter, a hybrid algorithm is proposed based on the metaheuristic algorithm particle swarm optimization to find the optimal coil topology of the hyperthermia insert.

3.2 Basics of metaheuristic algorithms and particle swarm optimization

There is a large amount of existing metaheuristics, the majority of metaheuristics are based on biological evolution principles. Figure 3.1 gives a clarification of how abstract a metaheuristic works. This section will give a brief introduction to metaheuristic algorithms and the particle swarm optimization.

```
Create one or more initial solutions
  While (stopping criterion by exploitation step);
    If exploit then
      Create new solution by exploitation step;
    Else
      Create new solution by exploration step;
    End
    Update best found solution;
End
Return best found solution;
```

Figure 3.1: Abstract algorithmic framework for metaheuristics. (adapted from [61])

3.2.1 Fitness function

A fitness function is a merit that is used to summarize how close a given solution is to achieve the set aims and guide the algorithms toward optimal solutions. The candidate solutions are evaluated by the fitness function at each iteration and the candidate updating mechanism in the next iteration is adapted according to the fitness function results. Since the metaheuristics are usually designed for unconstrained optimization, the fitness function has to be adapted to tackle the constrained cases, i.e. those in which not all representable solutions are valid. To handle the constrain of solutions, penalty functions are introduced. The penalty function gives a fitness disadvantage to these individuals based on the amount of constraint violation in the solution. In other words, a penalty, in this case a constant of large value, is assigned to the fitness of one individual when the constraint is violated.

3.2.2 Benchmark functions

Benchmark test functions are fundamental optimization problems presented in the form of mathematical numerical functions [62]. These functions are also often rotated or shifted and also used with wider range of dimensions (from 10D to 1000D) to add complexity in the optimization landscape. They are used for algorithm performance validation and comparison with other algorithms. In this work, the Rosenbrock, Rastrigin and Griewank function are used. They are chosen since they are within the most commonly used benchmark functions and the performance of other algorithms on them are available in literature. The mathematical expression of the three functions are:

Rosenbrock:

$$f_1(x) = \sum_{i=1}^{n-1}(100(x_{i+1} - x_i^2)^2 + (x_i - 1)^2) \tag{3.1}$$

Rastrigin:

$$f_2(x) = \sum_{i=1}^{n}(x_i^2 - 10\cos(2\pi x_i) + 10) \tag{3.2}$$

Griewank:

$$f_3(x) = \frac{1}{4000}\sum_{i=1}^{n} x_i^2 - \prod_{i=1}^{n}\cos(\frac{x_i}{\sqrt{i}}) + 1 \tag{3.3}$$

The Rosenbrock function is an unimodal function and the Ratrigin and Greiwank function are multimodal functions. The solution space of the three functions is shown in Figure 3.2.

3.2.3 Particle swarm optimization

Particle swarm optimization (PSO) is one of the most popular nature-inspired metaheuristic optimization algorithms developed by James Kennedy and Russell Eberhart in 1995 [63]. PSO was inspired from animals behavior in society as fish schooling or bird flocking. Since its development, PSO has been used to solve practical issues in science and engineering. In PSO, each individual of the birds or fish is represented by a particle in the solution space of some problem or function, randomly assigned with initial velocity and position. The location and velocity of each particle will be recorded as $X_{i,j} = [X_{i,1}, X_{i,2}, X_{i,3}, ..., X_{i,D}]$ and

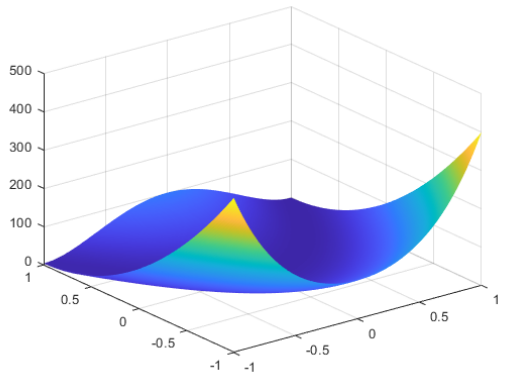

(a) Rosenbrock

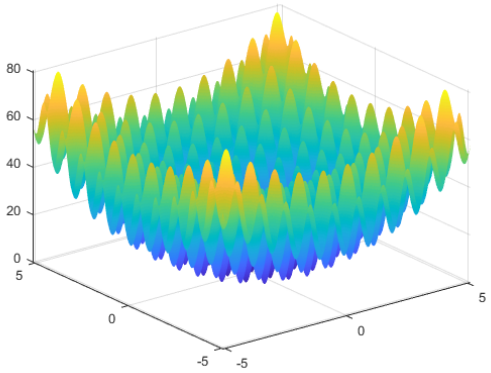

(b) Rastrigin

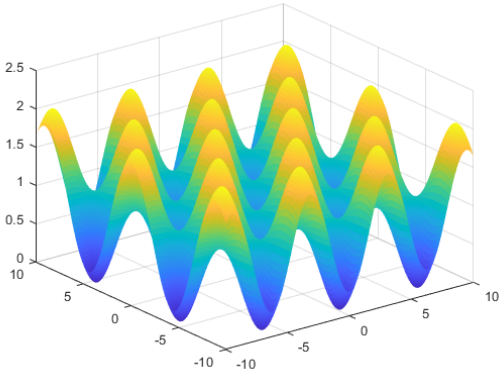

(c) Griewank

Figure 3.2: Solution space of three benchmark functions with $D = 2$. The rosenbrock function has a global minimum at the point (1,1), the rastrigin and griewank function have one global minimum at (0,0) and many local minima.

$V_{i,j} = [V_{i,1}, V_{i,2}, V_{i,3}, ..., V_{i,D}]$, with $i \in \{1,\mathrm{N}\}$ and $j \in \{1,\mathrm{D}\}$, N is the particle population and D is the dimension of the fitness function. The fitness function of every particles are first evaluated at their current location. Each particle has the memory ability and can memorize the best fitness position it ever reached. The particles also have the ability to communicate with other members of the swarm to know and memorize the best result found by the whole swarm. Each particle then determines its movement through the solution space based on the history of its own current and best locations with those of the swarm. At generation k, $X_{i,j}$ and $V_{i,j}$ are updated according to Equation 3.4 and 3.5.

$$V_{i,j}^{k+1} = \omega \times V_{i,j}^{k} + c_1 \times r_1 \times \left({P_{\mathrm{best}}}_{i,j}^{k} - X_{i,j}^{k}\right) + c_2 \times r_2 \times \left({G_{\mathrm{best}}}_{i,j}^{k} - X_{i,j}^{k}\right) \tag{3.4}$$

$$X_{i,j}^{k+1} = X_{i,j}^{k} + V_{i,j}^{k+1} \tag{3.5}$$

where P_{best} represents the personal best component of one certain particle, while G_{best} represents the best particle of the population up to current iteration, ω is the inertia factor, c_1 and c_2 are the acceleration factors, r_1 and r_2 are two random numbers generated between [0, 1], k is the current iteration. The algorithm is used to minimize the value of a function of several independent variables.

Figure 3.3 shows how P_{best} and G_{best} effect the movement of one particle in a certain iteration. The next iteration takes place after all particles' position are updated. Eventually the swarm as a whole is likely to move close to an optimum of the fitness function.

3.3 Optimization problem of the coil topology

As discussed in section 3.1, metaheuristic algorithms can be used to optimize the coil topology of the hyperthermia insert. In this section the coil design of the hyperthermia insert is discussed and modeled with an optimization problem.

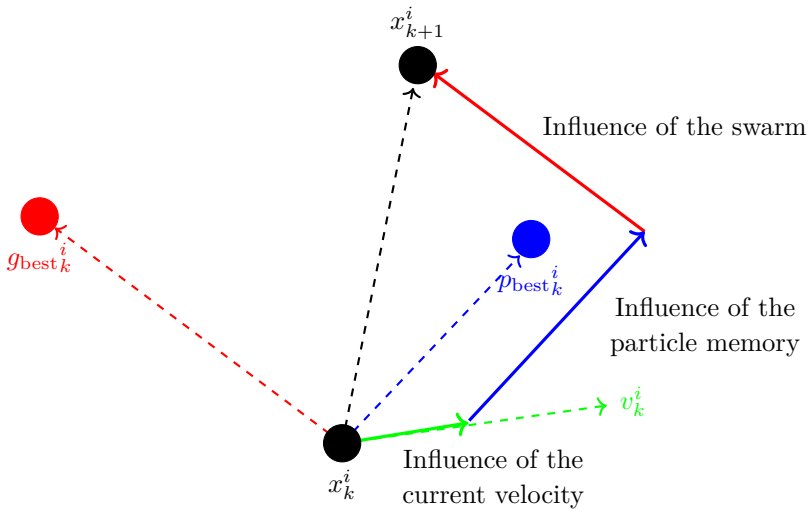

Figure 3.3: The illustration of the particle position update of the particle x^i from generation k to generation $k+1$ in particle swarm optimization. (adapted from [64])

3.3.1 Coil topology of the hyperthermia insert

The hyperthermia insert coil is composed of a heating coil to allow the hyperthermia and a compensation coil to generate the counter field for compensation. The heating coil is a solenoid coil which should be capable to generate a magnetic field up to 10 mT in amplitude for effective heating of the MNPs. Since it is intended to conduct experiments on the rat brain with the MPI-MFH system, the coil should fit a small size rat and cover the brain area. Therefore, the inner diameter of the coil is chosen to be 66 mm and a length of 30 mm.

The compensation coil is in series with the heating coil but wound in the opposite direction. To minimize the loss in field strength in the center, where the field is supposed to heat up the MNPs, the cancellation coil should be as far away from the heating coil as possible. Taking the space for cooling and the diameter of the litz wire into consideration, we set the diameter of the cancellation coil to 96 mm to fit the scanner bore with 118 mm diameter. The heating winding and compensation winding have to be placed in a way that the induced voltage in the MPI scanner is minimized or at least on an acceptable level.

3.3.2 Field profile

To create a data set which includes all influences of the target system a measurement-based approach following [58] is used. Here the measurement coils are translated along the scanner bore and the voltage induced by the scanner in the coils is measured with an oscilloscope. The measurement process is depicted in Figure 3.5. The procedure is conducted separately with measurement coils for the heating coil and compensation coil (Figure 3.4) and for all three channels of the system. The measurements give the field profiles $\hat{u}_x^h$, $\hat{u}_y^h$, $\hat{u}_z^h$, $\hat{u}_x^c$, $\hat{u}_y^c$ and $\hat{u}_z^c$ with respect to the measurement coils position in the scanner, where a superscript indicates heating (h) or compensation (c) windings and the subscripts indicate the channel x, y or z. Using the law of reciprocity one can deduct a winding profile which minimizes the induced voltage from the MFH insert to the MPI scanner. The induced voltages have been recorded for $N = 201$ spatial positions, thus the field profiles can be understood as elements of a 201-dimensional vector space.

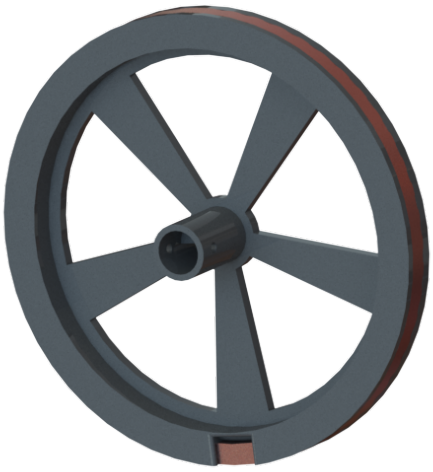

Figure 3.4: The measurement coil for the field profile recording. The coil has one single turn with the identical diameter as the heating coil or the compensation coil. It can be mounted on the probe stick of the MPI scanner and moved along the scanner bore by a robot.

The measured field profiles of each channel are shown in Figure 3.6. Since the coil is on the yz plane, most voltage is induced in the x direction.

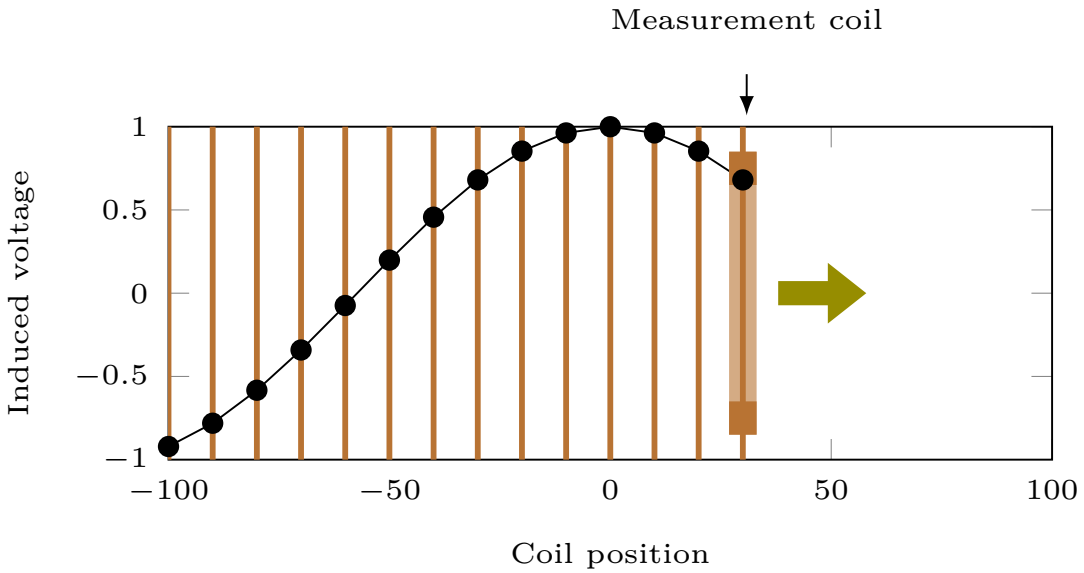

Figure 3.5: A visualization of the induced field profile measurement. The measurement coil is moved through the excitation field generated by the preclinical MPI scanner. The amplitude of the induced voltage is recorded depending on the coil position.

3.3.3 Minimization problem

As discussed in section 2.5, the induced signal by the hyperthermia insert in the MPI scanner receive chain needs to be minimized. This can be achieved by minimizing the following function:

$$\min_{w^j} \sum_i \left| \sum_j w^j \cdot \hat{u}_i^j \right|; \quad i \in \{\text{x,y,z}\}; \quad j \in \{\text{h,c}\} \tag{3.6}$$

where w_i^h and w_i^c with $i = 1, ..., N$ are the winding profiles of the hyperthermia insert coil, $\hat{u}_x^h$, $\hat{u}_y^h$, $\hat{u}_z^h$, $\hat{u}_x^c$, $\hat{u}_y^c$, $\hat{u}_z^c \in \mathbb{R}^N$ are the measured field profiles of the preclinical MPI scanner. It is useful to reduce the degrees of freedom for such a problem using rational arguments. It makes sense to only allow a single winding direction for the heating coil, to avoid self-compensation of the heating field, but allow both winding directions for the compensation coil, to allow best compensation. Therefore $w_i^h \in \{0, 1\}$ and $w_i^c \in \{-1, 0, 1\}$ with $i = 1, ..., N$. N is the number of the number of spatial positions, which is 201. Equation 3.6 is of high dimension and its solution space is not guaranteed to have a global minimum, since this highly depends on the recorded field profile. Therefore, the metaheuristic optimization approach is used to solve it.

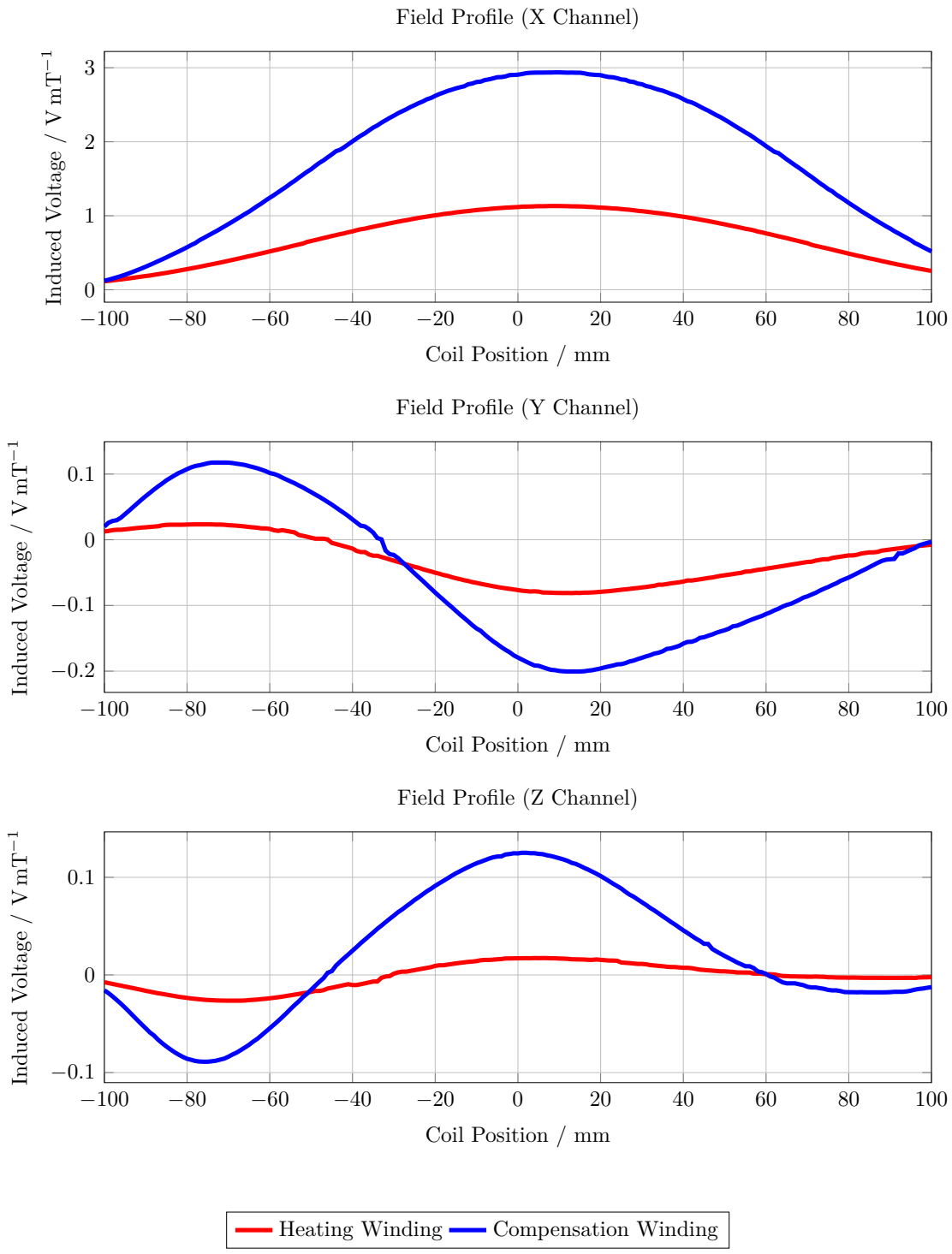

Figure 3.6: The ratio of the induced voltage to the magnetic flux density for a single compensation turn (blue) and a single heating turn (red) translated along the bore, while the MPI system creates a magnetic field along a certain direction (x, y or z).

3.4 Hybrid optimization algorithm

In this work, a hybrid optimization algorithm based on particle swarm optimization is proposed to minimize Equation 3.6. This section gives a detailed description of the hybrid algorithm and its performance on benchmark functions.

3.4.1 Premature of PSO

The motivation to develop the hybrid algorithm is the premature problem of PSO. Premature refers to that the algorithm converges to a local minimum, in other words, the particles trapped into local minima and cannot continue to search in other area in the solution space. As many other metaheuristics, PSO suffers from premature convergence. In PSO, the update of the particle position is based on the P_{best} and G_{best}, when a particle is in a local minimum, P_{best} and G_{best} will be updated to the current position. Once their values coincide, all the particles move to the same position thus lose the diversity of the swarm. In this case, it may be impossible for a particle to come out of the local optimum area once P_{best} and G_{best} coincide. Figure 3.7 shows the convergence curve of using PSO to minimize Equation 3.6. The fitness value decreases dramatic at the begin of the iteration, afterwards the convergence rate slows down and the result stops improving. In this situation P_{best}, G_{best}, X_i and X_{i+1} are all identical, therefore no new particle can be generated.

3.4.2 Modifications proposed for improving PSO

To improve the ability of PSO to search large areas in the solution space and prevent premature, modifications are made on the original algorithm. On one hand, the update process of PSO is simplified to improve the convergence velocity, which enables the algorithm to search with a larger population size and more evolution generations. On the other hand, disturbance and mutation of the particles are introduced to increase the population variety.

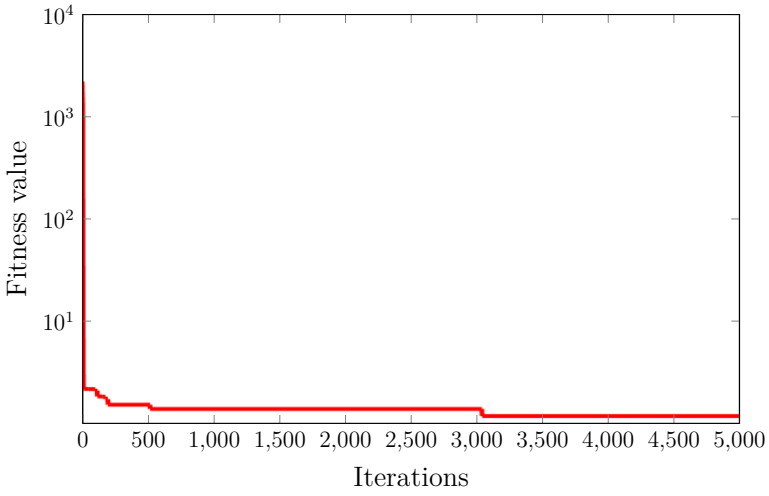

Figure 3.7: PSO convergence characteristics. The algorithm converges fast at the first 500 iterations. From iteration 500 the particle is trapped in the local minimum and cannot find better solutions.

Simplification of PSO

The original PSO can be simplified to reduce the calculation time, therefore the more particles can search in the solution space in the same time. A simplified PSO (sPSO) is adopted according to [65]. The sPSO discards the particle velocity and reduces the update process of the original PSO and the evolutionary process is only controlled by the variables of the particles position. The particle position is updated by:

$$X_{i,j}^{k+1} = \omega \times X_{i,j}^{k} + c_1 \times r_1 \times \left(P_{\text{best}}{}_{i,j}^{k} - X_{i,j}^{k}\right) + c_2 \times r_2 \times \left(G_{\text{best}}{}_{i,j}^{k} - X_{i,j}^{k}\right) \quad (3.7)$$

Introducing disturbance

Premature convergence can be prevented through maintaining the right balance between exploration and exploitation [66], which is the balance between the ability to search for more points in the solution space and the ability to search near the current solution. This can be achieved by adjusting PSO parameters and/or by introducing disturbances to maintain high diversity of the particles. In Equation 3.8 the P_{best} and G_{best} are multiplied with random numbers r_{3i} and r_4, trying to 'kick' the particle out of the local minimum.

$$X_{i,j}^{k+1} = \omega \times X_{i,j}^{k} + c_1 \times r_1 \times \left(r_{3i} P_{\text{best}}{}_{i,j}^{k} - X_{i,j}^{k}\right) + c_2 \times r_2 \times \left(r_4 G_{\text{best}}{}_{i,j}^{k} - X_{i,j}^{k}\right) \quad (3.8)$$

Improving the search diversity

Combining PSO with other search techniques also helps to improve the local search ability and increase the diversity thus avoid premature. In order to promote the search diversity in the PSO, a sea of models have been studied [64]. In this work, the mutation strategy of differential evolution algorithms is used to increase the search diversity of the original PSO. Differential evolution (DE) is a simple and powerful evolutionary optimization algorithm proposed by Storn and Price [67]. The implementation of DE is straightforward because its search process is governed by few algorithm-specific parameters. Despite its simplicity, DE is able to demonstrate a more promising optimization ability [68]. There are three basic operators of DE, namely the mutation, crossover and selection operator.

Mutation: DE employs the mutation strategy to generate a mutant vector V_i for each individual vector according to:

$$M_i^k = X_{r1}^k + F \cdot \left(X_{r2}^k - X_{r3}^k\right), \tag{3.9}$$

where F is the mutation scaling factor. r_1, r_2 and r_3 are distinct integers randomly selected from the $[1, N]$ and are different from i.

Crossover: After mutation, the mutants M_i are integrated in to the population by crossover process to generate a trial vector $U_{i,j}$:

$$U_{i,j}^k = \begin{cases} M_{i,j}^k & \text{if } rand \leq \text{CR or } i == randD \\ X_{i,j}^k & \text{otherwise} \end{cases}, \tag{3.10}$$

where CR is the cross probability, $rand$ is a random number between [0, 1], and $randD$ is a random number between [1, D].

Selection: For the next generation, the crossover processed vectors will be compared to the original vector and the vector with a better fitness will survive.

$$X_i^{(k+1)} = \begin{cases} U_i^k & \text{if fit}(U_i) \leq \text{fit}(X_i) \\ X_i^k & \text{otherwise} \end{cases}, \tag{3.11}$$

where fit is the fitness function, which is Equation 3.6.

3.4.3 Hybrid algorithm

The hybrid algorithm is proposed based on the original PSO with the three modifications in section 3.4.2. The flowchart of the proposed hybrid algorithm is shown in Figure 3.8. At each iteration, the particles are first manipulated with DE operator to introduce random mutations to the particle swarm. The fitness of the mutated swarm is then evaluated and the particles go through different process depending on the fitness result. Those have improved fitness value will be kept and enter the next iteration, while those show no fitness improvement will be updated by the PSO algorithm. The parameters of the hybrid algorithm are shown in Table 3.1. The parameters are chosen according to the original PSO and DE algorithms.

Table 3.1: Parameter values of the hybrid algorithm.

Inertial weight	0.4 to 0.9
Acceleration factors	$c_1 = c_2 = 2$
Scaling factor	0.1 to 0.9
Crossover probability	0.3
Population size	120
Maximum iteration	20000

3.4.4 Evaluation of the hybrid algorithm

The hybrid algorithm is tested on benchmark functions to prove its efficiency. The performance of the hybrid algorithm is compared with the original PSO and DE.

Convergence curve under fixed iteration times

To evaluate the convergence efficiency of the algorithm the performance of PSO, DE and the hybrid algorithm on the benchmark functions with fixed iteration times (500 iterations) are compared. The parameters of the used benchmark functions and the best solutions found by each algorithm are shown in Figure 3.2. Besides, the convergence curves of the best run within the 30 run times are compared and shown in Figure 3.9, 3.10 and 3.11.

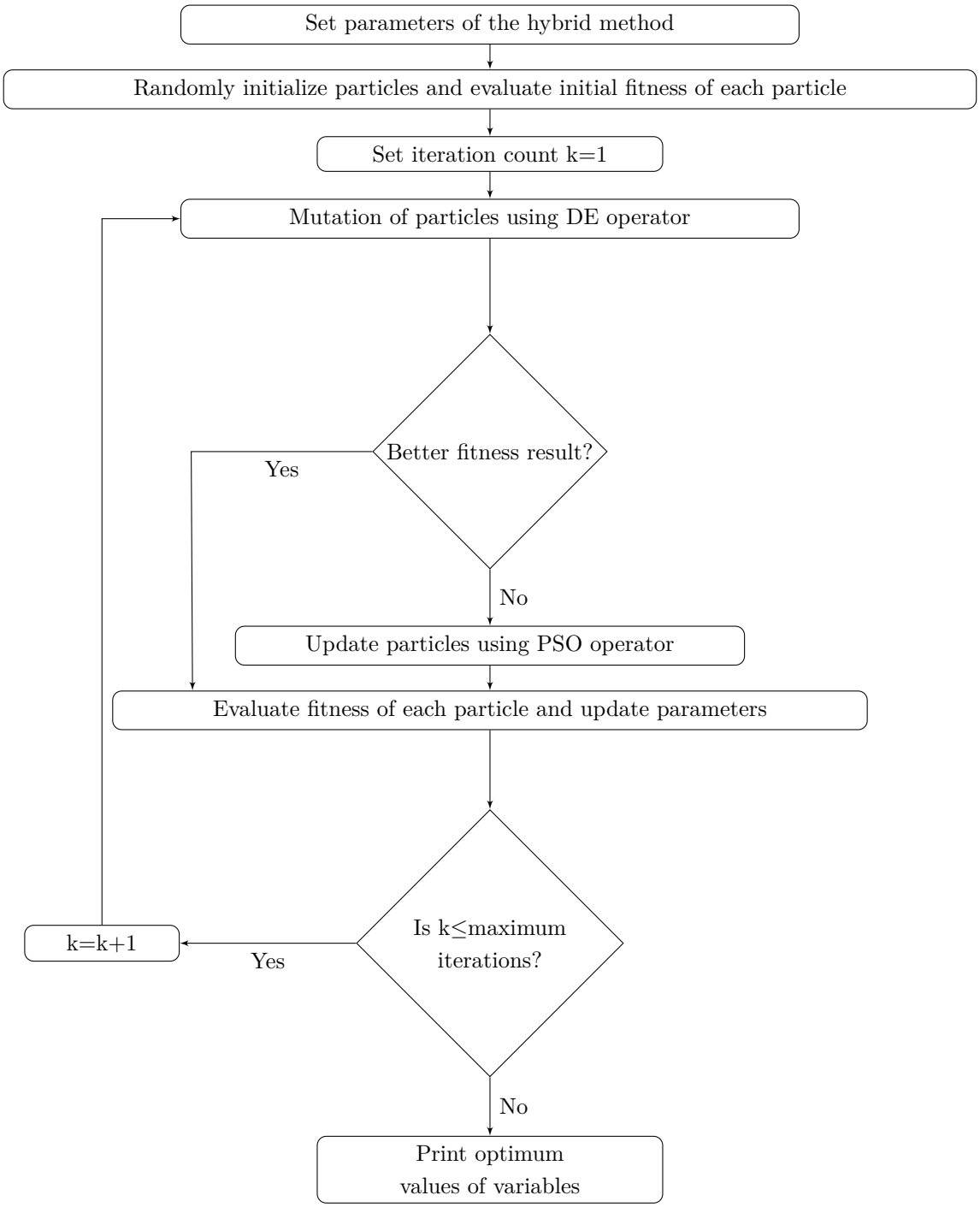

Figure 3.8: Flowchart of the hybrid method.

When comparing between PSO and DE, PSO finds better results under Griewank function while DE finds better results under the Rastrigin function. The results are similar under the Rosenbrock function. The hybrid algorithm finds the best result with a large improvement of the results found by the other two algorithms for the all

Table 3.2: Best solution of the benchmark functions found by PSO, DE and the hybrid algorithm within 500 iterations.

Benchmark function	Population size	Dimension	Solution Range	Iteration	Run times	Best solution		
						PSO	DE	Hybrid algorithm
Rosenbrock	50	100	[-2,2]	500	30	2339.67	2109.01	97.66
Rastrigin	50	100	[-5.12,5.12]	500	30	535.05	877.27	2.42E-11
Griewank	50	100	[-600,600]	500	30	208.82	63.12	0

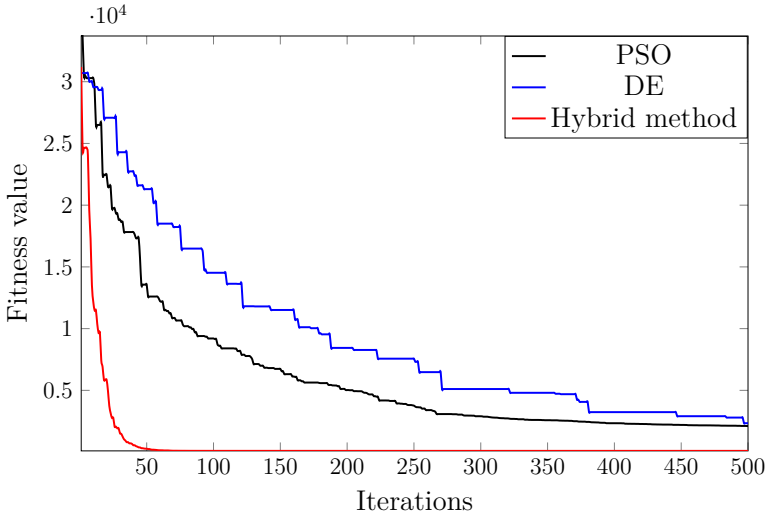

Figure 3.9: Convergence curve for Rosenbrock function.

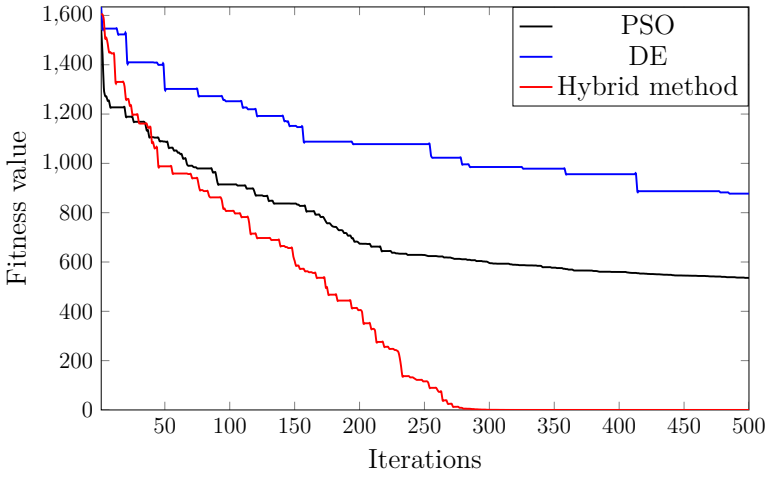

Figure 3.10: Convergence curve for Rastrigin function.

three benchmark functions, especially the Rastrigin function. It can be seen from the figures that, with the randomized initial solutions, the three algorithms begin

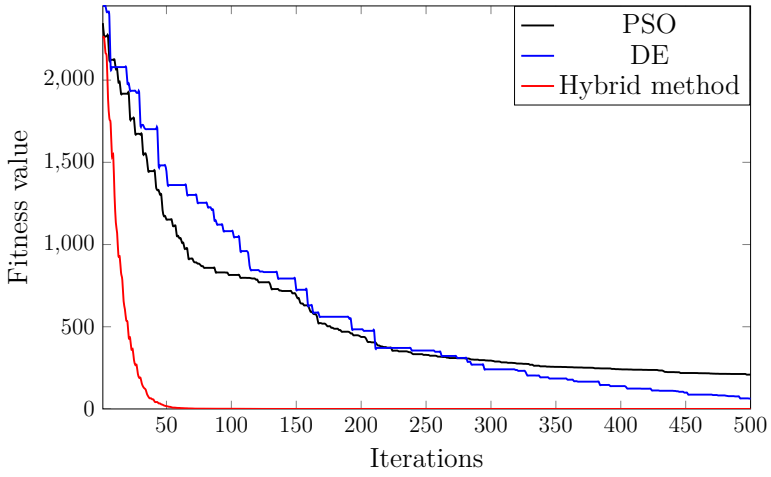

Figure 3.11: Convergence curve for Griewank function.

with similar initial values. After the iteration starts, the hybrid algorithm shows the highest convergence rate. The convergence rate of the PSO and DE are high at the early stage of the iterations and decrease gradually with the iteration process. Within the 500 iterations, PSO and DE are neither converged nor find the best result, while the hybrid algorithm converges significantly faster to the best solution. The above results show that the hybrid algorithm has an improved convergence efficiency than the two algorithms and find a better solution within the limited iteration times.

Population distribution analysis at different iteration stage

The multimodal function Rastrigin is chosen to evaluate and compare the distribution of particles in different periods of the iteration process between PSO, DE and the hybrid algorithm. The Rastrigin function has a large number of local minima and one global minimum at $\mathbf{x} = \mathbf{0}$ where $f(\mathbf{x}) = 0$. In order to display the results with 2D plots, the solution space of the benchmark functions is constrained to 2-dimensional and the population size of the algorithms is set to 30. The particle distribution is recorded separately at iteration 10, 30 and 50. The results are shown in Figure 3.12.

Due to the low dimension of the benchmark function, the algorithms converge very fast. In the early stage of the iteration, the particle distribution of the three algorithms is similar and more dispersed. After 30 iterations, the particles converge quickly to the global minimum. As discussed, the multimodal function

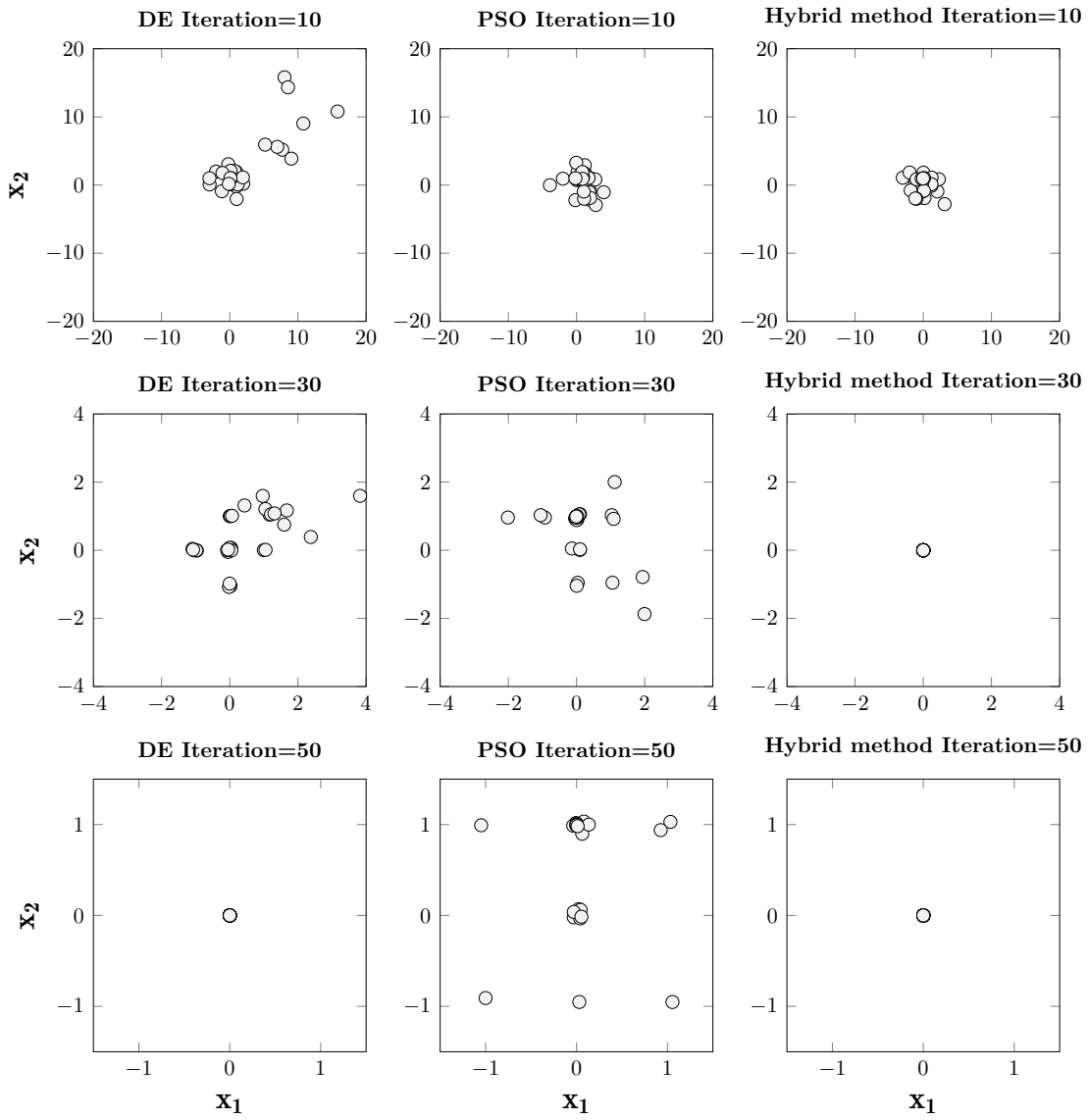

Figure 3.12: The distribution of the particles of PSO, DE and the hybrid method under the 2D Rastrigin function at the iteration 10, 30 and 50 respectively.

Rastrigin has several local extreme points, which are deceptive during search optimization process for the algorithm, also it has a great impact on the final result. It can be seen from the results of DE and PSO that the particles are constantly aggregating, but there are groups around several local extreme points and fall into the local traps. DE converges to the global minimum at 50 iteration, while the PSO still has not converged. However, in the case of the hybrid algorithm, all of the particles already find the best solution without falling into the local extrema with 30 iterations, showing a strong convergence.

Performance on minimizing the coupling effect

The algorithms' performance on minimizing the fitness function Equation 3.6 is compared. Theoretically, the global minimum would be 0 when the insert is perfectly decoupled from the MPI scanner. However, whether this can be achieved remains unknown since there is no information about the solution space of the fitness function. The fitness value and the consumed time for 30 runs are compared. The hybrid algorithm gives the best fitness value but needs the longest time for 30 runs.

Table 3.3: The optimized decoupling result found by PSO, DE and the hybrid algorithm.

Algorithm	Population size	Iteration	Best fitness value	Time consumed for 30 runs
PSO	120	10000	6.68	3900
DE	120	10000	0.39	2415
Hybrid algorithm	120	10000	0.018	9540

The convergence curves of the three algorithms are shown in Figure 3.13. The PSO converges after around 300 iterations and the result stops improving, while DE and the hybrid algorithm still keep the ability to escape from the current potion and find better result even at the late stage of the iteration.

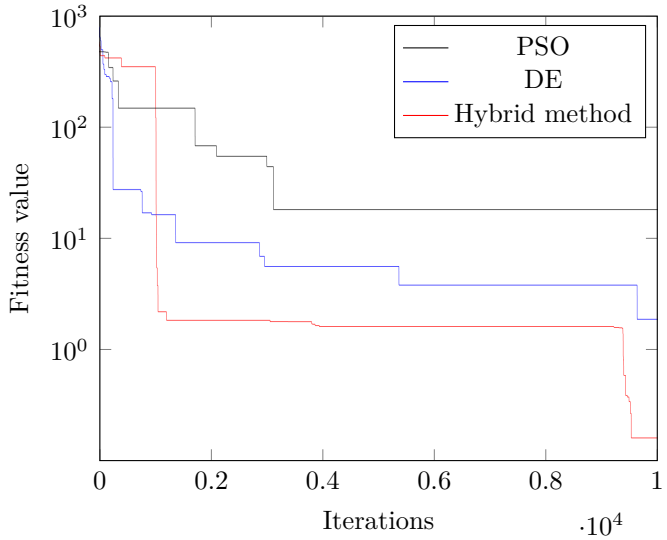

Figure 3.13: Convergence characteristics of PSO, DE and the hybrid method for function 3.6. The steps in the curves show the iteration where the particles escape from the locla minima and find better solutions.

3.5 Results and further improvement

The winding profiles of the compensation coil given by the three algorithms are shown in Figure 3.13. The bars represent each single turn of the winding at the according position. The direction of one turn is represented by the number 1 or -1, where 1 means the turn has the same direction of the heating coil, -1 means the winding has the opposite direction. The heating coil has 5 turns placed at $-12.5\,\mathrm{mm}$, $-6.25\,\mathrm{mm}$, $0\,\mathrm{mm}$, $6.25\,\mathrm{mm}$, $12.5\,\mathrm{mm}$ to the FFP along the scanner bore.

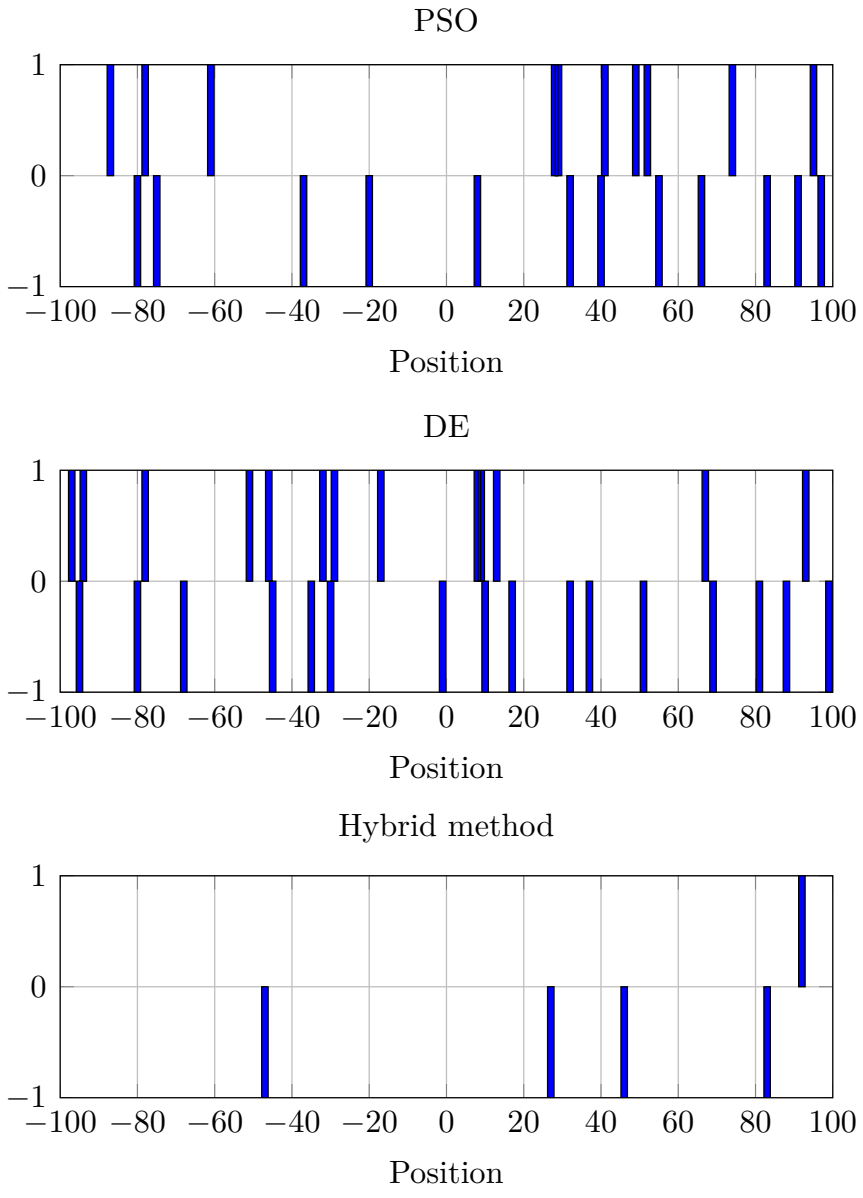

Figure 3.14: The winding profile given by PSO, DE and the hybrid method.

There are many other issues need to be taken into consideration for the construction of a coil with topology as in Figure 3.13. One is that the number of turns of the winding profile given by PSO and DE are 23 and 30 respectively, which are unrealistic since they result in coils with huge size and very high inductance. To build the hyperthermia insert, a coil with less turns is desired mainly because of two reasons. First, the power consumption of the insert is proportional to the square of current and the resistance. A coil with more turns will have higher resistance and needs larger current to generate the magnetic field with the same field strength. High power assumption is a challenge for both the power supply and the cooling of the coil. Second, the inductance of the insert increases with the number of turns. The voltage on the insert will be too high and may breakthrough the insulation between the windings. Another problem is the interval between two adjacent turns. In the results given by PSO and DE, several turns are placed at adjacent positions, which means the interval in between is 1 mm. However, due to the width of the litz wire, two turns have to be placed at least 5 mm apart from each other.

To include the problems stated above into the optimization process, the variables of the fitness function are changed from the winding status at each position to the number of turns and position of each turns. The maximum number of turns is set to n_{total}, the variable are $[n_1, n_2, ..., n_{n_{\text{total}}}, m]$. $n_{1,...,n_{\text{total}}}$ are the position for each turn and $m \in \{0, n_{\text{total}}\}$ is the maximum number of the minus turns. For each candidate, $n_{1,...,m}$ represents the position of the turns in the opposite direction of the heating coil and $n_{m+1,n_{\text{total}}}$represent the position of the winding in the same direction of the heating coil. To limit the total length of the coil, instead of varying the position $n_{1,...,n_{\text{total}}}$ in a large range from -200 and 200, only the positions in the interval $[-100, 100]$ are counted as a valid turn and contribute to the induced voltage.

Therefore, for a candidate $\mathbf{X}$, the winding profile can be obtained by:

$$w_i^c = \begin{cases} 1, & \text{if } i = n_j \text{ and } -100 \leq n_j \leq 100, j \in [1, m] \\ -1 & \text{if } i = n_j \text{ and } -100 \leq n_j \leq 100, j \in [m, n_{\text{total}}] \\ 0, & \text{otherwise} \end{cases} \tag{3.12}$$

By this, the maximum turns of the winding profile is constrained to n_{total}. Another advantage of this improvement is that the dimension of the problem is largely reduced from 201 to $n_{\text{total}} + 1$ so that the algorithm can find better result

with the same population size and iteration times. In this work, the maximum number of turns of the compensation coil is limited to 6 turns.

To ensure sufficient space for each turns, a constrain is added to the candidates using the penalty function. Every candidate is examined, if the distance between each winding is too close, a penalty of 1000 will be added to the fitness function.

$$Fitness(\mathbf{X}) = \begin{cases} Fitness(\mathbf{X}) + 1000 & n_i - n_j < 2, i, j \in [1, n_{\text{total}}]; i \neq j \\ Fitness(\mathbf{X}) & \text{otherwise} \end{cases} \tag{3.13}$$

The winding profile given by the hybrid algorithm with reduced dimension and modified fitness function has a fitness value of 0.008 and only has 9 turns in total. The 4 turns of the compensation coil are in the opposite direction of the heating coil at position −58 mm, −9 mm, 60 mm,91 mm to the center along the scanner bore axis. The final topology of the hyperthermia insert coil is shown in Figure 3.15.

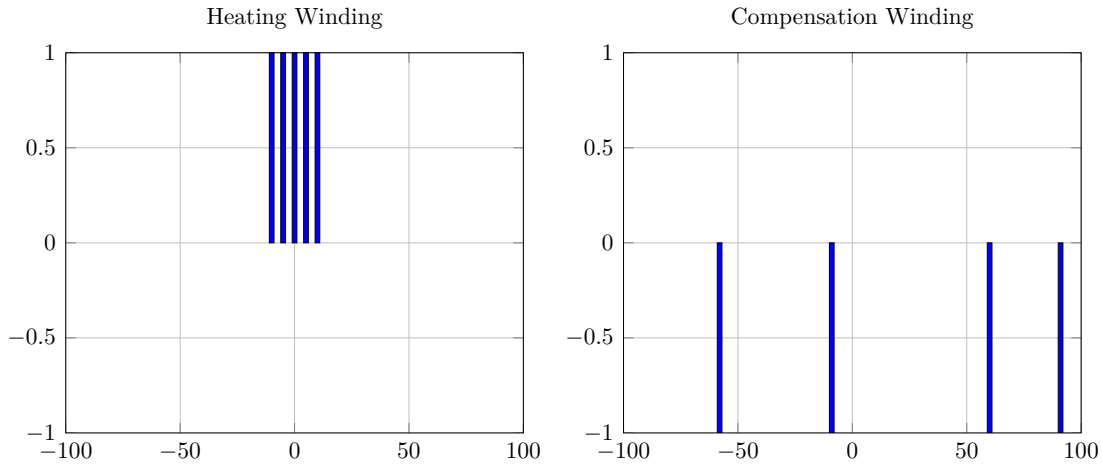

Figure 3.15: Optimized winding profile obtained by the hybrid method to minimize the induced signal composed of 5 heating turns and 5 compensation turns.

3.6 Summary and Discussion

In this section, the coil topology design of the insert is discussed. The main challenge is to decouple the insert coil to the MPI system, which means to minimize the

induced signal by the insert coil in the MPI receive chain. The method proposed is a self-compensation coil design with a heating coil to generate the MFH field and a compensation coil to compensate the effect of the heating coil. While the topology of the heating coil is relatively defined to fit the rat cassette and cover the rat head, the winding profile of the compensation coil is given by an optimization algorithm.

The optimization of the coil topology is then modeled as a minimization problem. To find out the solution of the minimization problem, metaheuristic algorithms PSO and DE are introduced. When choosing the algorithms, attempts have been made with many other metaheuristics to minimize the induced voltage. Among those PSO and DE showed best performance. It can be seen from the fitness value in Table 3.3 that PSO and DE along can already find promising result. However a better result is still beneficial to have less residue power, which is easier to handle with the extra receive filter. Through analyzing the convergence characteristics, the premature of PSO is very obvious: the result keeps the same and does not improve after a certain times of iteration. This leads to the idea to combine PSO with DE to keep the advantage of PSO and introduce new particle population by DE to maintain the population diversity. Based on the two algorithm, the hybrid algorithm is developed. The hybrid algorithm is compared with the two original algorithms and shows improved performance in all aspects.

It can be seen from the convergence curve that the hybrid algorithm is effected by the premature problem as well, the result stay unimproved for long period. Nevertheless, it still equips the ability to escape from the local minimum even at the high number of iteration (around 8000) and find a better result in the end. The randomness of the optimization result needs to be mentioned. The optimization process starts with random initial solutions and there are many random steps when updating a particle, which results in different best solutions by each run. Therefore, the algorithms are run for several times to ensure the global minimum is found. In this work the best solution of 30 runs is used. Better result might be found when increasing the iteration or the run times. However, the improvement is quite limited since the result found with the current parameters is already very close to the theoretic optimal result 0.

The first result of the winding profile is unrealistic for the coil construction. The fitness function is then modified to take all the practice problems into consideration. As a good side effect, the dimension of the problem is largely reduced and the result is further improved. The winding profile shown in Figure 3.15 is the final result with

a good compensation result. It has only 9 turns and a length of 154 mm. It would be beneficial to have a winding profile with shorter distance between the first and the last turn, so that the size of the insert can be reduced. However, the 9 turns and 0.008 fitness value is considered as a "good enough" solution in this work and the winding profile is used for the insert coil construction.

In this chapter, the hybrid algorithm is only compared with PSO and DE. There are a large amount of modified optimization algorithms based on PSO or DE has been published. A comparison of two other algorithms is shown in Table 3.4 and 3.5. However, further analysis and evaluation of the hybrid algorithm as an optimization algorithm is beyond the frame of this work.

Benchmark function	Population size	Dimension	Solution Range	Generation	Run times	Best solution	
						DEPSO	Hybrid algorithm
Rosenbrock	20	30	Unconstrained	1000	100	80.8259	27.6468
	40	30	Unconstrained	1000	100	66.8730	27.0975
	80	30	Unconstrained	1000	100	60.6405	26.8482
Rastrigin	20	30	Unconstrained	1000	100	0.8656	27.6468
	40	30	Unconstrained	1000	100	0.0099	0
	80	30	Unconstrained	1000	100	3.919E-009	0
Griewank	20	30	Unconstrained	1000	100	0.091	0
	40	30	Unconstrained	1000	100	0.0069	0
	80	30	Unconstrained	1000	100	0.0056	0

Table 3.4: Comparison with DEPSO [69].

Benchmark function	Population size	Dimension	Solution Range	Generation	Run times	Best solution	
						FCPSO	Hybrid algorithm
Rosenbrock	30	500	[-2,2]	1000	100	1.29E003	4.98E002
Rastrigin	30	500	[-5.12,5.12]	1000	100	1.28E004	23.85
Griewank	30	500	[-600,600]	1000	100	1.96	7.66E-015

Table 3.5: Comparison with FCPSO [70].

4

Implementation and high power test of the hyperthermia insert

Contents

4.1 Introduction

In this chapter, the implementation of a hyperthermia insert for the preclinical MPI scanner to generate the high frequency magnetic field for hyperthermia applications

is discussed. The hyperthermia insert is made up of two main parts: a coil system to generate the magnetic field and a cooling unit for the cooling of the coil system. The coil topology of the coil system has been discussed and given in chapter 3. In this chapter, the decoupling effect of the optimized coil topology is validated using rapid prototyping technique. Simplified model which consists of the winding placed on a minimal skeleton-like structure is produced according to the winding profile shown in Figure 3.15. The power transmitted to the MPI receive chain can be estimated with the prototype by the transfer function measured at small signal level, which avoids potential damage on the MPI system. Based on the prototype, the cooling unit of the hyperthermia insert is designed. The challenge is to fit the optimized coil system and a suitable cooling unit inside the MPI scanner as well as use the limited volume effectively to ensure a wider range of experiments within the insert. The design and construction of the hyperthermia insert using additive manufacture technique are detailed in this chapter. To effectively transmit power to the platforms, an impedance matching network is implemented. Finally, the magnetic properties, cooling capacity, stability, and the ability to heat up MNPs of the hyperthermia insert are evaluated with high power tests.

4.2 Prototype of the hyperthermia insert

Prior to the construction of the hyperthermia insert, a prototype is manufactured for small signal measurements. The estimation of the electrical and magnetic characteristics as well as compensation effectiveness of the coil can be obtained with the prototype and provide information for the insert final design.

4.2.1 Design of the prototype

The design of the prototype starts from simulation using the calculated coil topology. Based on the simulation results, parameters of the litz wire used for the coil can be determined. Knowing the geometry parameters of the litz wire, the coil support structure can be designed accordingly.

Simulation

The finite element solver FEMM (finite element method magnetics, version 4.2) [71] is used to simulate the magnetic and electronic properties of the insert coil. FEMM is an open source program for defining, solving, and post processing 2D planar and axisymmetric problems of magnetostatics, eddy currents, electrostatics and heat flow using the finite element method [72]. Despite its special topology, the hyperthermia insert coil is axisymmetric therefore can be modeled in FEMM. As shown in Figure 4.1, only half of the coil is sketched. Own to the symmetry of the coil, the information of the magnetic field in 3D space can be obtained with the sketched part. The circles represent the turns of the winding placed at the designed position.The 5 turns of the solenoid heating coil can be modeled as a whole using a rectangle. However, to consider the 1.25 mm space between the adjacent turns and have a more precise simulation result, they are modeled with 5 separate circles. The heating and compensation coils are categorized into two circuits with the same value of current but the opposite direction, representing that they are counter-wound. It is necessary to simulate the behavior of litz wire to ensure the correct simulation result at high frequency range. At 700 kHz, the material of the coil wire (circular area) cannot be simply defined as copper, where the litz wire is considered as a solid conductor and loses its property of mitigating the skin effect. Therefore, a custom defined "litz wire" material with the number and diameter of the strands in the litz wire is used for simulation. Figure 4.2 compares the current density with the wire with different settings. When the material is set as copper, the skin effect is very obvious and current only flows through the surface of the wire, however when the material is set to litz wire, the current density within the wire is homogeneous. The material of the rest of the space is set as air. Finally, the open boundary with 10 layers is used for the unbounded space. The simulation results are shown in Figure 4.1. The magnetic field generated by the heating coil, compensation coil and the complete coil system is simulated. The heating coil generates a magnetic field inside the solenoid. By adding the compensation coil, the magnetic field at the center remains the same, while at the both ends of the heating coil is affected by the counter magnetic field of the compensation coil and has weaker magnetic field. According to the simulation, $I_{\text{peak}} = 170\,\text{A}$ is needed to generate 10 mT magnetic field at the center of the heating coil.

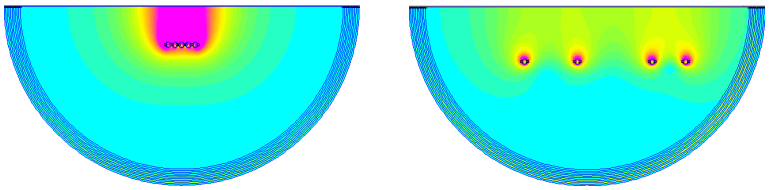

(a) Magnetic field generated by the heating coil (left) and the compensation coil (right).

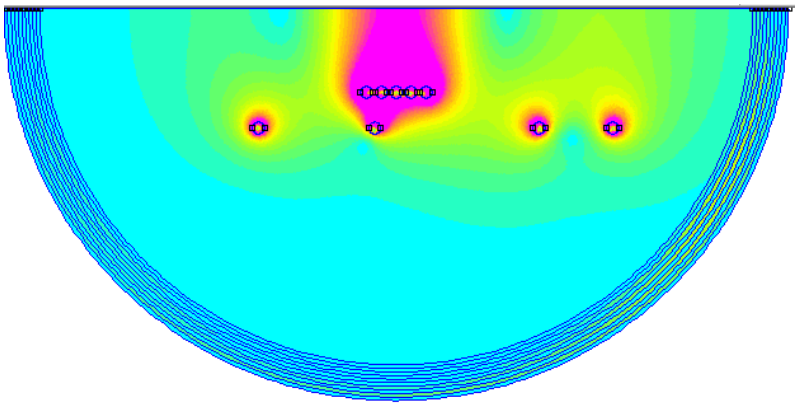

(b) Magnetic field generated be the hyperthermia insert coil.

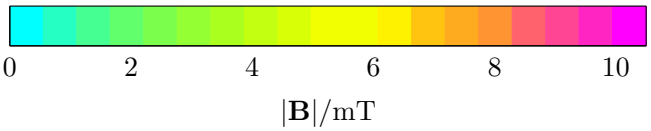

Figure 4.1: FEMM simulation results of the magnetic field generated by the coil system with 170 A_{peak} 700 kHz current on the circuit. The circles show the position of each turns of the coil.

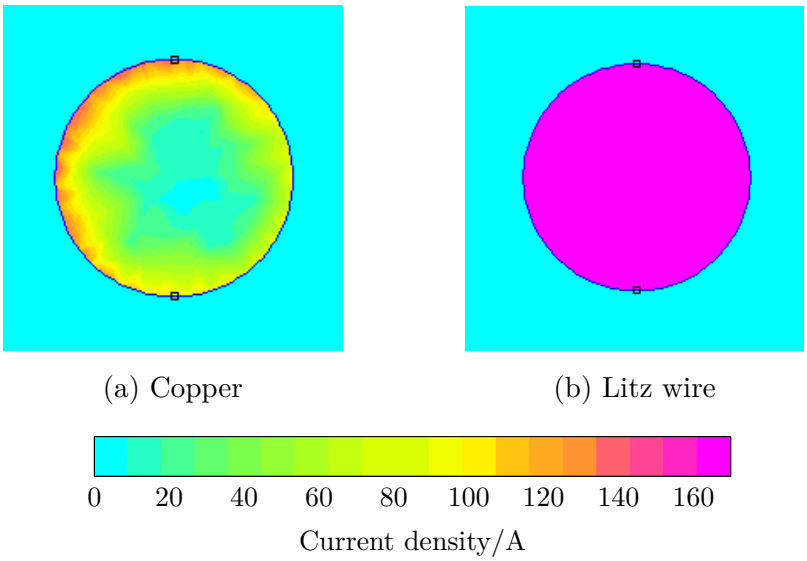

(a) Copper (b) Litz wire

Figure 4.2: Simulated current density of the wire using different material settings. 700 kHz AC with 170 A_{peak} is used for the simulation. Due to the skin effect, current only flows on the surface of the wire when the material is defined as copper. When using litz wire, the skin effect is mitigated and the current density is homogeneous on the cross section of the wire.

Choice of litz wire

To mitigate the skin effect at high frequency range, litz wire is used to wind the coil. According to the simulation results, the litz wire will carry 170 A current with around 700 kHz. Therefore, the litz wire with 8000 single strands and 0.04 mm diameter of each strand is chosen for the coil. The outer diameter of the whole litz wire is around 5 mm. Normally, litz wire is served with additional insulation material and tapes. For the insert coil the unserved litz wire is used because of its good flexibility. Another advantage is that the coolant can flow in between of each single strand and has a better cooling effect. However the strands are easier to be broken than served litz wire, which can result in an increased resistance. Therefore, the litz wire has to be treated carefully and wound on material with smooth surface.

Coil support structure

Conventionally a solenoid coil can be wound around a cylinder core. To wind a coil with the desired winding profile, a coil support structure as in Figure 4.3a is

designed. It is composed of 3D printed parts to support the litz wire and spacers in between of each turn to keep the winding in the designed positions. The height of the spacers is set according to the distance between each turn. The topology of the compensation coil could be fine-tuned by the use of spacers of different heights, which reduces the time of optimization. The support structure of the heating coil is a cylinder with grooves to guide the litz wire to the correct position.The same design as in Figure 3.4 is used for the support structure of a single turn of the compensation coil.

The implemented prototype is shown in Figure 4.3b. The heating coil and compensation coil are wound with a single litz wire with no soldering joints, which would experience excessive heating due to the high frequency and flux density requirements of the coil. The connection litz wire between the heating coil and the compensation coil is twisted and fixed along the axial direction of the coil to minimize parasite inductance and signal coupling with the MPI system.

4.2.2 Estimation of electrical characteristics

For the estimation of the electrical characteristics a precision LCR meter (Keysight E4980A, Kesight Technologies, USA) is used to measure the series resistance R_S and the series inductance L_S of the prototypes at a frequency of 700 kHz. The measured result is compared to the simulated result in Table 4.1. The resistance of the prototype is similar as the simulation result while the inductance increases. Since the simulation has not taken the connection wire into consideration, the prototype should have a higher resistance and inductance due to the longer wire. However, considering the very low resistance of the coil, the difference between the simulation and measured result might not be obvious. With 170 A current through the 2.9 µH coil at 700 kHz, the voltage across the coil reaches around 2 kV. The high voltage drop needs to be considered when designing and manufacturing the cooling unit and other components of the circuit.

Table 4.1: Electrical characteristics of the prototype.

Simulated result		Measured result	
Series Resistance	Inductance	Series Resistance	Inductance
45 mΩ	2.3 µH	44 mΩ	2.7 µH

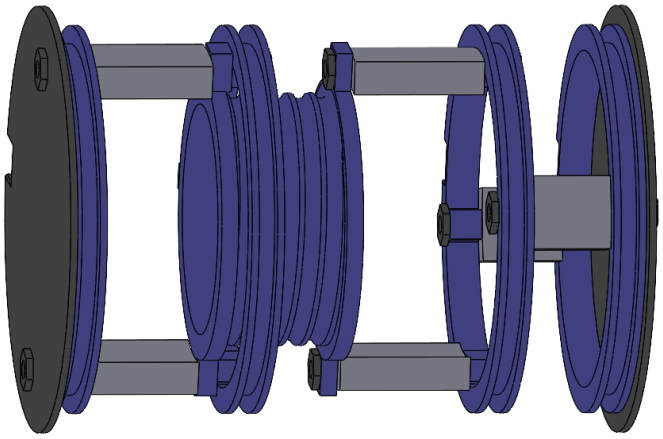

(a) CAD model of the coil support parts. The gray parts are the spacers and the litz wire is wound on the blue parts.

(b) Prototype of the hyperthermia insert. The the coil support parts are printed using Form 2 (Formlabs, USA) and Ultimaker3 (Ultimaker B.V., Netherlands) 3D printers. The printed parts are assembled together using screws and thread rods.

Figure 4.3: Design of the coil support structure and the hyperthermia insert prototype.

4.2.3 Estimation of magnetic characteristics

To evaluate the magnetic field created by the prototype, a DC source (DC power supply SM30-200, Delta Elektronika, Netherlands) is connected to the coil and a measurement current of $I_{\mathrm{m}} = 3\,\mathrm{A}$ is applied. The magnetic field H_{m} produced by the prototype is measured with a gaussmeter (Lakeshore Model 460, Lakeshore

Cryotronics, USA). The gaussmeter probe is controlled by a Cartesian robot (Isel Automation, Germany) to measure the magnetic field strength at the center of the heating coil over a volume of 22.5 mm × 18 mm × 12 mm in steps of 1.5 mm in each direction. The covered volume is chosen to imitate the size of a rat brain [73], which is the target for MFH therapy in this work. The magnetic field at the xy plane over an area of 30 mm × 30 mm in steps of 1 mm is measured as well. To compare with the simulation result, the magnetic field with 170 A current is calculated based on the measured results. Since the magnetic field strength is directly proportional to the amount of current flow through the coil, the field produced at unit current H_0 can be calculated using

$$H_0 = \frac{H_\mathrm{m}}{I_\mathrm{m}} \,. \tag{4.1}$$

Therefore, the magnetic field generated with I_max=170 A is

$$H_\mathrm{max} = I_\mathrm{max} H_0. \tag{4.2}$$

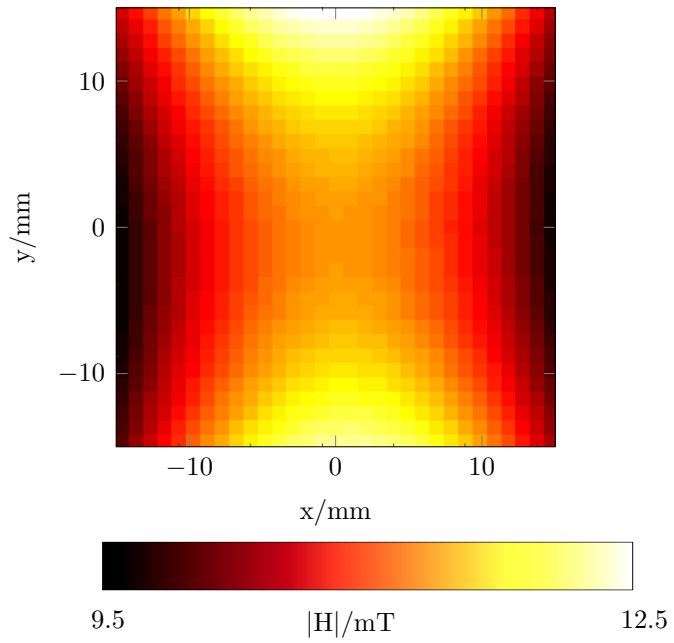

Figure 4.4: Magnetic field strength generated by the prototype on the xy plane. In the axial direction of the insert, the field strength decreases with the distance from the center. In the radial direction the field strength increases with the distance from the center.

The average field strength is 12.13 mT, with a standard deviation of 0.73 mT. As

shown in Figure 4.4, the magnetic field generated by the prototype has the similar profile as the simulation results. Along the axial direction, the magnetic field strength decreases as getting away from the FFP, while along the radial direction the magnetic field strength increases as getting away from FFP and closer to the winding. Figure 4.2 compares the average and the standard deviation of the calculated and simulated field strength over the same volume. The field profile of the calculated magnetic field along three axes is compared to the simulation results in Figure 4.5. The two field profiles have high similarity, which indicates the influence of the connection wire on the field can be ignored. However, the simulation has given a lower prediction of the magnetic field strength, which is around 2 mT lower than the measured values.

Table 4.2: Magnetic field comparison of the simulated and measured results. The prototype generates a stronger field than the simulation.

Direction	Average/mT		Standard deviation/mT	
	Simulation	Prototype	Simulation	Prototype
x	9.49	12.38	0.48	0.35
y	10.16	12.82	0.14	0.12
z	10.06	12.76	0.06	0.05

4.2.4 Small-signal evaluation of prototype decoupling

The prototype is used to evaluate the effectiveness of self-compensation of the optimized winding profile. The transfer function from the prototype to the low noise amplifier output of the MPI system is measured over a frequency range from 100 kHz to 1 MHz by a network analyzer (LF-RF Network Analyzer E5061B, Keysight Technologies, USA). The measurement schematic is shown in Figure 4.6. The prototype is placed in the MPI scanner imaging bore in the position that the center of the heating coil and the FFP coincide. The prototype is connected to the T-input (transmission port) of the network analyzer and the LNA output of the according channel is connected to the R-input (receive port) of the network analyzer. As usual the RF out of the network analyzer is also fed to the R input of the network analyzer as reference. The same parameter of a 5-turn solenoid coil that has the same geometry of the heating coil but without compensation is also measured and shown as a comparison in Figure 4.7. The send power is set to

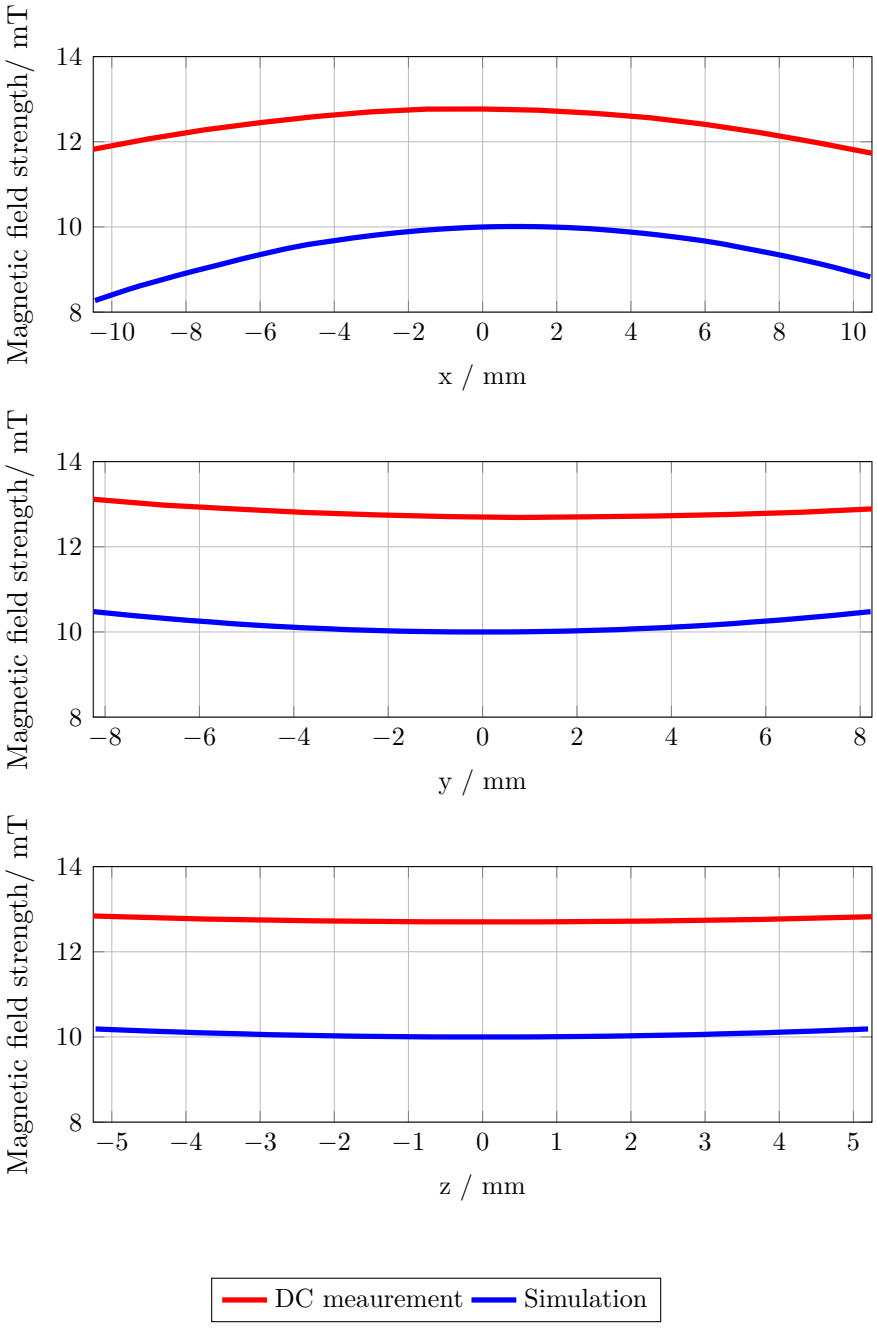

Figure 4.5: Magnetic field comparison of the simulated and DC measured results along the x, y, and z axis. The field profiles are similar while the field strength generated by the prototype is higher than the simulated results.

make the two coil setups generate the magnetic field with the same strength. After compensation, the magnitude at 700 kHz of all three channel decreases, especially on the x channel. On y and z channel the results are similar since the

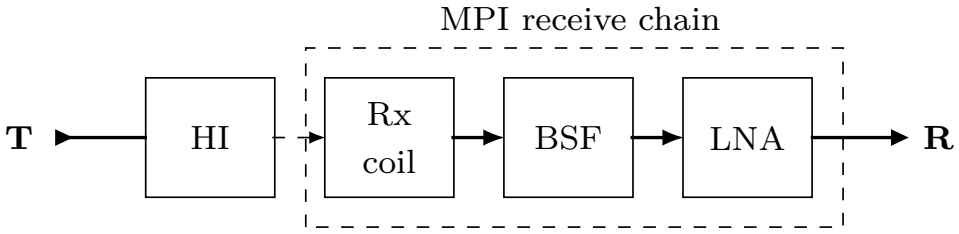

Figure 4.6: Diagram of the transfer function measurement. Solid arrows indicate the wire connection while the dashed arrow indicates the coil coupling. HI: hyperthermia insert. Rx coil: MPI receive coil. BSF: band stop filter. LNA: low noise amplifier.

coil mainly induces signal in x direction.

The magnitude of the transfer function can be used to calculate the transmitted power in the MPI receive chain after compensation. The measured transfer function has to be corrected for the gain of the low-noise amplifier at 700 kHz, which is around 47 dB and a factor of

$$\frac{\sqrt{R_{\mathrm{L}}^2 + (\omega L)^2}}{R_{\mathrm{L}}},$$

which arises due to the fact that the small signal evaluation has been performed by an unmatched coil and the heating will be performed with a matched coil. For an unmatched coil the RMS current through an electromagnetic coil is:

$$I_{\mathrm{test}} = \sqrt{\frac{P_{\mathrm{TX}}}{|Z|}} = \sqrt{\frac{P_{\mathrm{TX}}}{\sqrt{R_{\mathrm{L}}^2 + (\omega L)^2}}}, \tag{4.3}$$

where P_{TX} is the RMS power transmitted by the coil, R_{L} is the resistance of the coil, ω the angular frequency, L the inductance of the coil. For a matched coil, for instance using an impedance matching, the RMS current is calculated by:

$$I_{\mathrm{heat}} = \sqrt{\frac{P_{\mathrm{TX}}}{R_{\mathrm{L}}}} \tag{4.4}$$

The induced voltage in a coil due to an electromagnetic field is given by Faraday's law of induction and depends on the time-derivative of the magnetic field. The magnetic field depends on the geometry of the coil ensemble as well as the field generating current. Since the geometry is assumed not to change, it can be modeled as a factor σ. The induced voltage then depends solely on the time-derivative of the field generating current. The field-generating current is a sinusoidal current with

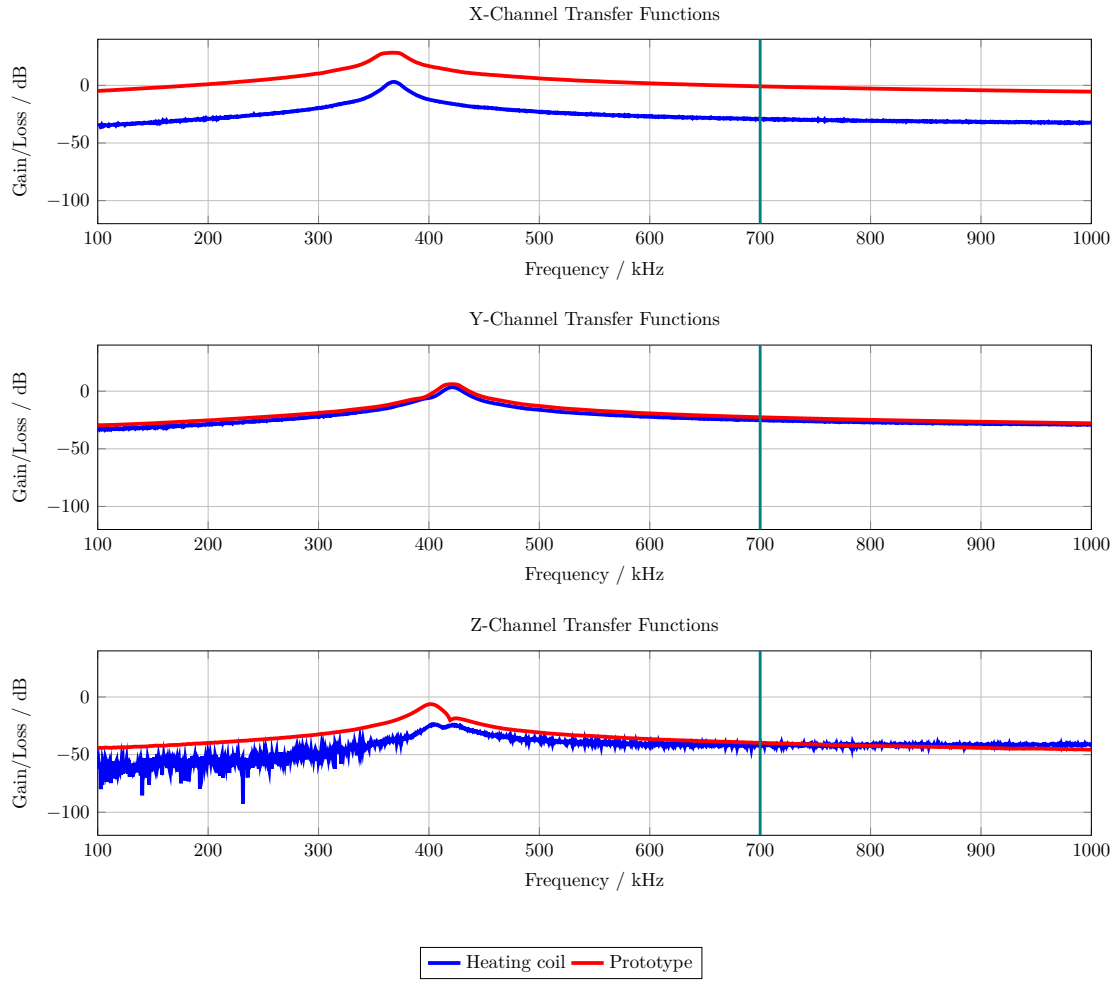

Figure 4.7: Transfer function from the insert prototype to the LNA output. The 700 kHz is marked by green lines. The transmitted power on x channel decreases due to self-compensation.

fixed angular frequency ω, hence:

$$\begin{aligned} U_{\text{testRX}} &= -\sigma \frac{\partial}{\partial t} \left(I_{\text{test}} \cdot \sin\left(\omega t\right) \right) \\ U_{\text{heatRX}} &= -\sigma \frac{\partial}{\partial t} \left(I_{\text{heat}} \cdot \sin\left(\omega t\right) \right) \\ \Rightarrow \frac{U_{\text{testRX}}}{U_{\text{heatRX}}} &= \frac{I_{\text{test}}}{I_{\text{heat}}} \frac{\frac{\partial}{\partial t}\left(\sin\left(\omega t\right)\right)}{\frac{\partial}{\partial t}\left(\sin\left(\omega t\right)\right)} = \frac{I_{\text{test}}}{I_{\text{heat}}}, \end{aligned} \tag{4.5}$$

where t is the time, U_{testRX} and U_{heatRX} are the voltages induced in the scanner from the test coil and the heating insert, respectively. The ratio of the powers

transmitted to the coil can then be calculated as

$$\begin{aligned}\frac{P_{\text{testRX}}}{P_{\text{heatRX}}} &= \frac{U_{\text{testRX}}^2}{Z_{\text{MPI}}} \frac{Z_{\text{MPI}}}{U_{\text{heatRX}}^2} = \frac{U_{\text{testRX}}^2}{U_{\text{heatRX}}^2} = \frac{I_{\text{test}}^2}{I_{\text{heat}}^2} \\ &= \sqrt{\frac{P}{\sqrt{R_{\text{L}}^2 + (\omega L)^2}}}^2 \sqrt{\frac{R_{\text{L}}}{P}}^2 \\ &= \frac{R_{\text{L}}}{\sqrt{R_{\text{L}}^2 + (\omega L)^2}} \end{aligned} \tag{4.6}$$

Finally, the correction factor for the transfer functions is given by

$$\frac{P_{\text{heatRX}}}{P_{\text{TX}}} = \frac{P_{\text{testRX}}}{P_{\text{TX}}} \frac{\sqrt{R_{\text{L}}^2 + (\omega L)^2}}{R_{\text{L}}}. \tag{4.7}$$

Table 4.3 shows the transmitted powers of the skeleton prototypes including the compensation winding compared to the power transmitted by the heating winding at the heating frequency of 700 kHz. Overall most of the power is effectively compensated, even though the transmitted power slightly increases in the z channel.

Table 4.3: The transmitted powers of the prototype compared to the power transmitted by the heating coil only at 700 kHz.

Channel	Prototype		Heating coil only	
	Gain/Loss level	Transmitted power	Gain/Loss level	Transmitted power
X	−93.78 dB	418.79 nW	−41.12 dB	77.27 mW
Y	−96.86 dB	206.06 nW	−62.89 dB	51.40 mW
Z	−112.32 dB	5.86 nW	−80.06 dB	9.86 µW

4.3 Implementation of the hyperthermia insert

Small signal measurements with the prototype in section 4.2.4 validate the coil topology design, therefore it is adopted for the coil system of the hyperthermia insert. However, the prototype can only work with small signals and cannot achieve the desired magnetic field strength for MFH. To allow high power on the coil system, a cooling unit has to be designed. In this section, the process of extending the prototype into the final hyperthermia insert with cooling is discussed.

4.3.1 Cooling of the coil system

To achieve the required field strength for good heating performance, high current and high voltage have to be applied on the coil. The current flows through the litz wire produces heat, whose power equals the product of the resistance of the litz wire and the square of the current:

$$P_{\text{heat}} = I_{\text{coil}}^2 R_{\text{coil}}. \tag{4.8}$$

According to the small signal measurement results with the prototype, $I_{\text{coil}} = 150\,\text{A}$ is needed to generate a magnetic flux density of 10 mT in the center of the coil. Carrying such high current, excessive heat will be generated in the litz wire despite its low impedance. The high temperature on the litz wire can cause deformation of the winding support parts and results in the change of the coil topology, which is essential to keep the self-compensation property of the insert. Furthermore, the insulation materials of the litz wire are with low temperature resistance, the litz wire has to be cooled properly to ensure the safe functioning of the insert. Therefore, a cooling unit is required to used the cooling system of the MPI scanner which cools the coil system with oil.

4.3.2 Cooling unit design

The cooling unit should contain the coil support structure to maintain the coil topology and ensure enough space for the oil flow to cool the whole coil system. As the insert has to fit in the imaging bore of the MPI scanner and should not influence the operation of the robot and the animal cassette used for imaging, the space for the cooling unit is limited. Figure 4.8 depicts the space limitation of the cooling unit.

The design of the cooling unit is shown in Figure 4.9. The cooling unit has one outer tube and one inner tube, the coil system is placed in the space between the two tubes. The diameter of the scanner bore and the small rat cassette are 119 mm and 59 mm respectively. Accordingly, the outer diameter of the outer tube and the inner diameter of the inner tube are 117.5 mm and 60 mm. The length of the cooling unit is around 245 mm to ensure enough space for the coil and the coolant. In order to have minimal influence on the animal cassette, which will be placed into the hyperthermia insert from the front side of the scanner, the coolant has to

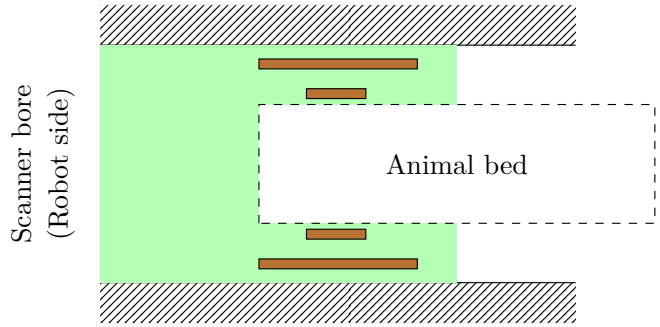

Figure 4.8: Space limitation of the cooling unit. The brown parts represent the winding of the coil system. The insert has to fit in the green area between the scanner bore and the animal bed.

flow in and out from the back side of the scanner. Therefore, the cooling inlet and outlet are designed both at the same end of the cooling unit. To prevent the coolant flows directly from the inlet to the outlet next to it and not cool all turns of the coil system, a tube-shaped separator is placed in between the heating coil and the compensation coil to guide the coolant flow to the end of the cooling unit. The coil topology is identical to the prototype. The heating coil is wound directly on the inner tube and the compensation coil is fixed on the separator. The compensation winding support parts are with cutouts to maximize the contacting surface to the coolant while maintaining the shape of the winding.

(a) CAD model of the coil support part of one compensation turn.

(b) CAD model of the cooling unit.

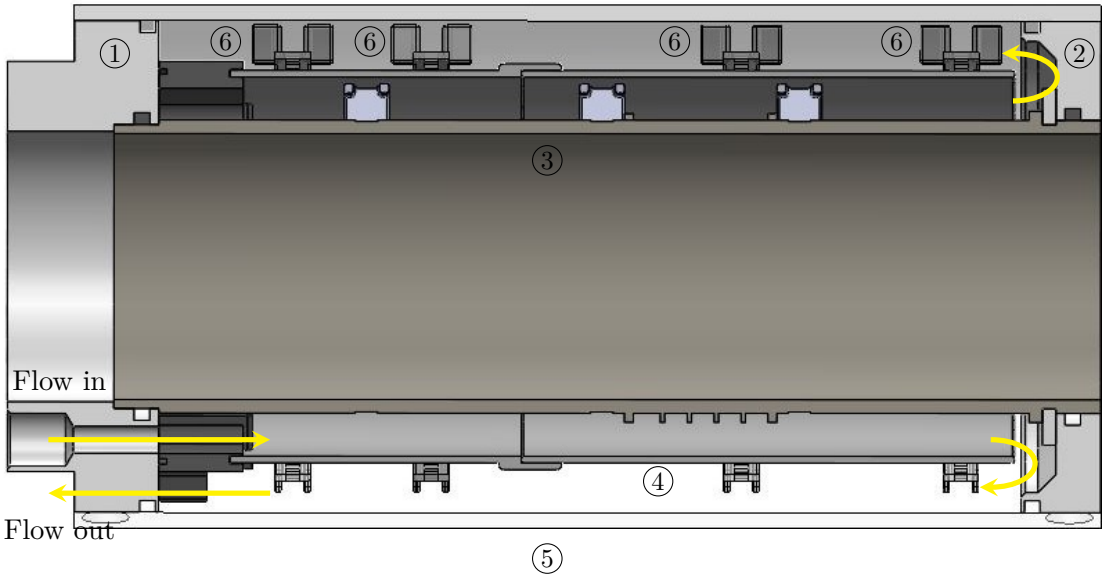

(c) Section view of the design of the cooling unit. The yellow arrows indicate the coolant flow. 1: Cover plate. 2: Bottom plate. 3: Inner tube. 4: Separator. 5: Outer tube. 6: Compensation winding supports

Figure 4.9: Design of the cooling unit. The heating coil is directly wound the inner tube. The compensation coil is wound on the coil support part (a) with cutouts, which is fixed on the seperator (b) through screws.

4.3.3 Manufacture of the cooling unit

The components of the cooling unit has to carry mechanical load, sustain thermal stress in high frequency magnetic field and oil surrounding environment. Therefore, suitable materials have to be chosen for the manufacturing of the cooling unit. Metal part and ferro-magnetic material should not be used to avoid inductive heating and unwanted MPI signals. Since oil will be used as the coolant, the material should be oil resistant. Due to the complexity of the components design, additive manufacturing and conventional subtractive manufacturing techniques are used to manufacture the cooling unit.

Additive manufacturing

The stereolithography (SLA) 3D printer Form 3 (Formlabs, Massachusetts, USA) is used to print the coil support parts and the separator. Stereolithography is one of the most widely used vat photopolymerization technologies, which creates objects by selectively curing a liquid form polymer resin using an ultraviolet (UV) laser beam. There are three main reasons that an SLA printer is chosen for manufacturing these parts. First, it offers printed objects with high accuracy and precision, which permits the fine structures of the coil support parts. Second, the SLA technique creates parts with the smoothest surface finish compared to other 3D printing processes, which is necessary to protect the unserved litz wire. Finally, there are a wide range of materials featuring different properties for printing. The separator is designed with 1.5 mm thickness to save space, which is a challenge for the subtractive manufacturing but possible to achieve with 3D printing. The separator has been divided into two parts and printed separately to fit the print volume of the 3D printer. The complex fine structure of the compensation winding supports can be realized with 3D printing. The printed parts are also light-weighted, which is beneficial since the compensation winding is fixed on the separator, therefore should not exceed the maximum weight that the separator can hold. High Temp resin is used for the winding support since it can sustain temperature up to 210 °C and can be used safely to have direct contact with the litz wire. 3D printing helps to lower production times and costs significantly compared to subtractive machining of the parts.

Subtractive manufacturing

Compared to additive manufacturing, subtractive manufacturing can deliver objects with tight tolerances and better surface finishes. It is more suitable for larger, less complex objects and those are subject to more extreme mechanical stress and strain. The inner tube, outer tube, top plate and bottom plate have to sustain pressure of the MPI cooling system up to 1 bar and have high accuracy to ensure that there is no leakage of the coolant. Besides, these parts have simple geometry and therefore is suitable to be subtractive manufactured. 3 mm thick polymethyl methacrylate (PMMA) pipes are used to build the inner and outer tube. The biggest advantage of PMMA is its excellent light transmittance, which allows the observation of the space between the two tubes. PMMA is also a tough, durable and lightweight material, that can provide good protection of the coil structure which is placed in between of the two tubes. The top and bottom plates are made of polyoxymethylene (POM), which has high mechanical strength, rigidity, excellent resilience and recovery elasticity.

Assembly process

The manufactured parts are assembled together to build the final hyperthermia insert. At first, the heating coil is wound on the inner tube. The voltage on the coil can be calculated by

$$U_{\text{coil}} = \omega L_{\text{coil}} I_{\text{coil}}, \tag{4.9}$$

which is 2168 V. With 9 turns of the coil, voltage drop between each turn is then around 240 V. Considering the small distance between each turn of the heating coil winding, extra insulation film is placed in between of the turns to prevent electrical breakdown and sparking. After that the separator with the compensation winding supports is fixed on the cover plate and the litz wire is placed on the support parts. The litz wire is fixed using nylon strands on the support parts at the begin and end of each turn. O-rings are seated in the groove of the cover and bottom plate and compressed during assembly, forming a seal between the inner and outer tube. Polyetheretherketone (PEEK) screws are used to fix the cover and bottom plates, offering excellent mechanical strength to fix the components of the cooling unit when sustaining pressure.

Figure 4.10 shows the first version of the hyperthermia insert. Because of the

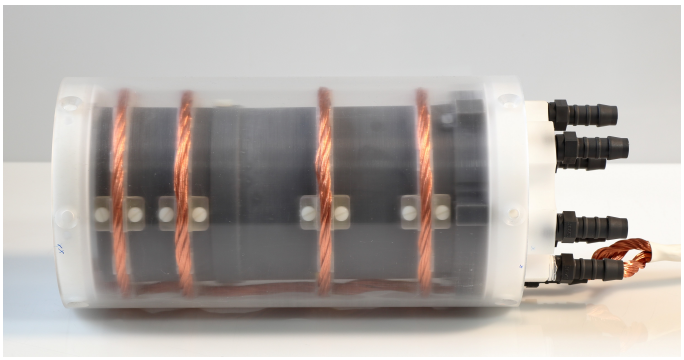

Figure 4.10: The first version of the hyperthermia insert with the coil support printed using high temp material and the separator printed using gray material.

separator (gray part) between the heating coil and the compensation coil, the heating coil winding cannot be seen. To make it visible, the material of the separator is changed to clear resin, which has high transmittance. Besides, the material of the compensation winding support has to be changed because that the high temperature material is very brittle and breaks easily during the insert assemble possess. Therefore, the standard gray resin has been used, which is less brittle and shows no deflection up to 100 °C under experiment conditions.

4.3.4 Temperature sensor

To ensure the coil system is cooled properly when high power is applied, a temperature sensor is used to monitor its temperature. A platinum resistance temperature detector (RTD) PT100 (C220, Heraeus Nexensos GmbH, Germany) is chosen in this work. RTD changes resistance at a predetermined rate in response to changes in temperature. PT100 has a resistance of 100 Ω at 0 °C and 138.5 Ω at 100 °C. It features ± 0.1 °C measurement accuracy and a measurement range from −65 °C to 650 °C. When measuring in the alternating magnetic field, optical rather than electronic temperature sensors are often used to avoid eddy current self-heating in conducting parts. However, eddy current heating is strongly dependent on the size and geometry of the conducting part [74]. The PT100 used in this work is a thin-film RTD with the size of 2.3 mm × 1.9 mm × 1 mm and is placed parallel to the magnetic field generated by the heating coil insert to minimize the eddy current heating caused by the alternating magnetic field (AMF). The temperature sensor is placed beside the heating coil, where is

expected to be the hottest position. It is fixed on a 3D printed holder which locates between the separator and the inner tube through a hole on the cover plate. The temperature sensor can be exchanged in case of defect by taking the holder out without disassemble the whole insert.

4.3.5 Connector to impedance matching

The connection wire of the coil system connects to the impedance matching network, which has to be cooled will oil and should be conveniently disconnected from the impedance matching network. Figure 4.11 shows a connector built for this purpose. The connector is composed of two separated chambers that connect to the cooling unit inlet and outlet by pipes. The litz wire from the cooling unit goes into the two chambers through the pipes and connects to the copper bars which stick into the chambers. Another two copper bars from the impedance matching network are connected to them by a copper clamp. With the connector the entire litz wire are cooled with oil and the hyperthermia insert can be connect and disconnected from the impedance matching network by simply plugging in and out the connector.

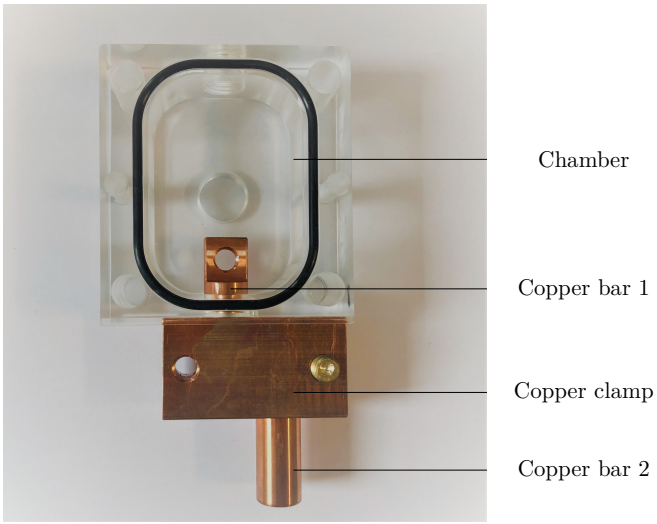

Figure 4.11: One chamber of the connector. The litz wire connects to the copper bar1 in the chamber. The copper bar 2 connects to the impedance matching network. Copper bar 1 and 2 are connected by the copper clamp.

4.3.6 Leak test

The hyperthermia insert has to be leak prove, which is validated by leak test of the implemented insert using the underwater method. 3 bar pressure is applied on the cooling unit and the whole insert has been placed beneath water, no visible bubble has been observed. After 1 hour, the pressure on the insert remains 3 bar, which indicates there is no leakage in the insert.

The final hyperthermia insert is shown in Figure 4.12. In oil, all the components including the litz wire, the temperature sensor and the winding support can be seen through the inner and outer tubes. The usage of transparent materials ensures the correct fit of all parts including the litz wire during the assembly process and enables visual inspection of the system for air bubbles in the oil.

4.4 Impedance matching network

In order to ensure the maximum power transfer between the amplifier and the hyperthermia insert coil, the impedance matching network has to be designed, which matches the load impedance to the source impedance of the amplifier:

$$Z_{\text{load}} = Z_{\text{source}} \tag{4.10}$$

The amplifier used to generated the signal for the hyperthermia insert has a real source impedance $Z_{\text{source}} = R_{\text{source}} = 50\,\Omega$. In contrast, the impedance of the insert coil is

$$Z_{\text{load}} = R_{\text{coil}} + i\omega L_{\text{coil}} = 0.44 + 12.97i\ \Omega \tag{4.11}$$

at 700 kHz, which is almost purely imaginary. In this section, the design and implementation of the impedance matching network to match the insert coil to the $50\,\Omega$ source impedance are discussed.

4.4.1 Circuit design

The impedance matching is of the type LCC impedance matching. The inductor of the LCC impedance matching is the field generating coil, which is matched to the power amplifiers optimal load by a series capacitor and a parallel capacitor.

(a) Front view of the hyperthermia insert.

(b) Right view of the hyperthermia insert.

Figure 4.12: The implemented hyperthermia insert cooled with oil. The coil system and the temperature sensor can be seen through the transparent outer tube, inner tube and separator.

As shown in Figure 4.13, at first a capacitor C_s is connected in series to the insert coil, the impedance of the branch is

$$Z_\mathrm{branch} = R_\mathrm{coil} + i\omega L_\mathrm{coil} - \frac{i}{\omega C_\mathrm{s}}. \tag{4.12}$$

Then the second capacitor is added in parallel, the load impedance is now given by

$$Z_\mathrm{load} = \frac{1}{\frac{1}{Z_\mathrm{branch}} + i\omega C_\mathrm{p}}, \tag{4.13}$$

which should be equal to $50\,\Omega$. The value of C_s and C_p can be obtained by first calculating the reactance of the series capacitor X_CS and the parallel capacitor X_CP

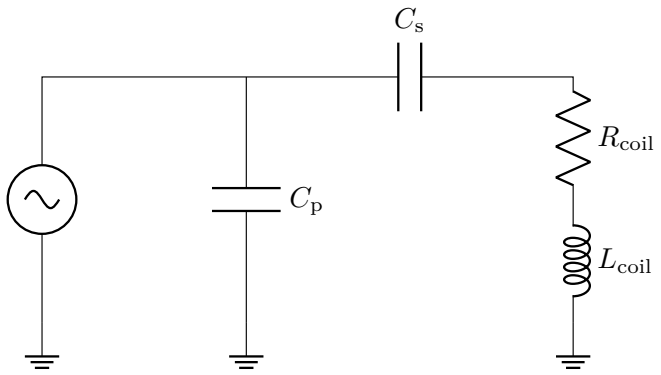

Figure 4.13: Impedance matching network circuit design with one series capacitor and one parallel capacitor.

using the following formulas

$$X_{CS} = \sqrt{R_S}\sqrt{Z_{src} - R_S} - X_{LS} \tag{4.14}$$

and

$$X_{CP} = -\sqrt{R_S}\frac{Z_{src}}{\sqrt{Z_{src} - R_S}}, \tag{4.15}$$

where R_S and X_{LS} are the resistance and the reactance of the magnetic field generating coil, respectively. The output impedance of the power amplifier is given by Z_{src}. The capacitance value C can afterwards be achieved from the reactance X using the relation

$$C = -\frac{1}{\omega X} \tag{4.16}$$

where ω is the angular frequency of the magnetic field. With the heating frequency of 700 kHz, the value of the series and parallel capacitor are 21.18 nF and 153.2 nF respectively.

4.4.2 Implementation of the impedance matching network

The CSM 150/300 capacitors (Celem power capacitors, Israel) are used to build the impedance matching network. The capacitors can work under high power at radio frequency range. Due to the limited available capacitance, several 50 nF and 100 nF capacitors are connected in series or parallel to achieve the desired values. At 700 kHz, the current and voltage rating of the two types of capacitor are 220 A_{rms} and 1000 V_{rms}, 300 A_{rms} and 690 V_{rms} receptively. According to simulation, the maximum current and voltage on each capacitors are shown in Table 4.4, which

are below the current and voltage ratings. The low inductance and low resistance connections are necessary for the capacitor bank. Therefore copper plates with cross section of 2 mm × 220 mm are used for the connection to have larger conducting surface. Similar to the hyperthermia insert, the impedance matching network has to be integrated into the MPI scanner, therefore the capacitor bank has to fit into a copper shielding box of size 300 mm × 280 mm × 102 mm.

Table 4.4: Current and voltage on each capacitors when generating 10 mT at the center of the heating coil.

Capacitor	Current/V_{rms}	Voltage/V_{rms}
C_{s1}	115	262
$C_{s2,3}$	115	522
$C_{p1,2,3}$	42	192

4.4.3 Cooling of the capacitors

The dielectric material used by the capacitors - polypropylene - can safely run at temperatures of up to 90 °C. The temperature gradient between the hottest points of the polypropylene element and the copper surface of the capacitors is 40-45 °C. Therefore, external surfaces of the capacitors must not exceed 45 °C. To ensure the proper work of the capacitors, both sides of the upper contacts surface copper are pressed in contact with copper plates with thermal conductive paste in the contacting surface. The copper plates are cooled with oil and served as a heat sink.The CAD model of the capacitor bank with cooling and the implemented impedance matching network is shown in Figure 4.14.

Since both the hyperthermia insert and the impedance matching network are connected in the cooling system of the MPI scanner, there are two types of connection as shown in Figure 4.15. The cooling flow rate is determined by the connection method and the flow resistance of the hyperthermia insert and the impedance matching network R_{Insert} and R_{IM}. Due to the fact that $R_{\mathrm{Insert}}$is much higher than R_{IM}, when using the parallel connection most oil flow into the impedance matching network and the hyperthermia insert cannot be cooled properly. Therefore, the capacitor bank is cooled in series with the coil and is cooled first due to the higher loss of the coil.

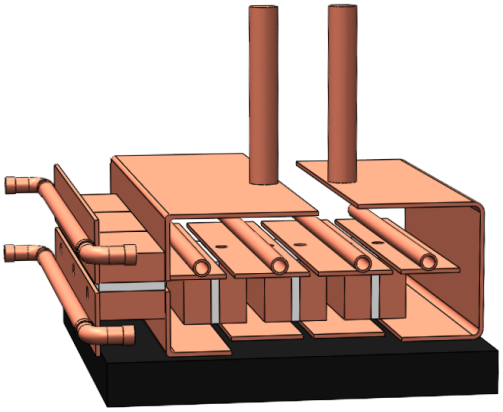

(a) CAD model of the capacitor bank, some cooling pipes are not shown. The capacitors are cooled through the copper pipes soldered on the copper plates. The two copper bars are the pins connect to the hyperthermia insert.

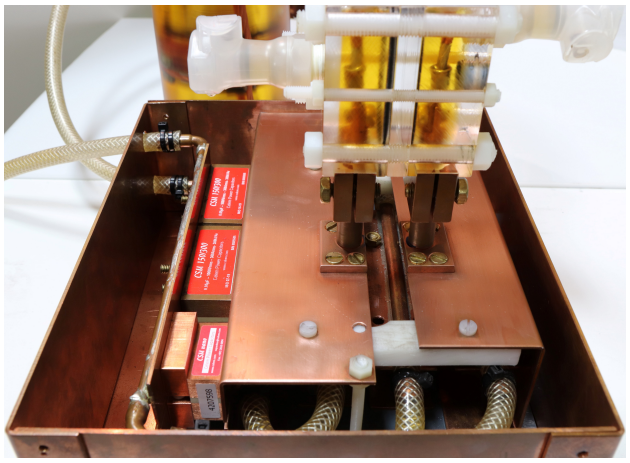

(b) Implemented impedance matching network (without cover). The transparent block connects to the copper plate is the connector of the hyperthermia insert.

Figure 4.14: CAD model of the capacitor bank and the implemented impedance matching network.

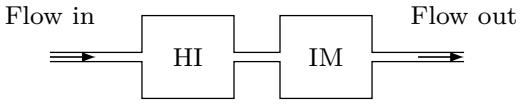

(a) Seires connection.

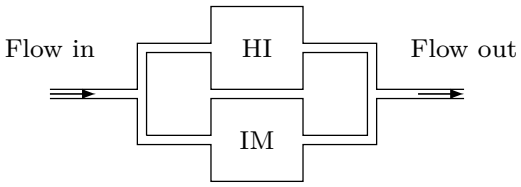

(b) Paraplell connection

Figure 4.15: Two different connection of the hyperthermia insert and the impedance matching network to the cooling system. HI: Hyperthermia insert. IM: Impedance matching network

4.5 Evaluation of the hyperthermia insert

In this section, the hyperthermia insert is evaluated regarding the electrical and magnetic characteristics, cooling capability, field strength, the magnetic coupling to the MPI system's and particle heating.

4.5.1 Electrical characteristics

To evaluate the electrical characteristics of the hyperthermia insert, the induction and the series resistance and other parameters of the coil system are measured. The results are shown in Table 4.5.

Table 4.5: Electrical characteristics of the hyperthermia insert.

Inductance	2.9 µH
Resistance	44 mΩ
Capacitance C_S	20.1 nF
Capacitance C_P	140 nF
Resonant frequency	698.6 kHz
Impedance @ resonant frequency	45 Ω

The capacitors for the impedance matching C_S and C_P are not exactly the same as the designed values. Therefore the working frequency and the load impedance has shifted from 700 kHz and 50 Ω to 698.6 kHz and 45 Ω. However the value is still in the acceptable range that the influence on the application in this work can be ignored.

4.5.2 Decoupling effect

The decoupling effect of the implemented hyperthermia insert is evaluated using the same method presented in section 4.2 and compared to the results measured with the prototype in Figure 4.16. Similar results are obtained for the x and y channel, while on the z channel the hyperthermia insert shows less decoupling effects due to the coupling of the connection wires. The litz wire connects the heating coil and the compensation coil forms a loop which acts like a coil and induces signal in the MPI receive chain. In the prototype, the connection wires are twisted, which minimizes the coupling effect. In the case of the hyperthermia insert, the separator is placed in between of the heating coil and the compensation coil, therefore the connection wires form a loop on the xz plane, which couples into the z channel.

4.5.3 High power test

To test the performance of the hyperthermia insert under high power, a radio frequency power amplifier (AG 1012, T&C Power Conversion, Inc., USA) is used to send power to the insert. The amplifier output is connected to the impedance matching network for optimal power transmission. The amplifier sends 600 W sinusoidal signal at the resonant frequency 698 kHz for 60 s. During the test, the current flows through the coil is measured by a current probe (MiniFlex MA200, Chauvin Arnoux, France) and the voltage on the coil are measured by a voltage probe (high voltage probe, Teledyne LeCroy, USA). The peak current and voltage on the coil is 160 A and 2.25 kV, respectively.

The temperature of the hyperthermia insert is monitored by the temperature sensor PT100 (section 4.3.4) and a fiber optic temperature probe (PRB-400, OSENSA Innovation Corp, Canada) during the test. The tip of the fiber optic probe is fixed at the inner tube wall where the heating coil is wound, where is expected to be

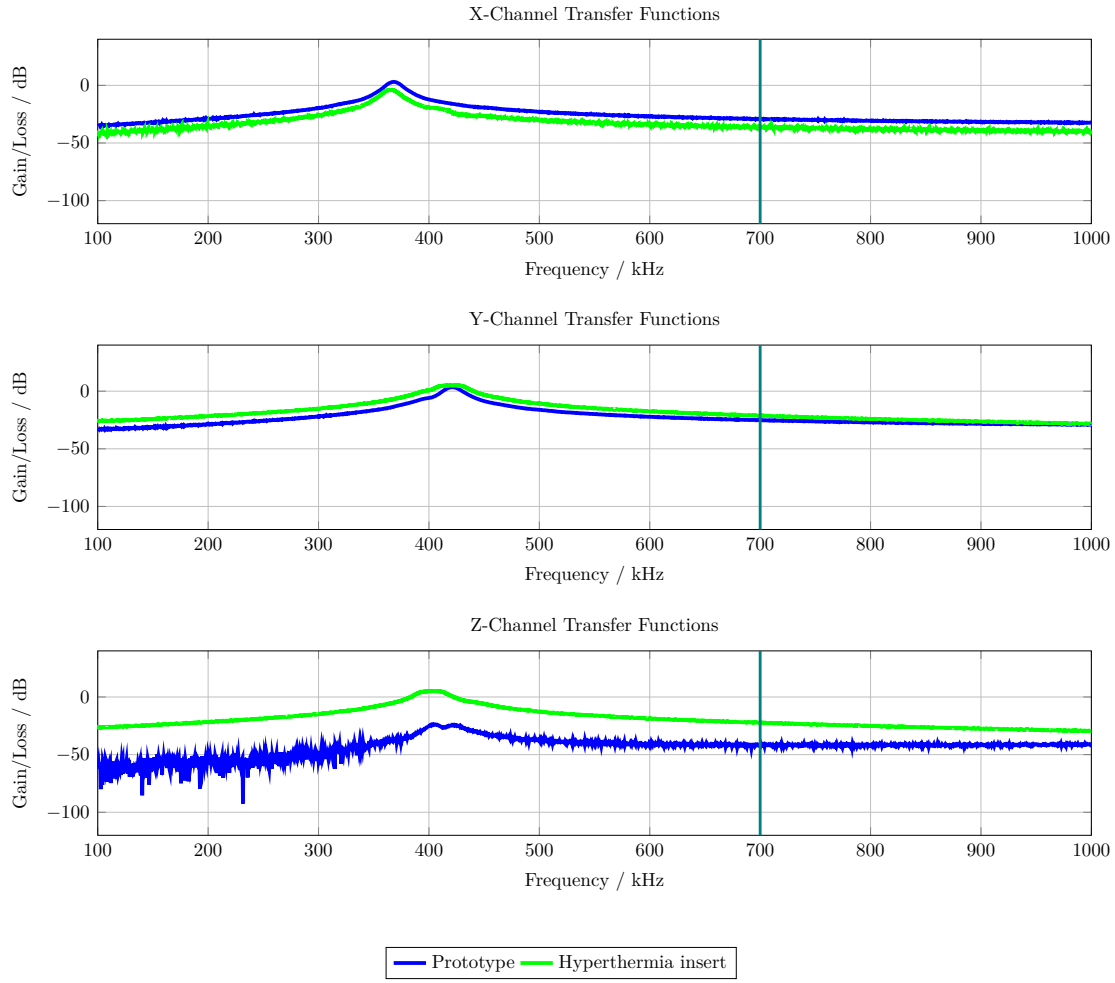

Figure 4.16: Transfer function from the hyperthermia insert to the LNA output. Similar results as the prototype are measured, except for the z channel.

the hottest point when high power is applied. The temperature measured by the PT100 and the fiber optic probe is plotted in Figure 4.17. Since the PT100 is placed beside the heating coil winding, the temperature increases immediately as the power is applied and drops rapidly after 60 s due to the cooling. In contrast, the inner tube is heated up due to the heat conducted form the litz wire, therefore the temperature measured by the fiber optic probe presents a time delay to the results of the PT100. Besides, the temperature of the inner tube arises and drops slower and reaches a lower maximum temperature.

The surface temperature of the capacitors are monitored by an infrared camera (testo 875-1, Testo SE & Co. KGaA, Germany). The maximum temperature of both series and parallel capacitors are below 35 °C during the test.

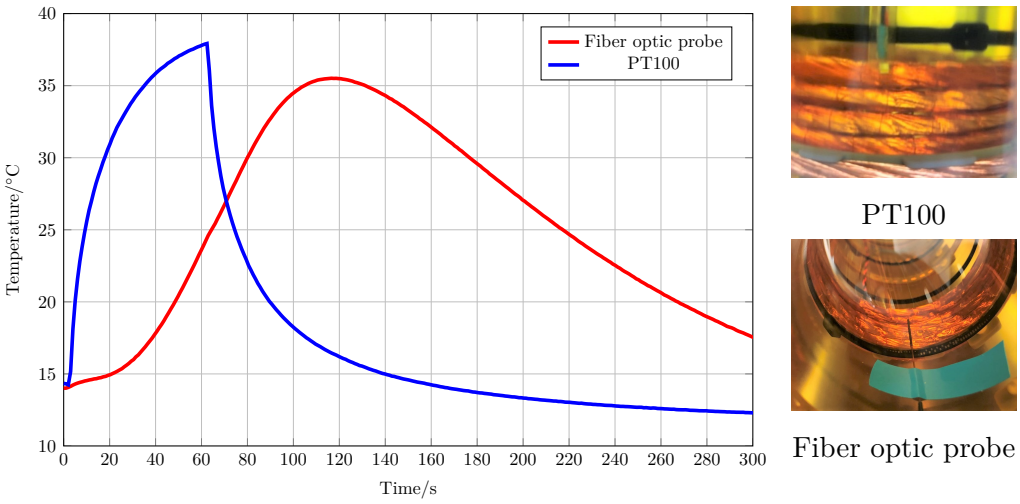

Figure 4.17: The temperature of the hyperthermia insert measured by the PT100 and the fiber optic probe for 60 s when 600 W power is applied. The pictures show the sensor location of the two measurement methods.

4.5.4 Cooling capability

To verify the safe operation limits with respect to the cooling effect, different powers are applied to the hyperthermia insert. While the power is applied, the temperature of the hyperthermia insert is measured. The temperature sensor PT100 has to work with a special temperature readout device, therefore for simplicity the fiber optic temperature probe is used for the tests. A flow meter is connected in series to the cooling system to measure the cooling oil flow rate. The conditions to end the test are a stable temperature over a time of 3 min or the coil reaching a temperature of 60 °C. In case the temperature limit is reached, the time until the temperature is reached is noted. Thus, a duty cycle for heating applications can be determined. At a certain power level, the system is defined as stable when it can work continuously for 180 s, otherwise the system is defined as unstable. The results from 10 W to 600 W are shown in Table 4.6.

According to the results, the insert can work stably up to 400 W, reaching around 84% of the desired maximum field strength. At the maximum power of 600 W, the temperature limit is reached after 90 s. The flow meter indicates the oil flow rate is less than 1 LPM (liter per minute). To increase the continuous working time of the hyperthermia insert, modifications are made on the cooling system design to

improve the cooling capacity. The inner diameter of the hose coupling used in the hyperthermia insert is increased from 6 mm to 9.5 mm. Accordingly, the diameter of the hoses which connect to the cooling unit is increased from 9.6 mm to 12 mm . The modifications reduces the flow resistance for oil and thus increases the flow rate from less than 1 LPM to 3 LPM. In Table 4.6, the increasing of flow rate reflects on improved cooling performance of the upgraded cooling unit. At the same power level, it takes longer to reach the limit temperature and requires less time to cool down. The maximum power that the insert can work stable increases to 475 W.

The cooling effect is further tested in interleave manner for 5 heating/cooling cycles. In the heating cycle 600 W is applied while in the cooling cycle the power is removed. The temperature of the insert of the original and upgraded system is shown in Figure 4.18. With the 60 s heating cycle for both tests, the upgraded system requires 240 s to fully cool down the insert, which is 60 s less compare to the 300 s of the original one. Besides, the upgraded system has an lower temperature overall and works more stable given that the maximum temperature maintain the same for each cycle.

4.5.5 Magnetic field

The alternating magnetic field can be measured using induction coils. Changing magnetic fields induce a voltage in a coil, depending on field frequency and strength. According to Faraday's law of induction, the induced voltage in the coil can be calculated by the number of turns of the coil multiple the instantaneous change in flux:

$$U(t) = -N\frac{d\Phi}{dt} = -N\frac{dB(t)A}{dt} \tag{4.17}$$

where B is the magnetic field flux density and A is the coil area. The insert generates an alternating field with sinusoidal waveform at frequency f, which can be described as

$$B(t) = B\sin(2\pi ft). \tag{4.18}$$

Therefore, the induced voltage can be writen as

$$U(t) = U_{\text{amp}}\sin(2\pi ft) \tag{4.19}$$

and the field strength can be obtained by

$$B = \frac{U_{\text{amp}}}{2\pi fNA}. \tag{4.20}$$

Power/W	Original cooling unit			Upgraded cooling unit		
	T/ °C	duration/s	condition	T/ °C	duration/s	condition
10	15	600	stable	16	600	stable
20	16	600	stable	16	600	stable
30	16	600	stable	16	600	stable
40	18	600	stable	16	600	stable
50	19	600	stable	17	600	stable
75	24	600	stable	20	600	stable
100	28	600	stable	24	600	stable
125	30	600	stable	28	600	stable
150	33	600	stable	31	600	stable
175	36	600	stable	34	600	stable
200	42	600	stable	38	600	stable
225	43	300	stable	37	300	stable
250	46	300	stable	40	300	stable
275	48	300	stable	42	300	stable
300	50	300	stable	44	300	stable
325	48	180	stable	47	300	stable
350	50	180	stable	40	180	stable
375	52	180	stable	42	180	stable
400	57	180	stable	43	180	stable
425	44	145	unstable	44	180	stable
450	47	130	unstable	47	180	stable
475	60	125	unstable	50	180	stable
500	60	115	unstable	50	160	unstable
525	60	110	unstable	50	155	unstable
550	60	100	unstable	50	150	unstable
575	60	95	unstable	50	135	unstable
600	60	90	unstable	50	130	unstable

Table 4.6: The coil hot-spot temperature over time with different power levels on the hyperthermia insert.

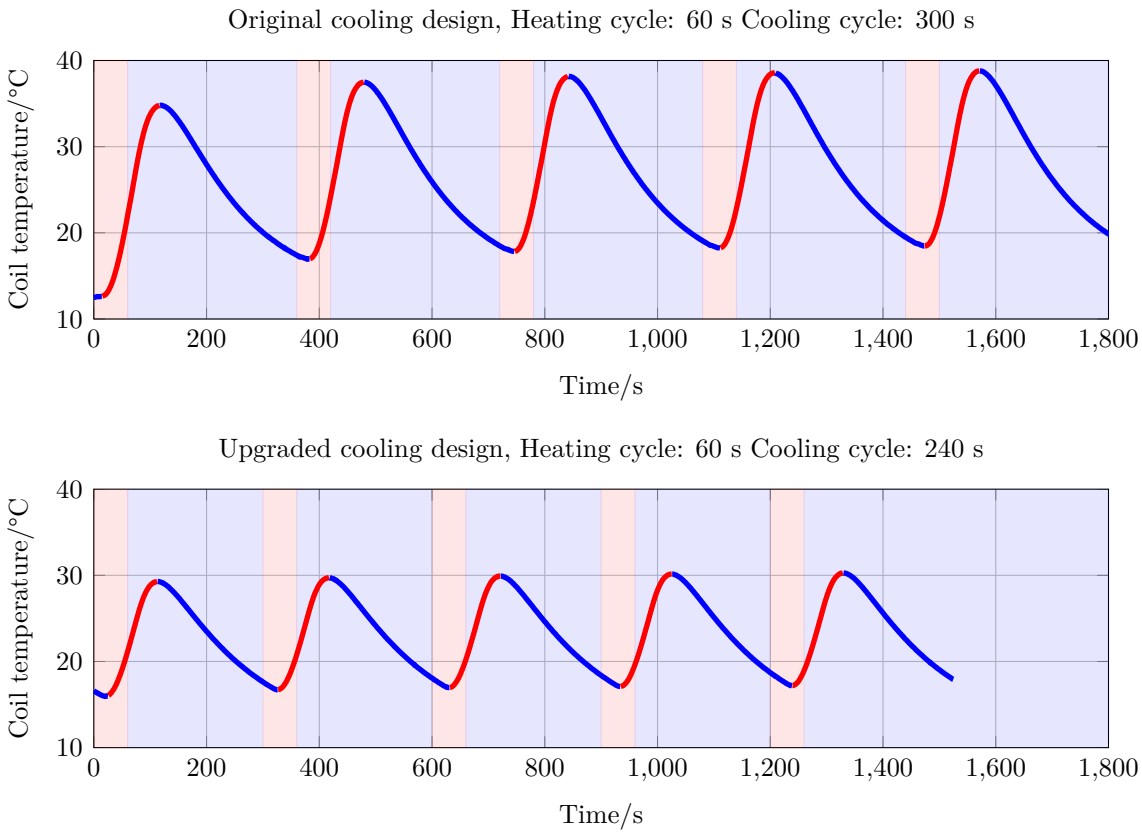

Figure 4.18: Temperature change of the hyperthermia insert over 5 heating/cooling cycles with the original and upgraded cooling unit design. The background filled with red and blue implies the heating and cooling cycles. The curve marked with red and blue are the period that the temperature increases and decreases. Delay of the temperature changes can be observed because the heat conduction time from the coil to the inner tube of the hyperthermia insert.

A 1D measurement coil with 10 turns and a diameter of 2 mm diameter is used to measure the field at the center of the heating coil on the x direction. The results with different power levels from 10 W to 600 W are shown in Figure 4.19. To compare the field generated by the hyperthermia insert and the prototype, the field strength with 170 A current is measured at different positions and compared with the field profile of the prototype in Figure 4.20. Due to the space limitation of the measurement coil, only the field along the x axis from -9 mm to 9 mm away from the center is measured. The field strength is above 11 mT at all measured positions. The measured field matches the result of the prototype, which means the hyperthermia insert is capable to generate the expected alternating field strength.

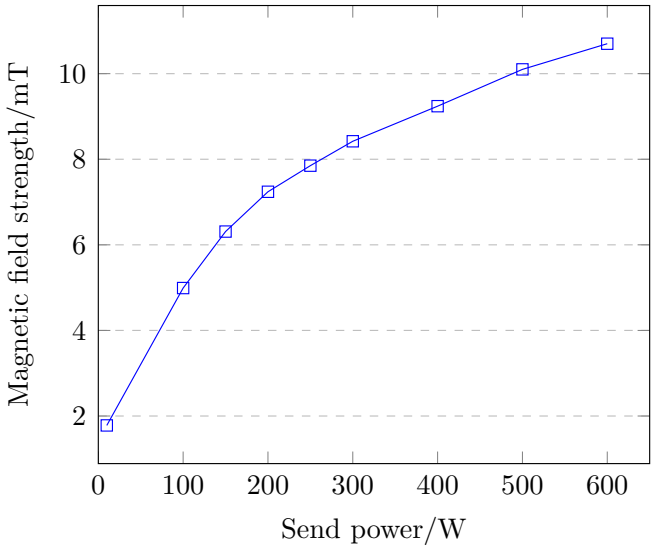

Figure 4.19: Magnetic field strength at the center of the MPI scanner with different send power level. The field strength increases in square root relation with the power on the hyperthermia insert. 10 mT is reached with 500 W.

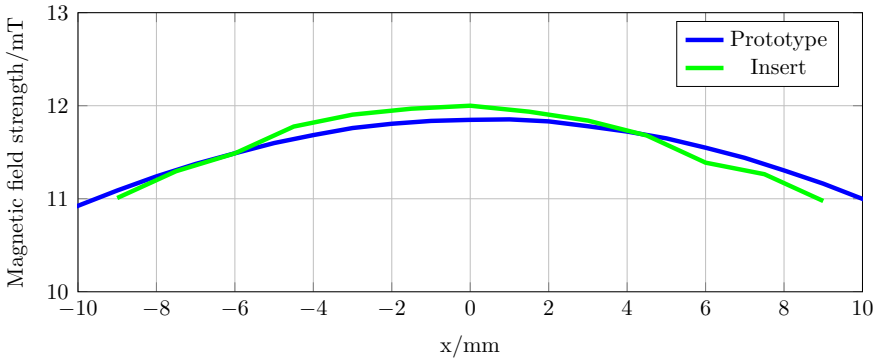

Figure 4.20: The magnetic field generated by the hyperthermia insert with 600 W along the x axis. The DC measurement result using the prototype is shown as comparison. The field profile of the hyperthermia insert fits well with the results of the prototype.

4.5.6 Stability test

The hyperthermia insert should work stably during working cycles, which means to generate the 700 kHz magnetic field at a constant field strength according to

the applied power. To test the stability of the insert, the magnetic field generated by it is monitored for 25 minutes by measuring the induced voltage in the same measurement coil used in Figure 4.5.5. During the 30 minutes, 600 W is applied on the insert in interleave manner for 5 heating/cooling cycles. The signal induced in the measurement coil is recorded at sample rate of 1.5 MHz to recover the waveform. The amplitude of the measured signal and its FFT result in the heating cycle are shown in Figure 4.21. A slight overshoot is observed when enabling the amplifier output. The field increased gradually after that and reaches the highest amplitude when the heating cycle finishes. The result is as expected since the reverse power is the largest at the beginning of the heating cycle and decreases when the system is heated up by the power applied. In the cooling cycle only noise is measured in the coil. No spikes are observed during the 25 minutes. The FFT result shows the frequency of the measured signal is 706.1 kHz, which matches the signal frequency sent by the RF power amplifier.

4.5.7 Particle heating

The capability of the hyperthermia insert to heat up MNPs is tested with Synomag-D 70 (micromod Partikeltechnologie GmbH, Germany) and Resovist (Bayer Schering Pharma AG, Germany) particles. The particle sample is placed in the center of the insert using a commercially available small rat cassette. The temperature of the particle solution is measured with the fiber optic probe. For all the measurements, water samples which have the same volume of the particle samples are used as the neutral reference. The temperature increase of the water was subtracted from the temperature of the particle to remove the effect of the heat dissipation from the coil.The measurement set up is shown in Figure 4.22.

Interleaved heating

To evaluate the interleaved heating, a 200 µL Resovist particle sample is heated with 600 W for 5 heating/cooling cycles (60 s heating and 240 s cooling). The change of the sample temperature is recorded and shown in Figure 4.23. The particles are heated up immediately when the heating cycle starts and cool down during the cooling cycles. During one heating cycle, the particle has been heated up for around 21 K. The maximum temperature that the particle can reach increases for 7.1 K in

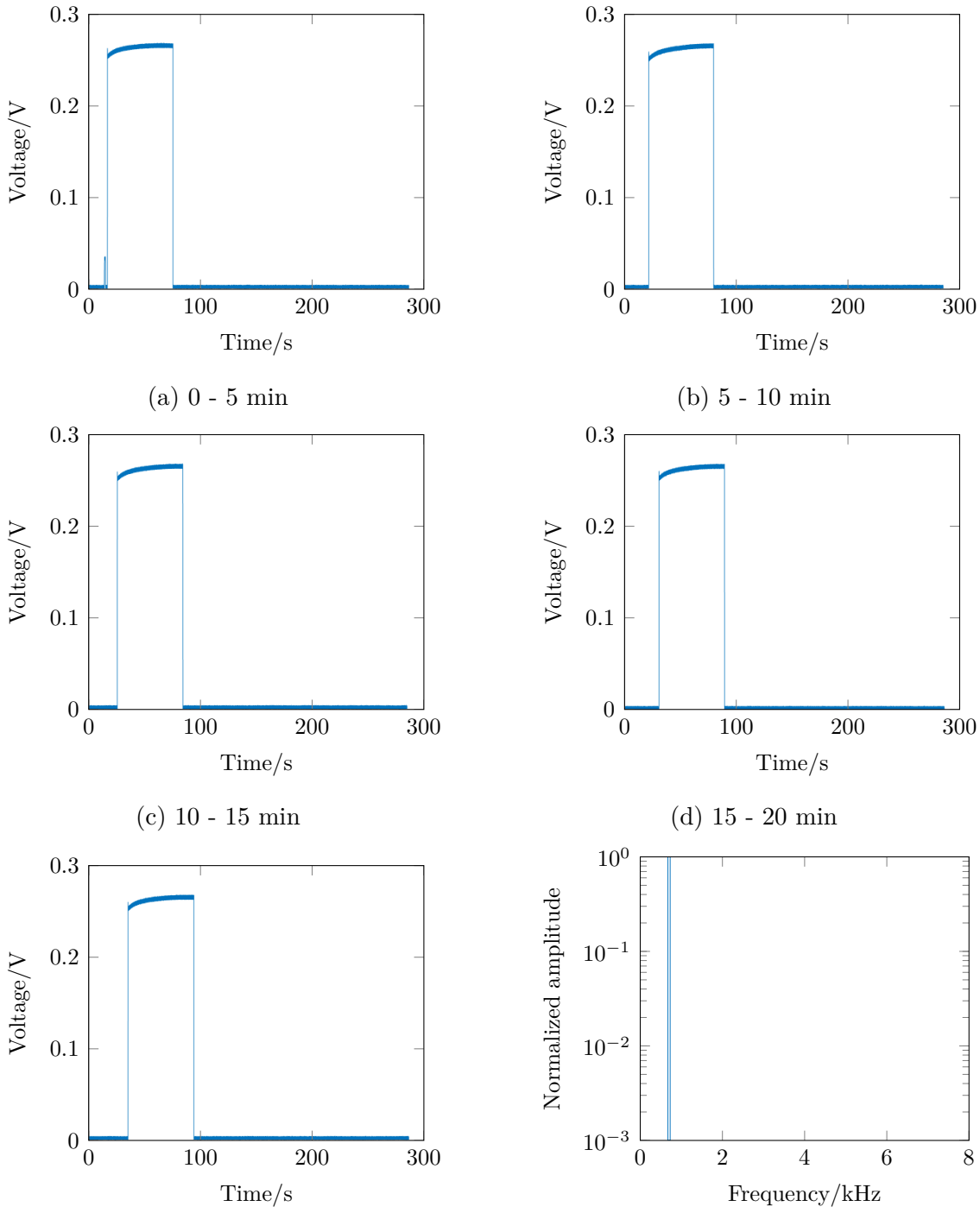

(a) 0 - 5 min

(b) 5 - 10 min

(c) 10 - 15 min

(d) 15 - 20 min

(e) 20 - 25 min

(f) Signal spectrum.

Figure 4.21: Amplitude of the induced voltage in the measurement coil during the stability test. Before the first heating cycle the amplifier sends 10 W to test whether the load matches, which is reflected on the small peak in (a). The FFT result of the induced signal in one heating cycle is shown in (f).

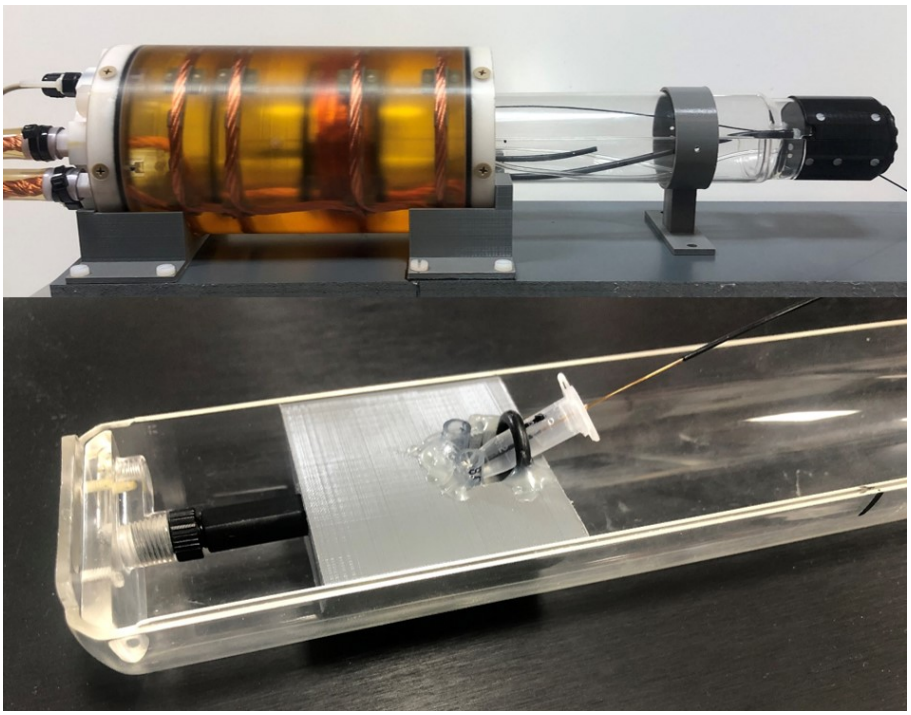

Figure 4.22: Setup of the particle heating measurement. The particle sample is fixed in the small rat cassette using a 3D printed part. The optical fiber is placed in the particle solution through a hole in the eppendorf tube.

the fifth heating cycle compared to the first heating cycle.

SAR

The particle heating effectiveness of different field strength is evaluated by measuring the specific absorption rate. 27 µL undiluted Synomag-D 70 nm particle sample (iron concentration 10 mg/mL is heated with different field strength by varying the send power. For each test, the sample is heated for 30 s and the temperature change of the sample is recorded. The SAR of the sample can be obtained from the measured particle temperature data using:

$$SAR = \frac{C_{\mathrm{w}} m_{\mathrm{w}} + C_{\mathrm{p}} m_{\mathrm{p}}}{m_{\mathrm{p}}} \cdot \frac{\Delta T}{\Delta t} \tag{4.21}$$

where T is the measured temperature, t is the time elapsed. $C_{\mathrm{w}} = 4190\,\mathrm{Jkg^{-1}K^{-1}}$ is the specific heat capacity of water, $C_{\mathrm{p}} = 670\,\mathrm{Jkg^{-1}K^{-1}}$ is the specific heat capacity

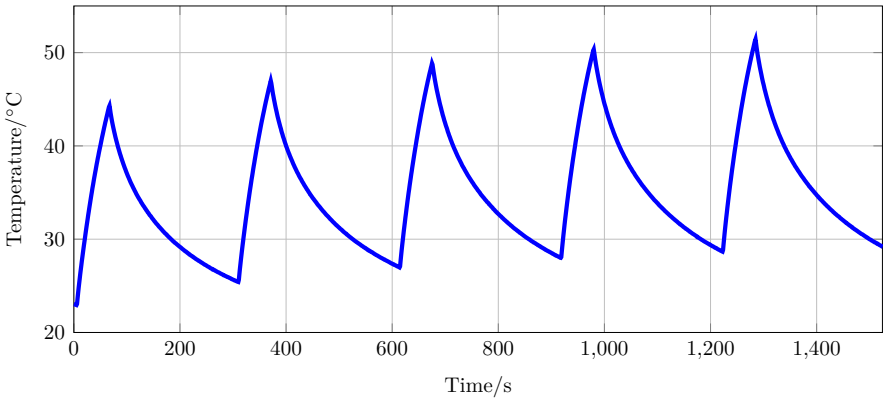

Figure 4.23: The change of 200 µL undilute Resovist (iron concentration 28 mg/ml) particle temperature during the 5 heating/cooling cycles.

of the particle [75], m_{w} and m_{p} are the mass of water and magnetic particles in the sample.

The temperature increases of the MNP sample ΔT_{p} and the water sample ΔT_{w} were obtained by subtracting the initial temperatures from the measured temperature:

$$\Delta T_{\mathrm{p,w}} = T_{\mathrm{p,w}}(t) - T_{\mathrm{p,w}}(0).$$

Subsequently, the temperature increase of the water blank sample was subtracted from that of the MNP sample, resulting in the net temperature increase,

$$\Delta T_{\mathrm{net}} = T_{\mathrm{p}}(t) - T_{\mathrm{w}}(t).$$

The temperature increasing rate $\frac{\Delta T}{\Delta t}$ can be estimated from the slope of the net temperature increase. Theoretically, the should be measured under adiabatic conditions, which is experimentally unachievable because some heat transfer always occurs across the sample-environment boundary. An approximation method [76] is used here to identify the quasi-adiabatic heating conditions in the heating experiment. The following values are calculated:

- Slope of the linear fit of the net temperature increase.
- Mean value of the first derivative of the net temperature increase at each time step.
- Y-intercept of the linear least square fit of the first derivative of the net temperature increase.

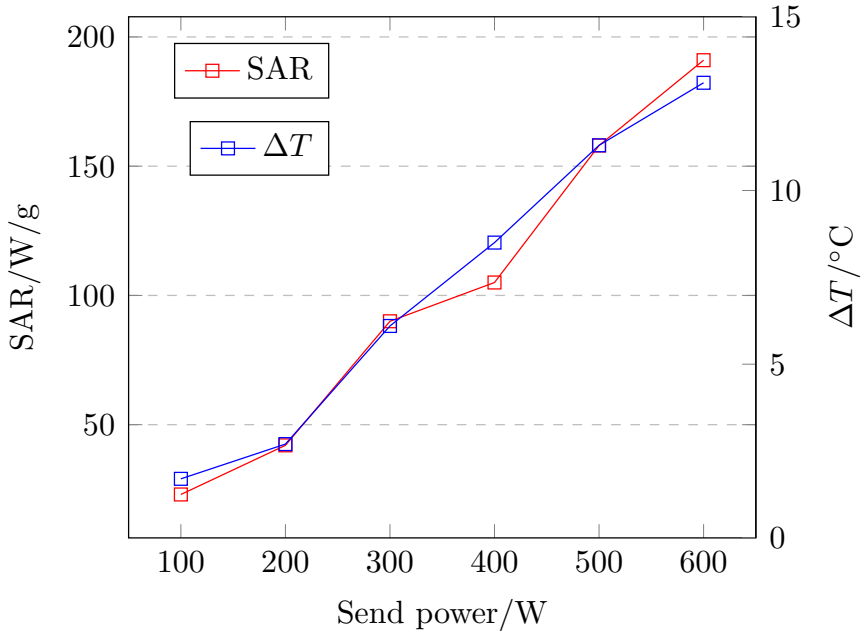

Figure 4.24: SAR of undiluted Synomag®-D 70 (iron concentration 10 mg/ml) and the temperature increase after 30s with different send power level.

The heating in the chosen time range is considered to be (quasi-) adiabatic when these values were within 5% of the net temperature increase slope. A MATLAB (The mathWorks, Inc, USA) script is written to find out the time range that satisfy the above conditions.

The SAR and the temperature increase after 30 s of the sample are shown in Figure 4.24. The SAR increases with the power, at 600 W, the SAR of Synomag-D 70 nm reaches 190 W/g, which is promising for MFH applications.

4.6 Summary and discussion

This section presents the design process, the manufacturing process and the evaluation of the hyperthermia insert capable of extending the preclinical scanner with the functionality of magnetic fluid hyperthermia. To protect the sensitive low noise electronics of the MPI scanner, the optimized coil topology introduced in chapter 3 with self-compensation effect is adopted and validated using a skeleton shape prototype. The small signal measurements with the prototype shows that most power can be compensated in all three channels. The manufacture process of

the hyperthermia insert is introduced in detail. The specific topology of the coil is difficult to achieve with conventional manufacturing and a high level of integration is mandatory to make good use of the finite space inside the MPI scanner. The adoption of both subtractive manufacturing and addictive manufacturing techniques allow manufacturing of customized parts with complex shape and mechanical strength. The massive use of clear material for construction permits the visibility of the inner structure of the cooling unit and helps to monitor the status of the coil.

The electric and magnetic characteristics, as well as the capability to heat particles of the hyperthermia insert have been evaluated. The insert has fulfilled the specified needs to generate up to 10 mT magnetic field at around 700 kHz which allows the magnetic fluid hyperthermia. The insert can work at full power continuously for 90 s and can work interleaved with 60 s /240 s heating/cooling cycle. The desired temperature increase of the brain tissue is 4 K to 6 K to successively open the blood brain barrier. The particle heating results have shown that the Synomag-D 70 nm particle sample can be heated up for 6 K by applying 300 W power for 30 s. The result shows that it is quite promising to achieve a $\Delta T = 6$ K, even with a smaller amount or lower concentration of the particles. Furthermore, the heating efficiency can be further improved by choosing the suitable MNP are specifically designed for MFH, contrary to the Resovist particles used in this study. A lot of researches have been made to synthesis the iron oxide nanoparticles feature large SAR value up to several hundreds W/g that are promising for magnetic hyperthermia applications [77, 78, 79].

However, further research needs to be done in the application scenarios that the MNPs are circulating in the vasculatures. When injected in to the animal or human, the particle solution is diluted by the blood, which can cause a dilution of around 1:1000–1:1500 [80]. Besides, the circulation time of the particles is limited. It has been shown that the particles are cleared quickly from the blood stream by liver and spleen, especially for larger particles and particle clusters, which contribute more to the heating effect [81]. One possible solution could be bolus admission via intraarterial injection using a catheter during cardiovascular interventions. The bolus can contain high concentrated MNPs and the catheter brings them directly to the main arteries in brain [29]. The effect of the blood perfusion on the heating efficiency has to be considered as well because of the significant heat removal by blood flow.

5

Integration of the hyperthermia insert into the MPI system

Contents

5.1 Introduction

In chapter 4, a hyperthermia insert is manufactured using rapid prototyping and 3D printing techniques, which is capable to generate a magnetic field suitable to perform MFH in the MPI scanner. The compatibility of the insert with the MPI system is tested, without discussing how to realize a MPI-MFH platform using both devices. In this chapter, a MFH system is implemented based on the hyperthermia insert and integrated into the commercial preclinical MPI scanner manufactured by Bruker BioSpin MRI, Ettlingen,Germany. To combine the two systems, the MPI scanner needs to be extended regarding the receive chain, cooling and control system. The specific plan of the hard installation and the inter-system communication as well as the risk analysis are made before the integration process. Finally, localized MFH using the MPI-MFH platform is validated by heating MNPs in phantoms.

5.1.1 Preclinical MPI scanner

The preclinical MPI scanner is intended for imaging the spatial distribution of MNPs in small animals (mice, rat, guinea pigs) and other solid or fluid samples with high temporal resolution and moderate spatial resolution. Some specifications of the scanner are listed in Table 5.1. The scanner features an FFP

Table 5.1: Specifications of the preclinical MPI system

Drive field	12 mT
Number of drive field channels	3
Drive field base frequency	25 kHz
Selection field	1.25/1.25/2.5 T/m
Focus field	15/15/36 mT
FOV	2 cm×2 cm×1 cm
Diameter of imaging bore	119 mm

traversing a Lissajous trajectory around the FOV with a period of 21.5 ms and the image reconstruction is based on acquiring the system function.

The system hardware consists of:

- Scanner frontend including MPI generator, calibration robot, and frontend electronics.
- Five electronic cabinets containing the control electronics and amplifiers.
- Two heat exchangers.
- Control workstation.

5.1.2 MFH system

The MFH system should equip the MPI scanner with MFH capabilities while maintaining its function of MNPs imaging. As discussed in chapter 2, the hardware setup for MFH is composed of a field generator, an impedance matching network and a power supply. Apart from that, extra filters are required to avoid the influence of the MFH frequencies on the MPI signal.

5.2 Components of the MFH system

The MFH system is composed of the hyperthermia insert with the impedance matching network, the radio-frequency (RF) power amplifier and the filters. The hyperthermia insert and the impedance matching network are discussed in chapter 4, this section will discuss the remaining components: the RF amplifier, the send filter, and the receive filter.

5.2.1 Signal chain of the MPI-MFH platform

The signal chain of the MPI-MFH platform is shown in Figure 5.1. The MFH system is for generating the MFH field therefore only has a send chain. The MFH signal is generated and amplified by the RF amplifier. Afterwards, the signal is band-pass-filtered and applied to the hyperthermia insert. Most power is compensated through the self-compensation effect of the coil topology. To protect the LNAs, the

signal that couples into the MPI receive chain is suppressed by a low-pass filter. After filtering the residue MFH signal enters the LNAs.

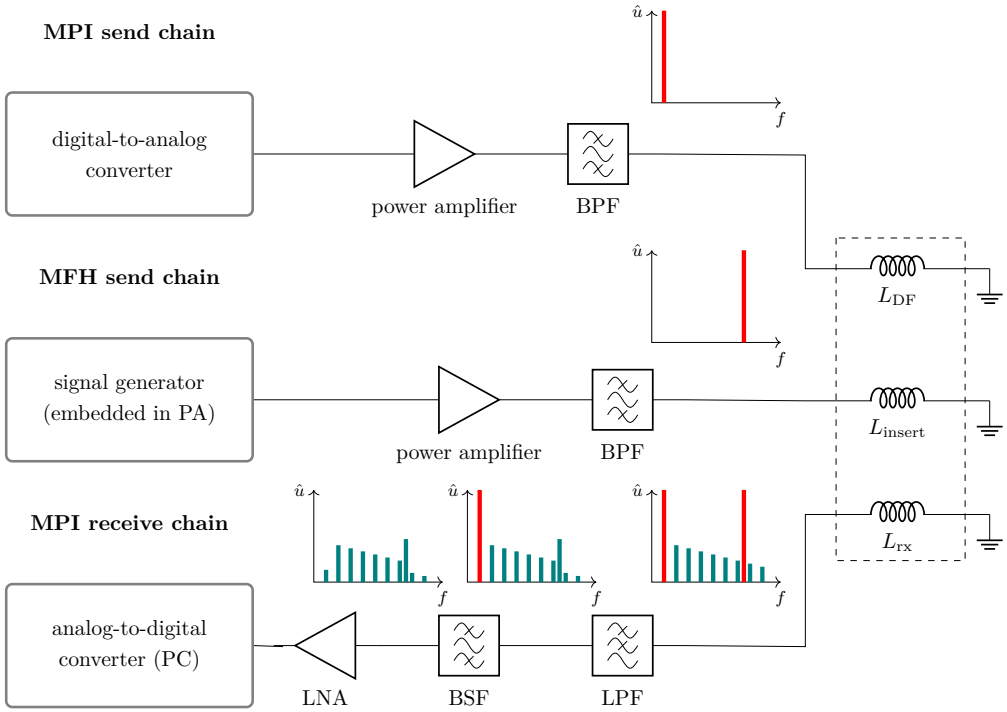

Figure 5.1: Signal chain of the integrated MPI-MFH platform.The impedance matching networks of the field generating coils are not shown. Red bars indicate the excitation signals directly couple into the receive chain which exceed the maximum input signal level of the LNAs. PA: power amplifier. L_{DF}: drive field coil. L_{insert}: hyperthermis insert coil. L_{rx}: MPI receive coil.

5.2.2 RF amplifier

A RF amplifier (AG 1012 Amplifier Generator, T&C Power Conversion, USA) generates and amplifies a high frequency signal (around 700 kHz) for the hyperthermia insert. The amplifier/generator provides up to 1000 W into a 50 Ω load and up to 800 W into any load in the frequency range 20 kHz to 6 MHz. The RF amplifier provides three important parameters related to the hyperthermia insert: the forward power, reverse power and the load power. As the name indicates, the forward power is the power output by the amplifier and the load power is the power transmitted into the load. The reverse power is the power

reflected to the amplifier because of load mismatch, which equals to the difference between the forward power and the load power. Due to the fact that a perfect 50 Ω load is not always achievable, some reflected power is common. In normal operation, the forward power is close to the set send power level of the amplifier, while the reverse power is a relatively small portion of the forward power. The opposite extreme, a faulty load (either open or short), results in significant reflected power typically near the level of the forward power. The forward power and reverse power of the RF amplifier have to be monitored continuously during operation.

5.2.3 Send filter

The RF amplifier does not only generate the signal for the MFH application but also noise. The noise enters the MPI receive chain together with the MFH signal and interferes with the MPI signal. Figure 5.2 shows the influence of the RF amplifier on the background MPI signal. The hyperthermia insert is placed in the scanner and powered by the RF amplifier. A MPI scan is conducted before and after the amplifier is enabled and the signal measured on three channels is compared. When the amplifier is off, the spectrum shows the background noise of the original MPI system. In the frequency range from 100 kHz to 1250 kHz, the noise level is below −100 dBm (10^{-10} mW). When the RF amplifier is on, the noise level in the frequency range from 200 kHz to 800 kHz increases due to the electronics of the amplifier even though no power is sent. At around 700 kHz, the resonant peak of the MFH system can be observed. To avoid influence on the particle signal, the noise level below 600 kHz should be kept under −100 dBm. Therefore, a send filter is implemented to remove the noise generated by the amplifier and pass the MFH signal.

Design

The send filter is designed as a bandpass filter. In principle, the filter structure can be realized as a Pi- or T-filter. In this work, a T-filter is used. The circuit design and the simulated transfer function of the send filter is shown in Figure 5.3. The resonant frequencies of each resonant branch are determined at first. Branches of L_{tx1} and L_{tx2} resonant at the same frequency of the MFH signal; the resonant frequency of branches L_{tx3} and L_{tx4} define the passband width and are set at ± 50 kHz of the

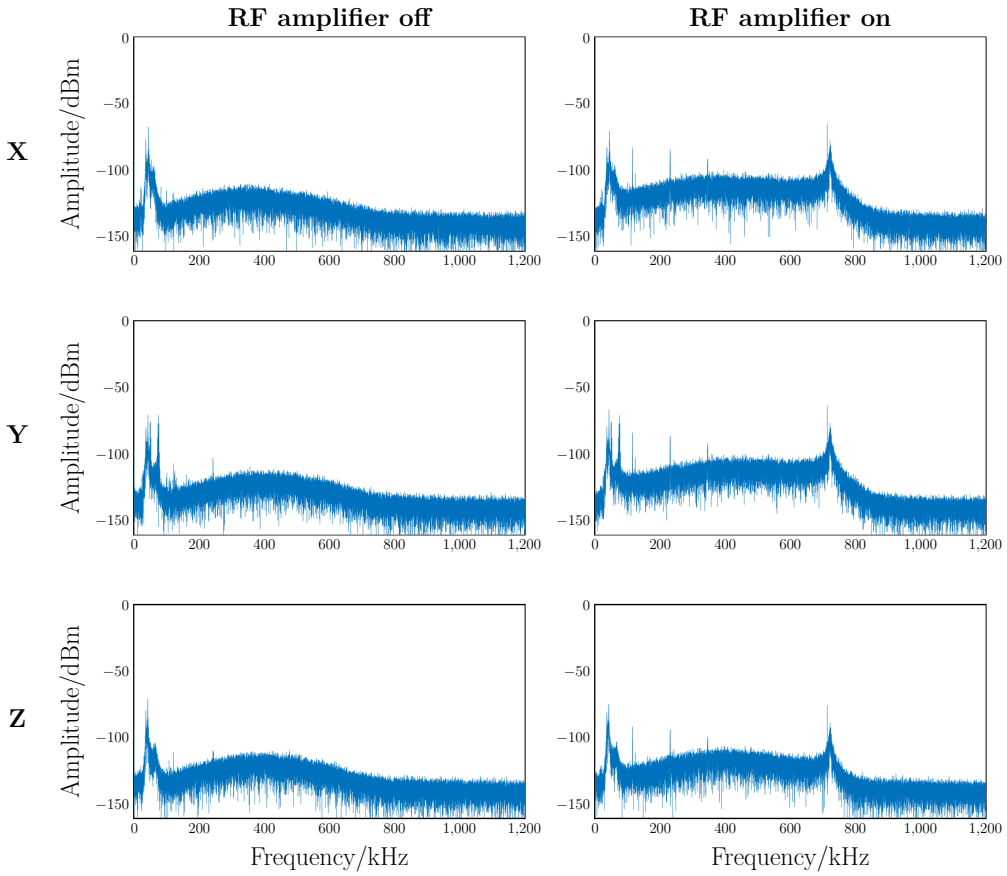

Figure 5.2: MPI background signal test with and without the RF amplifier. The peak at around 50 kHz is the resonant peak due to the MPI system and the peak at 700 kHz is due to the hyperthermia insert. The noise level increases in all 3 channels due to the RF amplifier.

center frequency. With the fixed resonant frequency f, the inductance L is inversely proportional to the capacitance C:

$$L = \frac{1}{(2\pi f)^2 C}.$$

At high frequencies, the impedance of the filter is determined by the inductors. To lower the current in the filter, inductors with larger inductance are preferred. Therefore the capacitors should be as small as possible. Taking the voltage and current rating into consideration, 5 nF Celem CP 80/200 capacitors (Celem Passive components, Israel) are used. Knowing the capacitance and the resonant frequency, the inductor values can be calculated.

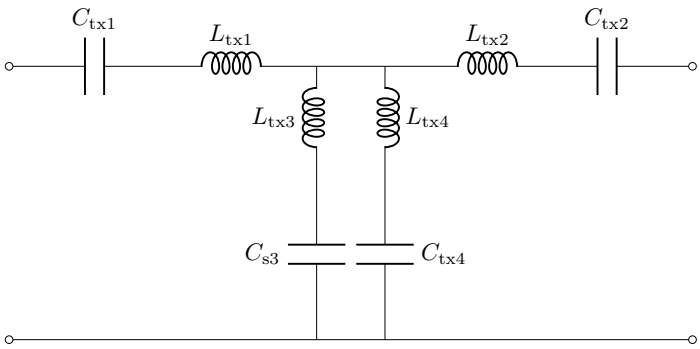

(a) Circuit design of the send filter based on resonant circuits with inductors and capacitors. The RF amplifier and the hyperthermia insert circuitry are not shown.

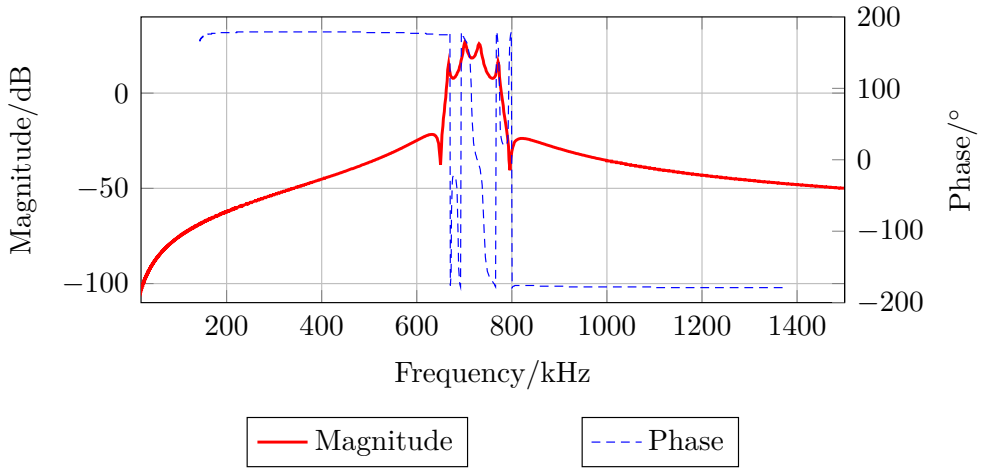

(b) Transfer function of the send filter simulated with the hyperthermia insert circuitry. The center frequency is 707 kHz and passband width is 100 kHz. The noises below 600 kHz are in the stopband and supressed by the filter.

Figure 5.3: Circuit design and transfer function of the send filter

Construction

10000 × 0.04 mm litz wire is used for winding the inductor. The litz wire is wound around toroid cores which are designed using CAD software and manufactured by 3D printing. The toroid cores are composed of two identical parts, the distance between those can be adjusted. In order to protect the filter from external influences and couplings of the filter components, the filter is installed in aluminium boxes with each stage isolated by copper plates. A 2 mm thick POM plate is placed between the

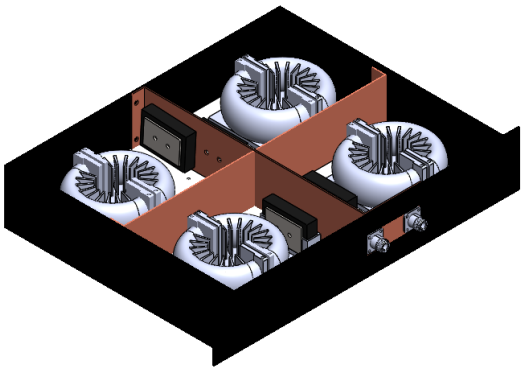

Figure 5.4: CAD model of the send filter. The grey parts are the toroid cores for the inductors. The stages are seperated with copper plates to prevent signal coupling.

components and the bottom of the boxes for better insulation. The filter has to be fine tuned to the resonant frequency of the hyperthermia insert by either adjusting the value of the capacitors or the inductors. The capacitance can be fine tuned by paralleling capacitors of small value. The inductance can be adjusted by changing the distance of the two half torii.The CAD model of the send filter is shown in Figure 5.4.

5.2.4 Receive filter

Despite the self compensation effect of the hyperthermia insert, signal will be coupled in the MPI receive chain. The maximum voltage on the impedance matching network can be calculated using:

$$P = \frac{U^2}{R}$$

with the full power 600 W and the impedance 50 Ω

$$U_{\max} = 489.8\,\mathrm{V_{pp}}.$$

The maximum input voltage of the LNAs is $50\,\mathrm{mV_{pp}}$, taking the 40 dB amplification ratio of the LNAs at 700 kHz into consideration, the attenuation of the MFH signal should be:

$$\mathrm{Gain} = 20\log_{10}\left(\frac{50\,\mathrm{mV_{pp}}}{489.8\,\mathrm{V_{pp}}}\right) + 40\,\mathrm{dB} = -39\,\mathrm{dB}.$$

According to the transfer function measurement shown in Figure 5.17b, due to the self compensation effect, the magnitude at the resonant frequency is already

−14.2 dB, −12.8 dB and −18.7 dB for x, y and z channel. The remaining −25.6 dB, −27.0 dB, −21.12 dB should be handled by filtering, therefore a receive filter is required.

Design

The filter should have no attenuation on the MPI signal below 600 kHz and around 30 dB damping of the 700 kHz MFH signal. A simplified circuit of the MPI receive chain shown in Figure 5.5a is used for simulation. The receive filter is connected in series to the MPI receive filter, which is a band stop filter with 25 kHz center frequency. From the electrical perspective, the receive filter can be placed either between the receive coil and the MPI receive filter or between the MPI receive filter and the LNA. However, that is difficult to realize in practice due to the space limitation for hardware installation. Therefore, the receive filter is placed in between of the two stages of the MPI receive filter as the red arrows indicate. Band stop filters or low pass filters can be used to remove the MFH signal. The receive filter needs to have a fast roll off from 0 dB at 600 kHz to −30 dB at 700 kHz. When using a band stop filter which has a similar design as the MPI receive filter but with a center frequency of 707 kHz, inductors of several hundreds µH and capacitors in the pF range are required. To have components that are easier to handle, a low pass filter with the design in Figure 5.5b is adopted. The parallel resonant circuits formed by L_{rx3}, C_{rx3} , L_{rx4}, and C_{rx4} have high impedance at the resonant frequency, which results in a notch in the stop band. By tuning the resonant frequency of L_{rx3}, C_{rx3} and L_{rx4}, C_{rx4} to 700 kHz, the MFH signal falls in the notch where has a higher attenuation than other frequencies in the stop band. The value of L_{rx3} and L_{rx4} should be as small as possible to have minimal attenuation of the MPI signal.

The transfer function of the MPI receive chain with and without the receive filter is simulated and shown in Figure 5.6. The high attenuation of the 25 kHz MPI excitation signal and at least 40 dB amplification of the higher harmonics of the original MPI receive chain should not be effected by the MFH receive filter. Compared to the original transfer function, the transfer function with the MFH receive filter remains unchanged until 40 kHz, which means the function of the MPI receive filter is maintained. The peak of the original MPI receive chain at 68 kHz is shifted to 53 kHz and peaks at 320 kHz, 560 kHz, 650 kHz are introduced by the receive filter. Table 5.2 compares the changes in amplitude at several

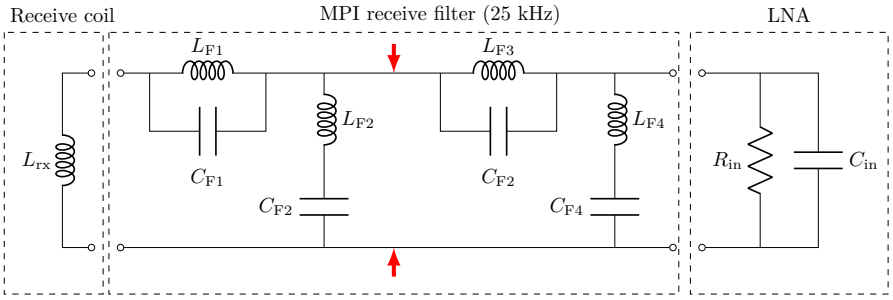

(a) Simplified circuit of the MPI receive chain. The signal in the receive coil is filtered by the MPI receive filter to remove the 25 kHz component before entering the LNA. Red arrows indicate the position of the receive filter. R_{in}, C_{in}: equivalent input resistance and capacitance of the LNA.

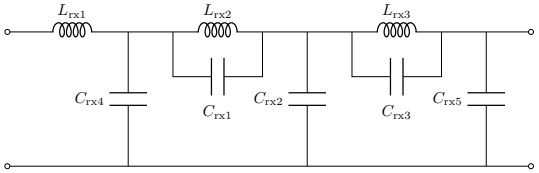

(b) Circuit design of the receive filter to suppress the MFH signal at 707 kHz. Low pass filter is used to achieve higher attenuation and reduce the amount of component.

Figure 5.5: Circuit design of the MPI receive chain and the receive filter.

frequencies. The amplification of the higher harmonics are higher than 36.6 dB until 600 kHz, the damping of the 700 kHz MFH signal is -57.8 dB.

Construction

The inductors are wound using 0.02 mm × 2000 Litz wire on ferrite cores. As discussed in chapter 2, the ferrite core introduces distortion into the MPI signal. However, the inductor L_{rx2} and L_{rx3} are only 3.5 µH and litz wire is chosen, the quality factor is low when winding on air core. To increase the quality factor, ferrite toroidal cores 80 TOROID (Fair-Rite Products Corp., New York) are used for the inductors. The core material features low permeability $\mu = 550$ thus generates only small distortion on the MPI signal. The inductance factor A_L is 350 µH±25%, the

Table 5.2: Comparison of the gain and loss value of the MPI receive chain with and without the receive filter at different frequencies. The MFH signal is suppressed without significant attenuation of the MPI signals.

Frequency/kHz	Gain/Loss w/o receive filter/dB	Gain/Loss with receive filter/dB	Difference/dB
25	-92.8	-92.8	0
75	52.3	40.9	-12.9
125	45.2	36.6	-8.6
175	42.5	37.5	-5.0
225	41.6	40.2	-1.4
275	41.3	45.6	4.3
325	41.0	51.9	10.9
375	40.9	43.5	2.4
425	40.8	39.1	-1.7
475	40.8	37.5	-3.3
525	40.7	38.9	-1.8
575	40.7	51.1	10.4
700	40.7	-57.8	-98.5

number of turns N can be calculated by:

$$N = \sqrt{\frac{L}{A_{\mathrm{L}}}}.$$

With A_{L}=350 nH, around 3 turns are needed for $\mathrm{L_{rx2}}$ and $\mathrm{L_{rx3}}$, 6 turns are needed for L_{rx1}. The Litz wire is fixed on the ferrite core using 3D printed parts. $\mathrm{C_{rx1}}$ to $\mathrm{C_{rx5}}$are made by parallelizing KEMET capacitors (KEMET Corporation, USA) of different values.

5.3 Inter-system communication and risk analysis

To protect and ensure proper working of both MPI and MFH systems, basic inter-system communication needs to be established. The MPI system should have full control of the MFH system and to be able to monitor its status such that measures can be taken when a fault condition is detected. In this section, the remote control

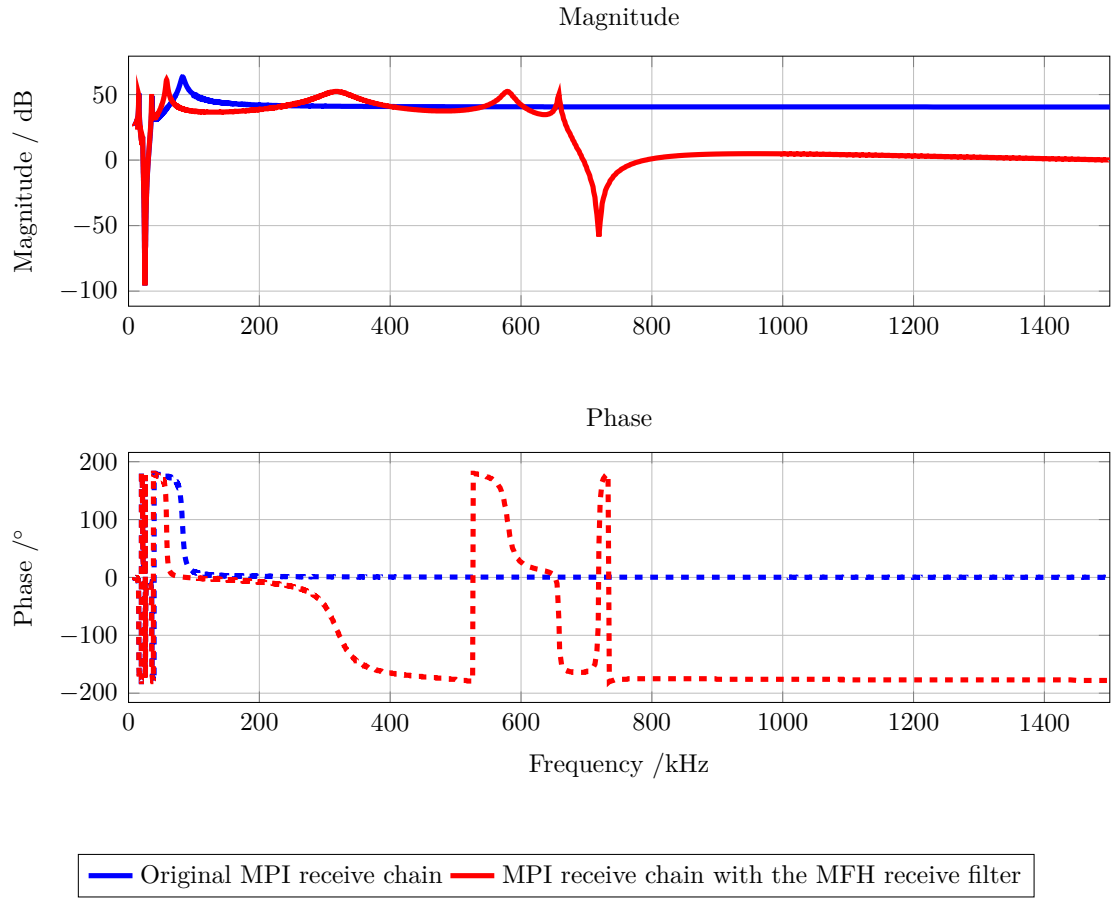

Figure 5.6: Transfer function of the MPI receive chain with and without the MFH receive filter. The magnitude and phase are change by incuding the MFH receive filter, nevetheless the MPI signal below 600 kHz is not significantly attenuated.

of the RF amplifier by the MPI system and the monitoring through a temperature sensor and a flow sensor are discussed. Furthermore, we perform the safety analysis to consider all problems the integrated system can encounter and propose possible solutions.

5.3.1 RF amplifier control

The RF amplifier is controlled by the MPI scanner for the following aspects:

- MPI system controls power supply of the RF amplifier.
- MPI system controls the power level of the RF amplifier.
- MPI system catches signal if the RF amplifier reverse power limit is reached.

The RF amplifier provides the remote control and monitoring functions by analog signal via the DB 25 connector on the rear panel, which includes: remote power level adjustment and control, remote access to forward and reverse power level information, and status flags indicating power on, thermal limit, reverse power limit. Table 5.3 lists the functions used in this work.

To enable remote operation, the remote control signal must be asserted (+5 V), which is provided by the user power of the RF amplifier. The amplifier's power level is controlled with a DC voltage proportional to the desired RF power level. A TTL high level on the blanking port will interrupt the RF output; the normal open condition allows normal operation. The amplifier output is blanked during the cooling cycle when the hyperthermia insert works in interleaved mode. The forward and reverse power can be detected by measuring the DC voltage at the regarding ports. The power supply of the amplifier is provided and controlled by the power unit of the MPI scanner.

5.3.2 Temperature monitoring

The MPI system should receive temperature information of the MFH system so that overheating of the hyperthermia insert triggers a shutdown of both systems. The temperature information of the hyperthermia insert can be obtained by the temperature sensor PT100 introduced in Figure 4. The resistance of the PT100 is measured for the temperature readout. Figure 5.7 shows the measurement circuit of the PT100. Four-wire connection is used to remove the effect of the lead wire resistances from the sensor measurement. The 4-wire circuit works by using wires 1 & 4 to power the circuit and wires 2 & 3 to read. The input impedance of the voltage measurement circuitry is very high to prevent significant current flow in

Table 5.3: Signal used for the remote control of the RF power amplifier. The power output and the send power level can be controlled using the MPI control unit. The power sent to the hyperthermia insert and the power reflected to the RF amplifier can be monitored. However, the signal input ports of the MPI control unit is not implemented in the frame of this work.

Signal	Signal type	Description	Signal direction	Signal generator/receiver
Remote enable	TTL	Hi=remote control active Lo=remote control disabled	IN	User power (RF amplifier)
RF power set	0-5 VDC	linear voltage scale: 1V/200W	IN	MPI control unit
Blanking signal	TTL	Hi=interrupts RF output Lo=uninterrupted operation	IN	MPI control unit
Forward power	0-5 VDC	linear voltage scale: 1V/200W	OUT	not defined in this work
Reverse power	0-5 VDC	linear voltage scale: 1V/200W	OUT	not defined in this work
RF power on	TTL	Hi=RF power on Lo=RF power off	OUT	not defined in this work

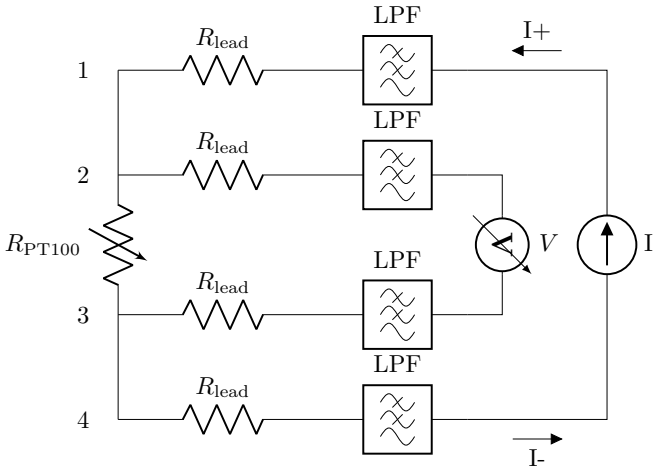

Figure 5.7: The measurement circuit of the temperature sensor PT100. The influence of the lead wire resistance is removed by using 4-wire-connection. Four same low pass filers are used to remove the high frequency signal induced in the circuit.

the voltage leads 2 & 3. The voltage drop across the resistance is measured by the voltmeter, and resistance calculated using Ohm's law:

$$R = \frac{U}{I}. \tag{5.1}$$

Since no current is flowing, the voltage drop measured is not effected by the test leads and connection wires. Thus, the errors caused by their resistances are eliminated.

The PT100 cannot connect directly to the readout circuit because the field generated by the insert and the MPI drive coil induce signals in the leads, which disturb the voltage and current measurement. Low pass filters are implemented to remove any signals higher than 10 kHz. The temperature data measured by the PT100 is collected by the control unit of the MPI system. When the measured temperature exceeds 50 °C, the scanner is set to standby mode and no power will be send to the insert.

5.3.3 Flow sensor

The hyperthermia insert and the impedance matching network are cooled with oil using the MPI cooling system. Sufficient oil flow is crucial for proper cooling and

avoiding overheat of the MFH system. A flow sensor is used to monitor the oil flow and sends information to the MPI control unit. A reduction of the cooling flow rate can be caused by broken or loosen parts of the insert in the oil or external forces on the cooling hoses which increase the flow resistance. Therefore, before sending power to the MFH system, the flow rate should be checked to ensure the proper cooling. During the heating process, the flow rate has to be continuously monitored. If flow decreasing is detected, the power supply of both systems has to be shut down.

5.3.4 Risk analysis

To reduce the risks of operating the integrated system, the potential uncertainties need to be analyzed. We perform a simple risk management process where the possible risk sources are identified and solutions are proposed to minimize the occurrence or impact of these risks.

- Fail of the MFH system power supply
  Fail or emergency shut down of the RF amplifier or the power supply unit of the MPI scanner can cause the breakdown of the hyperthermia insert power supply, which results in a sudden voltage drop at the hyperthermia insert. This should not be harmful since the power should decay due to the resonant circuit.

- Mismatching of impedance
  The impedance can generally become mismatched. This can be detected by sending small power (e.g. 10 W) to the insert and observe the reverse power of the RF amplifier. Impedance can be matched by adjusting the frequency or retune the impedance matching circuit.

- Sudden electrical or mechanical disconnection
  Electrical and mechanical connections can loosen and lead to sparking, spilling of coolant or other unexpected results. The connections should be checked before sending power to the MFH system.

- Sparking
  Considering the high voltages in the system, sparking can occur for unknown reasons in the insert.

- Wrong setting of the frequency
  The signal frequency of the RF amplifier can be set to wrong values. Choosing the wrong frequency leads to mismatch of the amplifier load, which may result in high reflected power. This should do lead no harm to the amplifier since it decreases the send power automatically when the reverse power limit is reached. The MPI system might be damaged due to the insufficient damping of the signal.

- Wrong setting of the send power
  Setting the send power of the RF amplifier higher than 600 W can destroy the electronics of the MPI receive chain and cause overheat of the insert. This can be prevented by setting the maximum forward power to 600 W on the RF amplifier.

- Positioning of the hyperthermia insert
  The hyperthermia insert can be placed at wrong positions in the scanner bore. The geometric center of the insert can be found by measuring its field profile. The center of the MPI scanner can be found by imaging a delta probe. The insert position should be adjusted to make the center position coincident.

- Movement of the hyperthermia insert
  The insert can move inside the scanner bore, destroying the compensation. A coil fixation pin is used to prevent the movement of the insert.

- Change of coil geometry
  The coil geometry can change, e.g. shift of wire or fail of wire fixation structures. This will lead to loss of compensation. The coil geometry can be checked by visual inspection of the hyperthermia insert.

- Material removal in the insert
  Material ablation can loosen material which gets carried away by the coolant and is a risk for components connected to the cooling circuit. Filters can be installed in the cooling system.

- False robot movement
  A faulty robot movement destroys or damages the insert. A guard-ring can be installed in the MPI scanner which has a smaller diameter than the insert bore. The robot stops when it touches the guard ring. Alternatively, the movement range of the robot can be defined by setting the MPI control system

so that it only moves in a cylinder which will confine the robot to move in a cylinder-shape space.

- Metal in the insert
  Metal in the insert heats up when the MFH field is on and even during imaging, the heat might destroy the insert. No metal parts should be placed in the insert bore.

- Destruction of insert material
  Pressure in the system can destroy the insert components and coolant might be spilled. Other risk sources could be the samples or chemicals in the insert bore which might interact with the material of the insert.

- Leakage of oil
  Oil can be spilled due to leakage in the cooling unit or oil hose.

- Clamping of the oil hose
  Clamping of the oil hose results in insufficient oil flow. This can be detected by the flow sensor.

- Condensation on cooling and power-hose
  If the temperature and humidity are above a certain level condensation might occur. This can be prevented by an air-conditioned scanner room and setting the chiller temperature to 16 °C.

- Fail of cooling
  The cooling fails. This would lead to overheating of the insert, increase of resistance and therefore detuning of the impedance matching circuit. This can be detected in means of reflected power by the RF amplifier or the PT100 temperature sensor and the decreased oil flow.

5.4 Hardware installation

The MPI scanner components are installed in two rooms: the scanner frontend is located in a low-frequency shielded scanner room, five cabinets including the system electronics and the cooling units are located in a technical room adjacent to the scanner room. Space has to be allocated for the MFH components including

the RF amplifier, send filter, receive filter and the hyperthermia insert with the impedance matching network (Figure 5.8). This section introduces the installation process of each component.

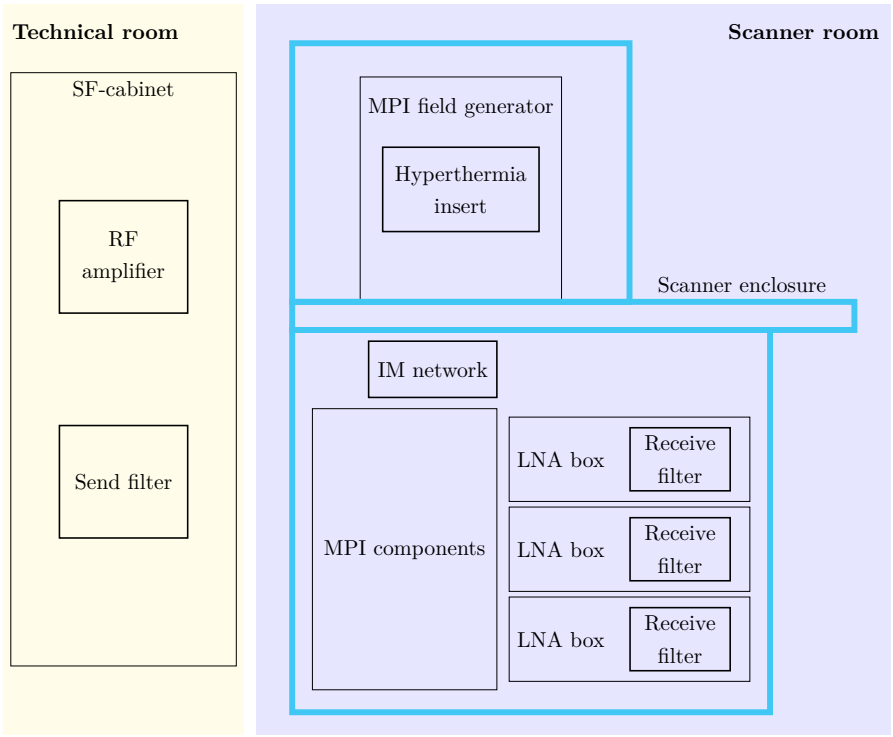

Figure 5.8: The physical location of the MFH components need to be installed into the MPI system. The hyperthermia insert is installed in the scanner bore. The impedance matching network and the the receive filters are installed in the scanner enclosure with other MPI components. The RF amplifier and the send filter are installed in the selection field cabinet.

5.4.1 Cabling plan

Cables are needed for signal transmission and power supply. The cables are installed as shown in Figure 5.9. KH_1 to KH_4 are the cables for the power supply of the MFH system. KH_8 to KH_{10} are the cables for the remote control of the RF amplifier. KH_{GND} is the ground cable of the impedance matching network. KT_1 to KT_3 are the cables for the PT100 temperature sensor readout. KK_1 and KK_4 are tubes for the cooling of the MFH system. The length and connectors of the cables are predefined for the proper installation. Feed-through on the filter plates and shielding

of the cables are installed as well.

5.4.2 Installation of the power amplifier

The RF power amplifier is installed in the selection field cabinet in the technical room. The MPI's power supply system provides the 200-240 VAC / 50-60Hz / 10A power supply required by the amplifier. Safety circuit breaker is installed. The amplifier chassis is connected to the cabinet ground. Proper ventilation is provided by the MPI system to ensure the operation of the amplifier. Figure 5.10 shows the RF amplifier installed in the SF cabinet. The analog remote control interface is installed on the front panel. A toggle switch is implemented for enabling and disabling the remote control of the RF power amplifier. The 5 BNC connectors are the send power leveling, forward power meter, reverse power meter, power output indicator and blanking port, respectively.

5.4.3 Installation of the cooling

The MFH cooling system is installed as shown in Figure 5.11. The cooling is connected in parallel with the cooling of the MPI drive coils. The oil flows in from the oil inlet of the impedance matching network and flows out to the oil outlet of the hyperthermia insert. The flow sensor is calibrated based on the maximum and minimum flow rate of the MFH system. The chiller is set to 16 °C and the pressure is set to 0.8 bar.

5.4.4 Installation of the hyperthermia insert

The hyperthermia insert is installed in the MPI scanner bore with an insert fixation part. As shown in Figure 5.12, the insert fixation part is connected to the hyperthermia insert and can be fixed by the fixation pin in the scanner bore provided by the MPI scanner. The fixation part ensures the center of the heating coil align with the 0 position of the MPI scanner and prevents rotation of the insert. The inner diameter of the insert fixation part is 3 mm smaller than the hyperthermia insert. When the robot is driven to the wrong position, it first

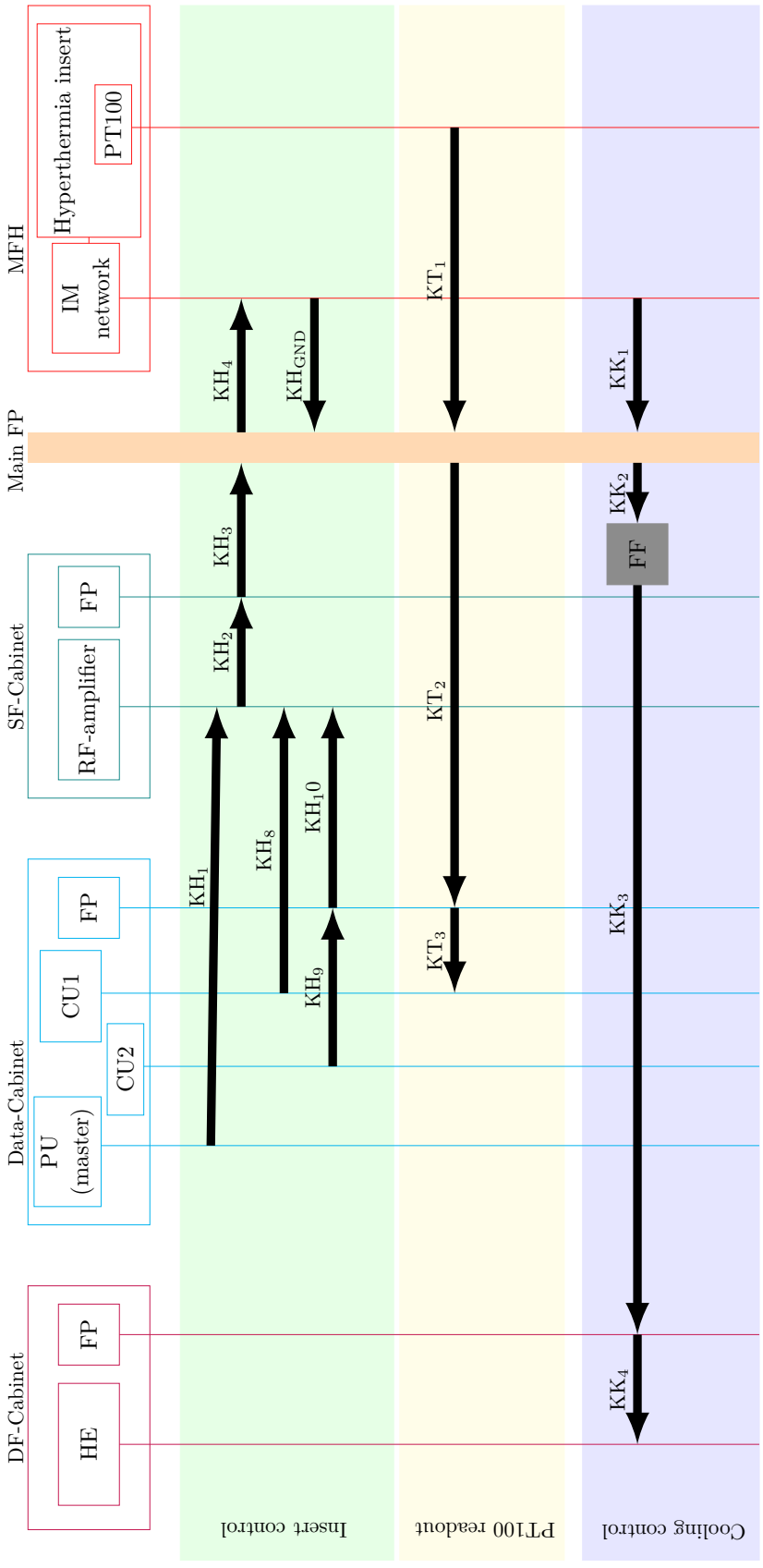

Figure 5.9: Cable and tubing plan of the MFH system. KH: cables for the insert control. KT: cables for the PT100 temperature readout. KK: cables for the cooling of the MFH system. HE: heat exchanger. PU: MPI power unit which provides the power supply of both the MPI system and the MFH system. CU1: MPI control unit which generates signal to enable the power output and set send power level of the RF amplifier. CU2: MPI contol unit which generates the blanking signal to the RF amplifier FP: filter plates where the filters and cabel feedtrough locate. FF: filter and flow sensor of the cooling.

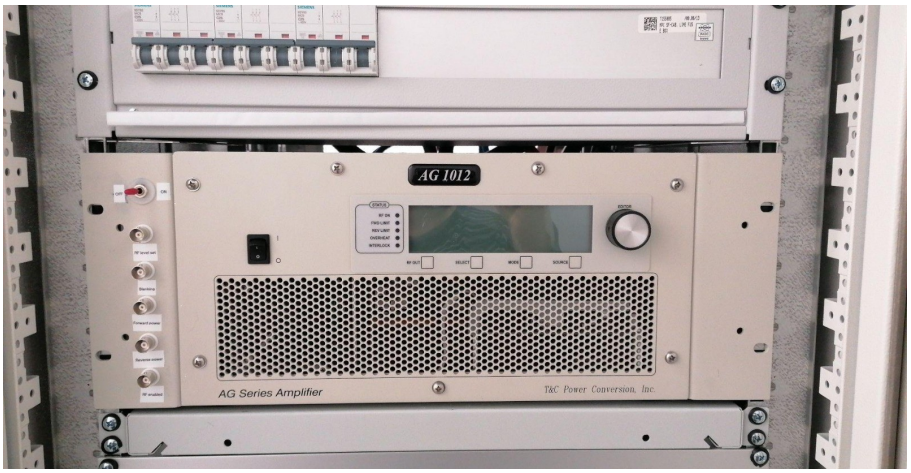

Figure 5.10: The RF amplifier installed on the rack of the selection field cabinet. A analog signal interface is implemented on the left side of the front panel for the remote contol.

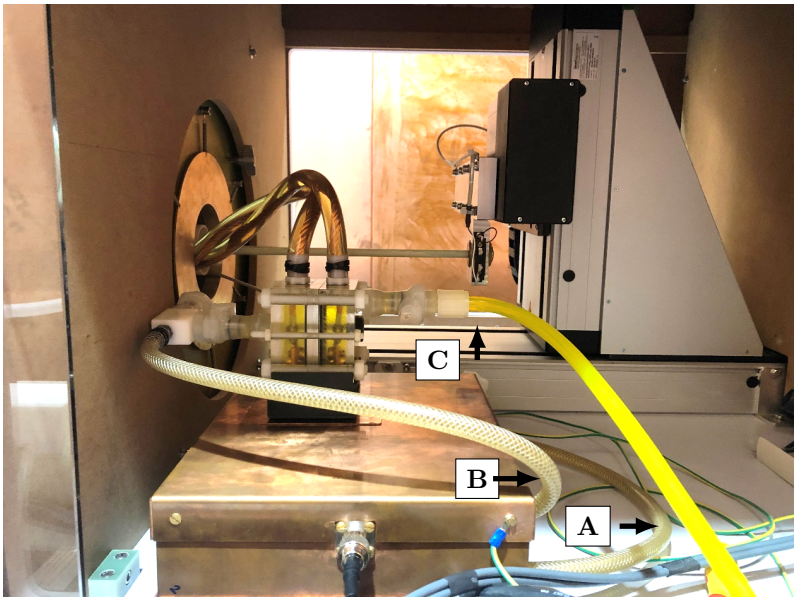

Figure 5.11: The cooling connection. The impedance matching network is placed beside the robot. The oil flows into the MFH system (A) and cools the capacitor bank of the impedance matching network. Afterwards, the oil flows from the impedance matching network to the hyperthermia insert (B) and flows out (C).

collides with the fixation part and stops, avoiding damage of the insert by robot collision.

Figure 5.13 shows the hyperthermia insert installed in the scanner observed from

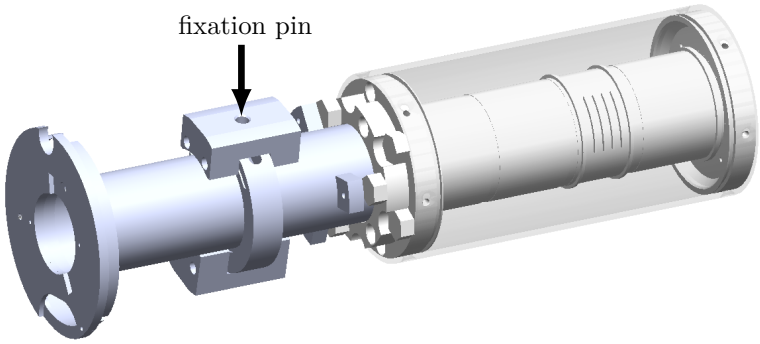

Figure 5.12: The insert fixation part (left) attached on the cover plate of the hyperthermia insert (right). The fixation pin locks the hypethermis insert through the hole on the fixation part.

the scanner front side and the robot side. When placed in the scanner, the insert can not be observed by visual inspection. Therefore, the oil has to be filled in before the insert is installed in the scanner bore to ensure the elimination of air bubbles.

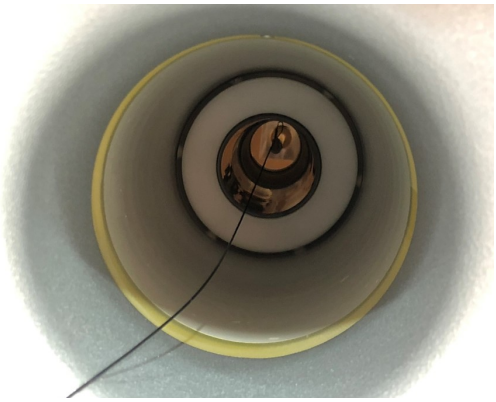

(a) Front side view.

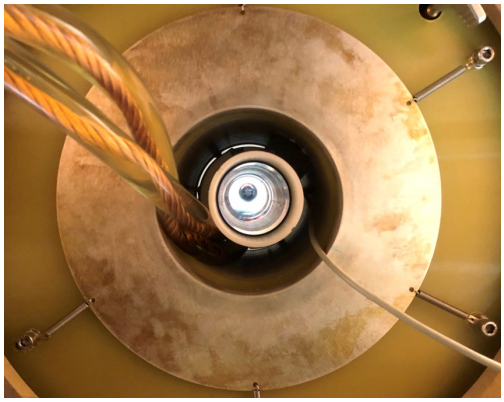

(b) Robot side view.

Figure 5.13: The hyperthermia insert placed in the scanner bore. The bottom plate of the hyperthermia insert and the insert fixation part can be seen from the front side view and the robot side view, respectively. The connection wires go out from the scanner bore from the robot side and connects to the impedance matching network.

5.5 Evaluation of the integrated system

In this section, the function of the installed components including the RF amplifier, the filters and the hyperthermia insert is evaluated. Both small signal and high power tests are conducted to validate the suppression effect of the MFH signal in the MPI receive chain using passive compensation and filtering.

5.5.1 RF amplifier remote control

The analog remote control of the amplifier send power is tested using a DC signal generator and an oscilloscope with a 50 Ω dummy load. The RF output is connected to the dummy load and the remote control is enabled. The DC signal generator is connected to the BNC send power leveling port of the remote control interface and generates analog signal with different voltage. The power supply of the amplifier can be controlled by switching the MPI power supply unit on and off via the MPI user interface. The forward power and reverse power measured by the amplifier are observed. The voltage on the dummy load is measured using the oscilloscope and used to calculate the power on the dummy load. Table 5.4 shows the comparison of the send power displayed on the amplifier and the power on the dummy load with different analog input signals. The input voltage is tested up to 3 V because the maximum power load of the dummy is 300 W. The blanking function is tested by sending 5 VDC to the blanking port. The amplifier displays interlocked on the front panel and the send power remains 0 W regardless of the analog input signal level at the send power leveling port.

Further tests are conducted to realize the interleaved heating by controlling the power amplifier using MPI software. The send power frequency is pre-set on the amplifier. The MPI control unit generates the signal to enable and disable the output of the amplifier according to the time of heating cycle, cooling cycle and the send power level defined in the program. Figure 5.14 shows the display of the RF power amplifier during the interleaved heating test. In the heating cycle the send power is 601 W, in the cooling cycle the send power is 0 W.

Table 5.4: Expected and measured power on the dummy load using remote control. SP: send power. LP: load power RP: reverse power.

Analog input/V	Expected SP/W	Display on amplifier			Power on the dummy load/W
		SP/W	LP/W	RP/W	
0	2	2	3	0	3.91
0.1	10	10	10	0	15.63
1.0	100	100	100	0	105.95
1.4	140	140	140	0	133.23
2.0	200	200	200	0	189.66
3.0	300	300	300	0	291.60

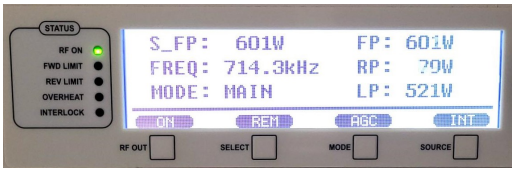

(a) RF power amplifier display in the heating cycle.

(b) RF power amplifier display in the cooling cycle.

Figure 5.14: RF power amplifier display during the interleaved heating test. The green light indicates that the power output is on. The red light indicates that the power output is blanked.

5.5.2 MFH magnetic field property

The magnetic field property is evaluated using a 3D pick up coil. The pick up coil has three channels, which receive the signal induced by the alternating magnetic field in the x, y and z direction. The pick-up coil can be moved to different positions by the scanner robot. The transfer function of the system is measured with the setup shown in Figure 5.15a. The amplitude of the MFH field is proportional to the magnitude of the measured transfer function at the MFH frequency. The MFH field profile can be evaluated by measuring the S21 curve of the x-channel at different positions. The pick up coil is moved along the x, y and z axes with a step size of 5 mm. The measurement range of the x-direction is -25 mm to 25 mm, while it is -20 mm to 20 mm in y and z direction due to the restriction of the insert bore size. The result is plotted in Figure 5.15b. Compared to Figure 4.5, the hyperthermia insert has a similar field profile when installed in the MPI scanner.

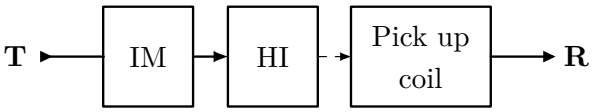

(a) Measurement schematic of the field property, where the solid arrow denotes the cable connection and the dashed arrow denotes the coil coupling. HI: hyperthermia insert. IM: impedance matching.

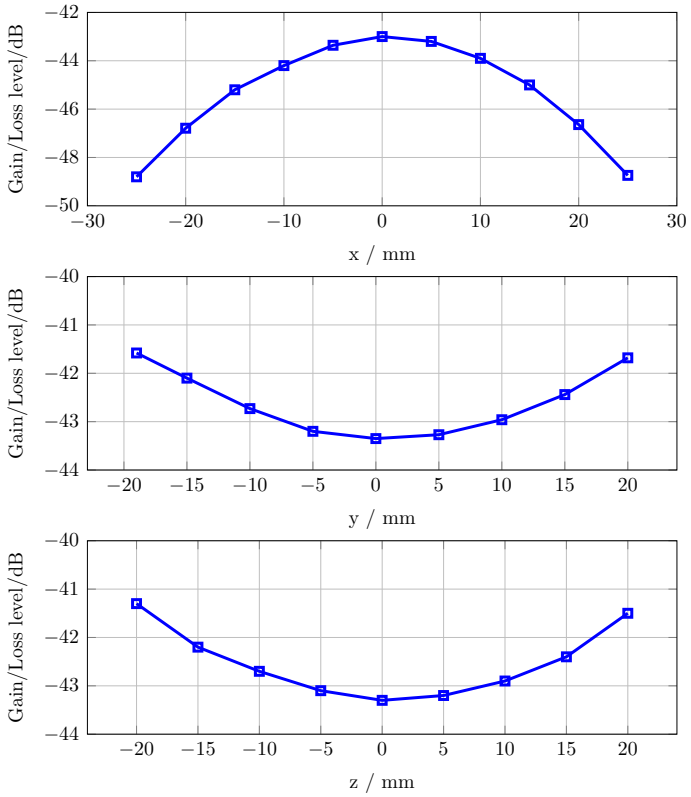

(b) Field profile of the MFH field genrated by the hyperthermia insert installed in the MPI scanner, similar shape as the result measured without the MPI scanner can be observed. On y direction, the field is measured until -19 mm due to the restriction of the coil fixation part.

Figure 5.15: Field profile measurement setup and result of the hyperthermia insert installed in the MPI scanner.

5.5.3 Impedance and resonant frequency

The resonant frequency and the impedance of the hyperthermia insert, when installed in the scanner, are measured. The resonant frequency defines the send power frequency that has to be set on the amplifier. The impedance magnitude

and phase at the resonant frequency should be around 50 Ω and 0° to avoid load mismatch. The result is shown in Figure 5.16. The matched frequency is 706.7 kHz and the impedance magnitude and the phase at the resonant frequency is 43.38 Ω and 4.2°. The resonant frequency shifts towards high frequency compared to the value in Table 4.5 due the interference of the components in the MPI scanner (i.e. eddy current).

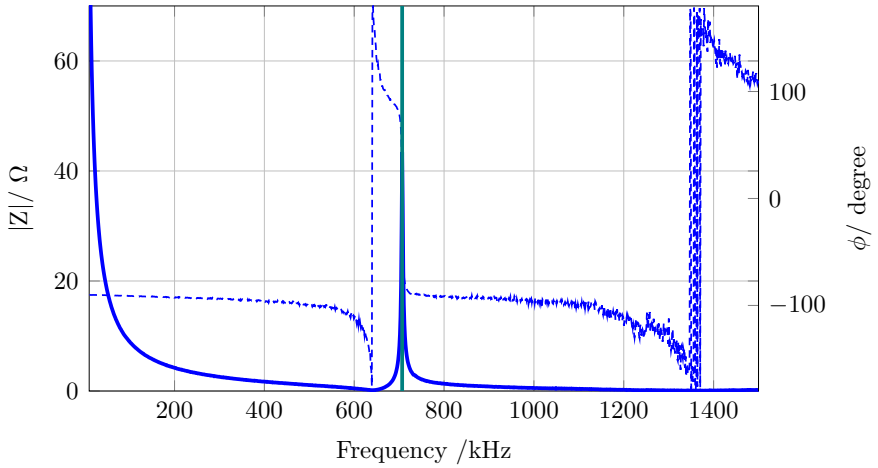

Figure 5.16: Impedance of the matched hyperthermia insert.The resonant frequency is marked with the green line. Solid line: amplitude. Dashed line: phase.

5.5.4 Decoupling effect

The decoupling effect of the hyperthermia insert is evaluated before the installing of the send filter and the receive filter. The transfer function from the impedance matching network to the LNA output is measured with the set up shown in Figure 5.17a. Figure 5.17b shows the measured transfer functions of three channels. At the resonant frequency, the magnitudes are −14.2 dB, −12.8 dB and −18.7 dB for the x, y and z channel. Due to the amplification effect of the resonant circuit, the power level at the matched frequency increases compared to the unmatched results in Chapter 4.

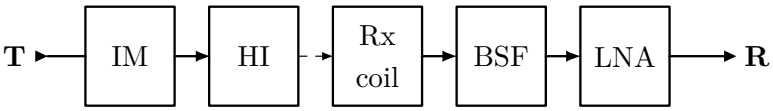

(a) Measurement schematic of the decoupling effect with impedance matching network.

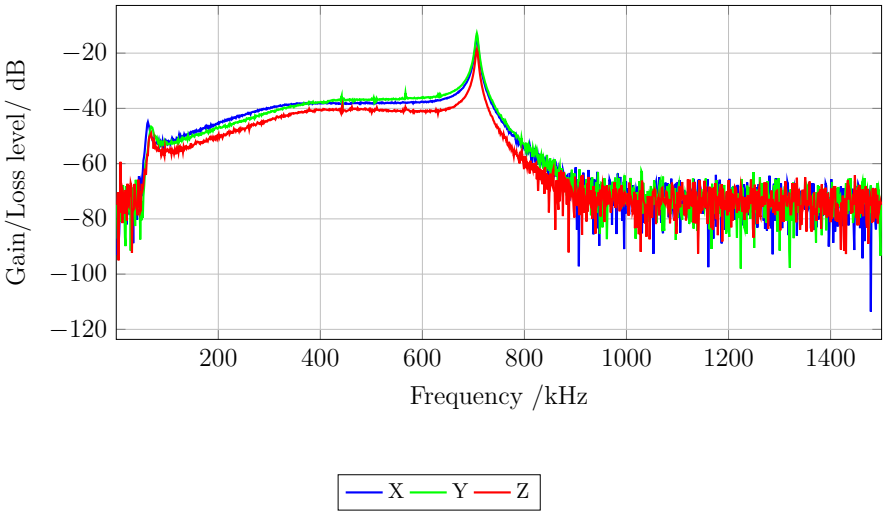

(b) Transfer function from the impedance matching to the LNA output. A resonant peak can be observed at the matched frequency 706.7 kHz of the hyperhtermia insert.

Figure 5.17: Decoupling effect measurement setup and result of the integrated hyperthermia insert.

5.5.5 Send filter

The send filter is connected between the RF power amplifier and the impedance matching network. The filter should suppress the noise generated by the amplifier in the frequency range below 600 kHz. Besides, it should have no effect on the matched impedance of the hyperthermia insert since the RF amplifier requires 50 Ω load for the maximum power transmission. Figure 5.18 shows influence of the send filter on the matched impedance. According to the simulation result, despite of the two resonant peaks introduced by the send filter at around 673 kHz and 767 kHz, the impedance at the MFH frequency remains unchanged at 43 Ω. However, the measured impedance at the MFH frequency decreases to 21 Ω, which is only half of the designed value. With 21 Ω, high reverse power can be expected when sending high power of 600 W. The reason of the change of impedance is the influence of

the MPI scanner on the electrical property of the hyperthermia insert coil. The components of the MPI scanner, e.g. drive field coils, focus field coils and shielding, which interact with the hyperthermia insert coil and change its inductance and impedance. Further work on the send filter design is required for high power test.

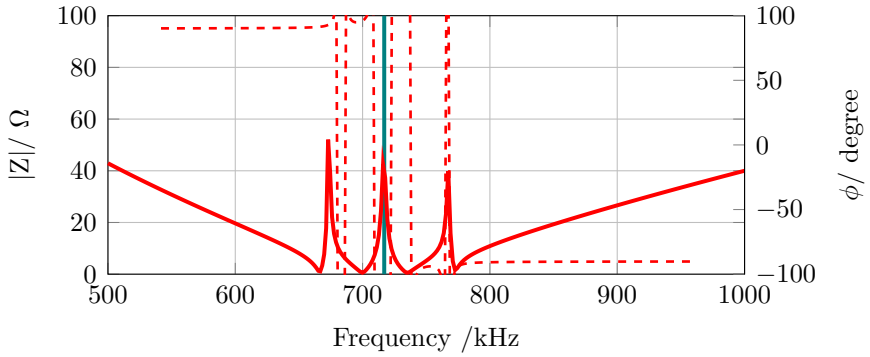

(a) Designed value of of matched impedance influnced by the hyperthermia insert. Without the MPI scanner, the impeance is around 50 Ω at the MFH frequency.

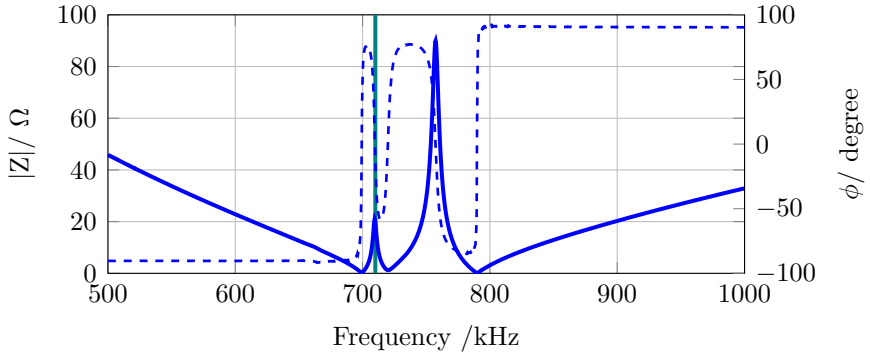

(b) Matched impedance of the hyperthermia insert with the send filter when installed in the MPI scanner. Both the matched frequency and impedance change.

Figure 5.18: Matched impedance of the hyperthermia insert with the send filter, namely the load impedance of the RF power amplifier. The MFH frequency is marked with green line.

Figure 5.19 shows the spectra of signal measured by the MPI scanner with and without the send filter. Due to the load mismatch, the frequency shifts to 709.6 kHz. The function of the send filter is tested with low power level (10 W) where no reverse power is observed. With the send filter, the noises below 600 kHz are attenuated and the power level is lower than −100 dBm. However, the power of the residual

MFH signal in three channels reduces from −48.0 dBm, −51.8 dBm and −49.9 dBm to −48.5 dBm, −52.2 dBm and −50.3 dBm. Since the send frequency is the same, the damping of the MFH signal due to the receive chain is the same. Therefore, the MFH signal is slightly attenuated by the send filter. The high power test with the send filter is not completed in the frame of this work.

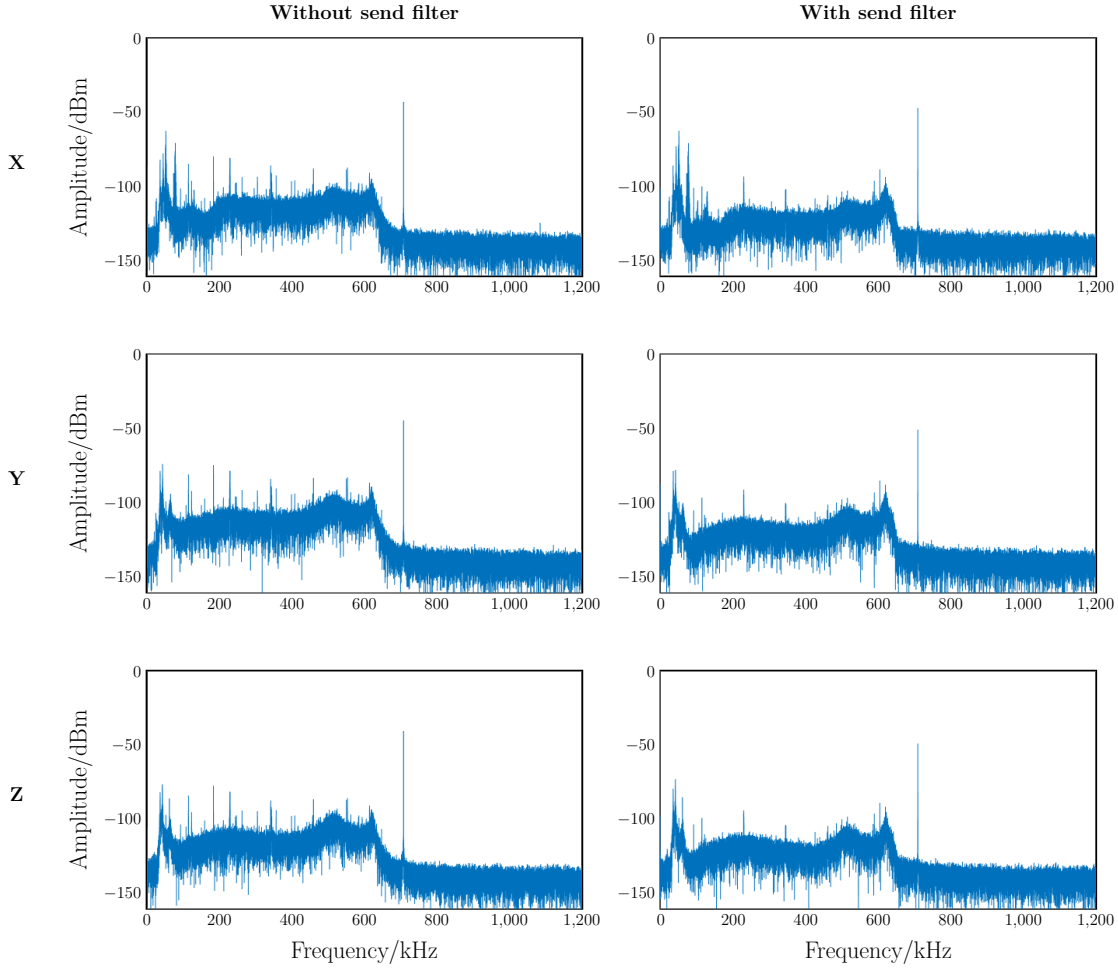

Figure 5.19: Signal spectra of three channels with and without the send filter. 10 W is sent to the hyperthermia insert. The send filter supresses the noises in all three channels. The MFH frequency is shifted from 706.7 kHz to 709.6 kHz.

5.5.6 Receive filter

The transfer function of the MPI receive chain is measured before and after the installation of the MFH receive filter. The receive filter is installed between the two

stages of the MPI receive filter, the measurement setup is shown in Figure 5.20a. and the results are compared in Figure 5.20b. At the MFH frequency, an attenuation of 50 dB can be achieved with the receive filter. To avoid influence on imaging, the filter should have no attenuation on the MPI signal below 600 kHz. However, different from the simulated results in Figure 5.6 where no significant attenuation of the MPI signal is observed, the attenuation of signal up to 10 dB is measured in the range from 300 kHz to 600 kHz. The difference between the simulation and measured results might due to the difference in the component values used for simulation from the real component values in the MPI system.

The attenuation of the MFH signal with the combination of self compensation effect and the receive filter can be obtained from by measuring the transfer function from the impedance matching to the LNA output of the new receive chain. The measurement setup and results are shown in Figure 5.21. At the MFH frequency, the attenuation of the MFH signal is −55 dB, −77 dB and −61 dB of the x, y and z channel. Subtracting the 40 dB amplification ratio of the LNA, the MFH signal is attenuated by −95 dB, −117 dB, −101 dB when entering the LNAs. According to the calculation in section 5.2.4, the residual signal is below the maximum input signal of the LNAs. According to the transfer function, the attenuation effect is sensitive to frequency. When working under full power, the resonant frequency of the MFH system increases because the components values of the impedance matching circuit changes with the temperature increase due to the large current flowing through the circuit. Therefore, the notch of the receive filter is tuned to a frequency slightly higher than the MFH frequency 706.7 kHz so that the MFH signal drifts towards the notch of the receive filter to ensure sufficient attenuation of the MFH signal.

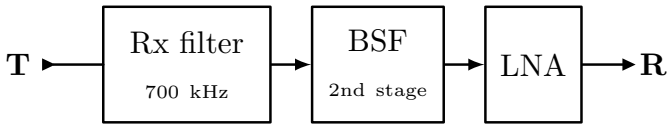

(a) Measurement schematic of the resonant frequency and impedance measurement. Rx filter: receive filter.

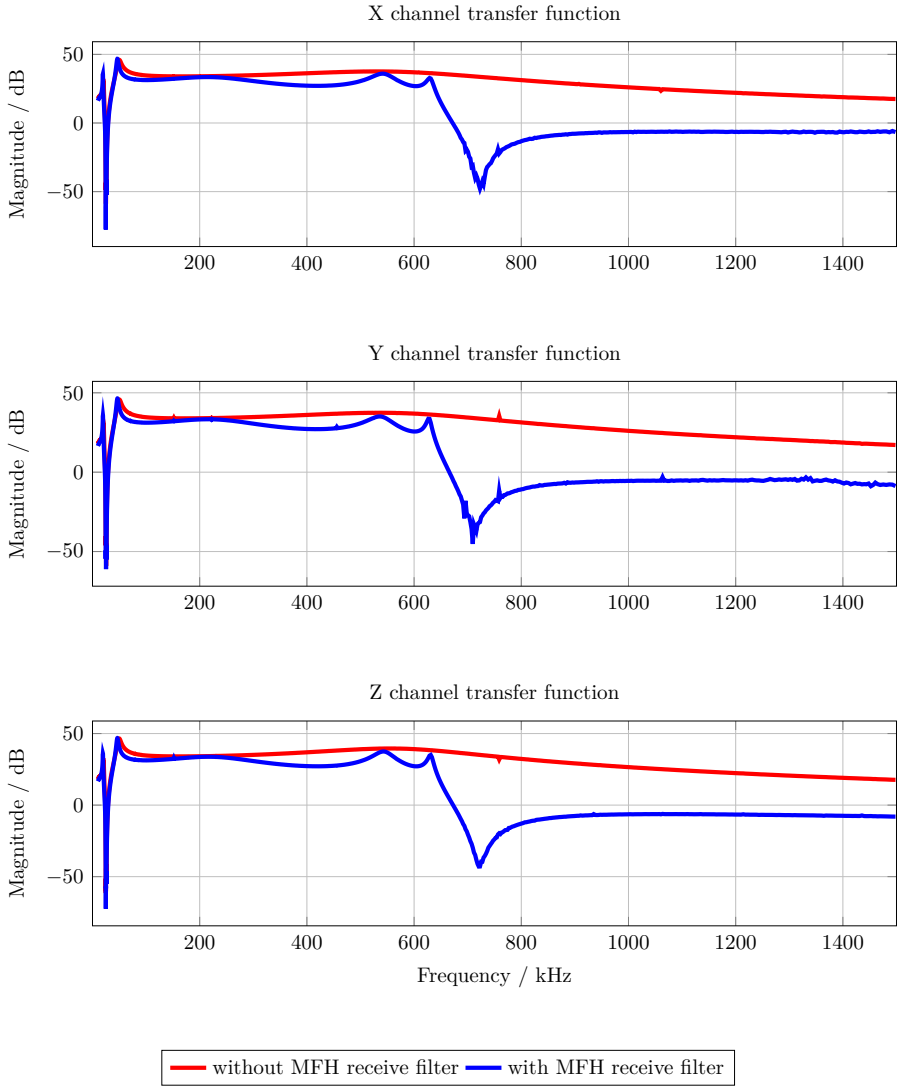

(b) Transfer function of the MPI receive chain with and without the MFH receive filters.

Figure 5.20: Measurement setup and result of the integrated hyperthermia insert.

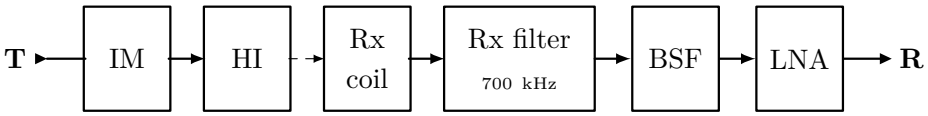

(a) Measurement schematic of the resonant frequency and impedance measurement. Rx filter: receive filter.

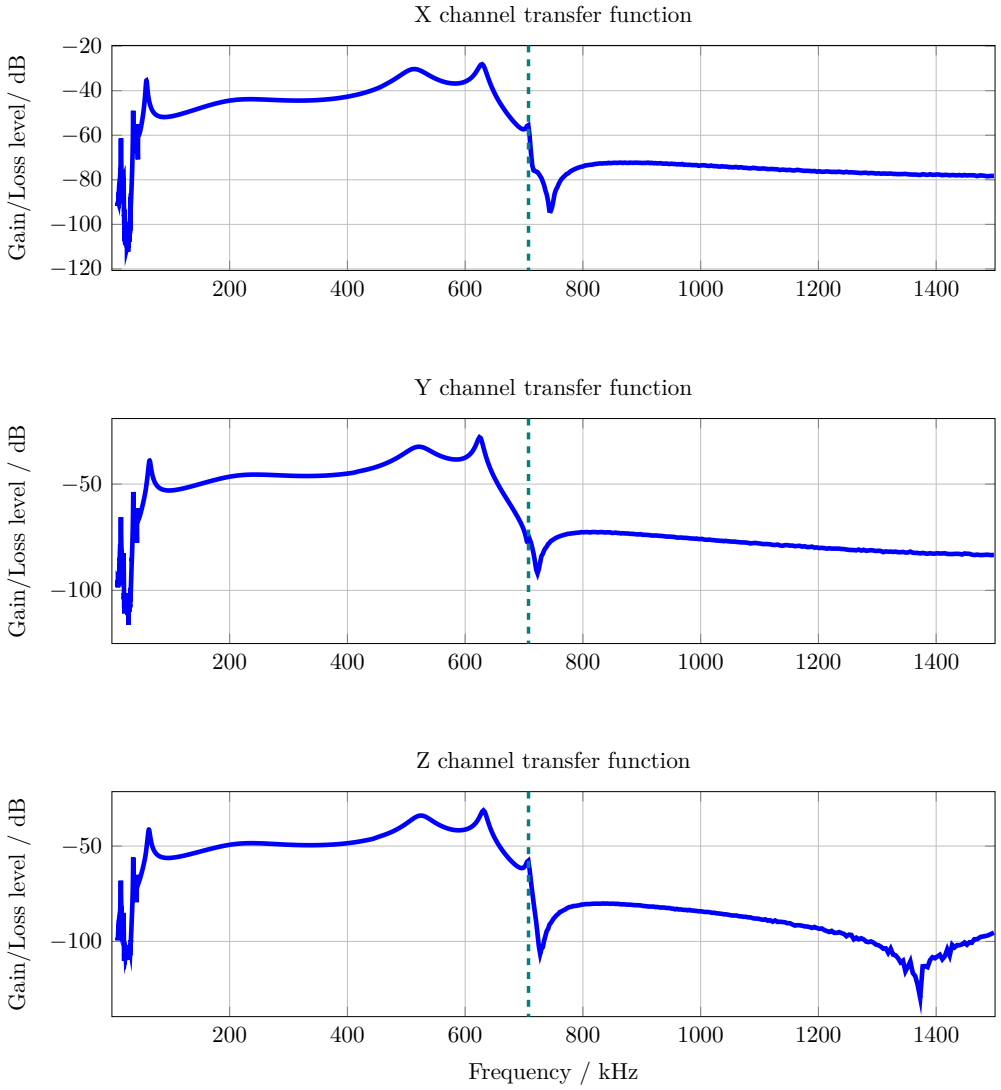

(b) Transfer function from the impedance matching to the LNA output with the receive filter.

Figure 5.21: Measurement setup and result of the integrated hyperthermia insert.

5.5.7 Power test

Power tests are performed on the integrated MPI-MFH platform to measure the residual MFH signal after filtering. In these tests, the LNAs in the MPI receive chain are activated and amplify the receive signal. The power level of the residual MFH signal can be obtained from the signal spectra of the LNA output signal. Due to the mismatch of the load impedance caused by the send filter, the amplifier sends signal directly to the MFH system without the send filter. For each test, the power amplifier is enabled for 30 seconds. After the amplifier is enabled, an MPI measurement is carried out with the settings shown in Table 5.5

Table 5.5: MPI measurement parameters of the power test.

Averages	1
Repetitions	100
Bandwidth	1.25 MHz
Drive field	0 mT
Focus field	0 mT
Selection Field	1.25/1.25/2.5 mT

The measurement finishes within 30 seconds. The power of the MFH signal in the x, y and z channel is noted and plotted in Figure 5.22. The MFH signal increases with the send power. It should be noted that a slightly higher MFH frequency is used from 200 W to match the load as discussed in section 5.5.6. Therefore, the attenuation of the signal increases and can be observed on the decreased residue MFH signal in the figures. Despite the passive compensating and filtering, the signal at the MFH frequency increases significantly compares to the noise level. Nevertheless, the residue MFH signal are within the maximum power level of 0 dBm and comparable to the particle signals which may reach around −40 dBm.

During the test, the coil temperature T_{coil} measured by the PT100 is observed using the MPI control software ParaVision (Bruker BioSpin, Germany). The coil is cooled down to around 17 °C before the next test starts. The coil temperature at the beginning of each test, the maximum coil temperature during the test and the temperature increased during the test are shown in Table 5.6. The maximum coil temperature increases with the power applied on the insert. Applying 600 W, the coil temperature increases for 20.6 K within 30 seconds. In all the tests, the

temperature of the insert stay below 40 °C.

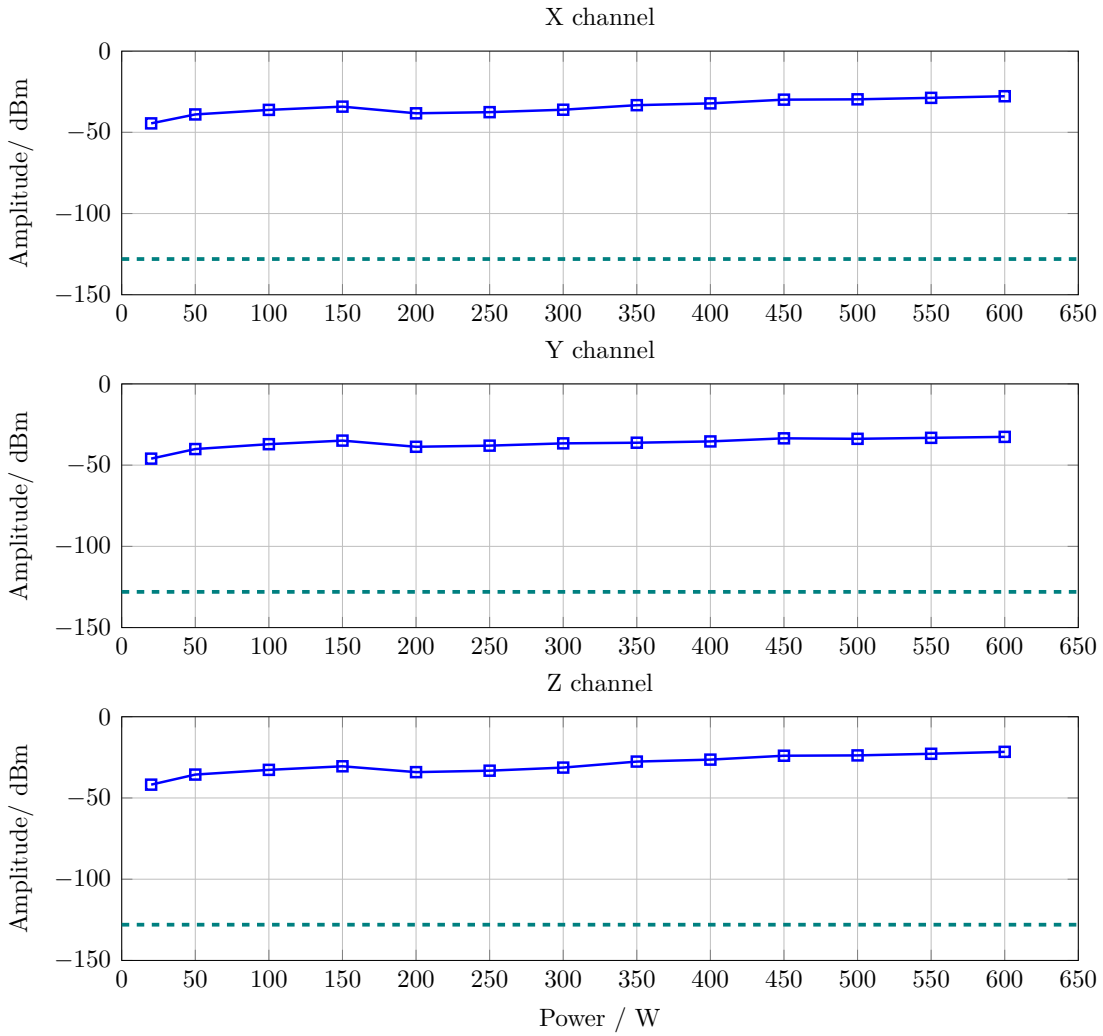

Figure 5.22: Residue MFH signal in the MPI receive chain with different send power. The green dashed line indicates the noise level without any MFH signal.

5.6 Particle heating using the integrated system

The integrated system is used to heat up MNP samples. Figure 5.23 shows the setup of the particle heating experiments. A 3D printed phantom is placed in the hyperthermia insert to hold the particle samples at 9 positions around the center of the MPI scanner (Figure 5.23). The temperature of the particle samples is measured by a thermal camera. Glass test tubes with 6 mm diameter are used to contain the

Table 5.6: Coil temperature measured by the PT100 temperature sensor during the power test.

Power	T_{coil} start/°C	T_{coil} max./°C	ΔT_{coil}/°C
100	17.7	20.1	2.4
200	17.8	27.4	9.6
300	17.2	29.1	11.9
400	17.4	31.8	14.4
500	17.3	34.8	17.5
600	17.5	38.1	20.6

particle solution. The wall thickness of the test tubes is less than 1 mm and uniform everywhere, which is important for an accurate temperature measurement. The test tubes are placed horizontally in the holes of the phantom. The particle solution is fixed with silicon in the tube to prevent spilling. Non-selective heating and selective heating of the samples are presented in this section.

5.6.1 Non-selective heating

The non-selective heating experiment is conducted without the MPI selection field and with samples of different iron concentrations. In this experiment, all samples are heated up by the high frequency magnetic field and the heating effect of different concentrations is compared. The desired temperature increase is 4 K for the application in this work to open the BBB. 27 µL Synomag-D 70 nm MNP with different iron concentration from 1.11 mg/mL to 10 mg/mL (stock concentration) are placed in the phantom. The hyperthermia insert works with 600 W at 714 kHz continuously for 130 s. The thermal pictures of the phantom at the beginning of heating and after 40 s are shown in Figure 5.24. The temperature increase ΔT of each sample and the hyperthermia insert measured by the thermal camera is plotted in Figure 5.25. The results show that all samples are heated up by the hyperthermia insert. The heating effect decreases fast with the iron concentration. Nevertheless, the sample with the lowest concentration of 1.11 mg/ml is heated up by 4 K in the experiment. It has to be noticed that the magnetic field generated by the hyperthermia insert is not homogeneous; the sample placed at the center is heated by a weaker field than the samples at other positions. However, it still

(a) Temperature measurment of the phantom test. A thermal camera is placed 1.5 m away from the opening of the scanner bore.

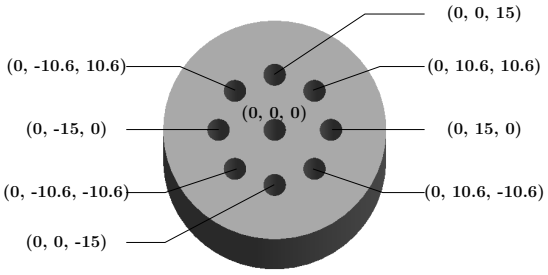

(b) 3D printed phantom. The sample can be placed in the holes at different positions.

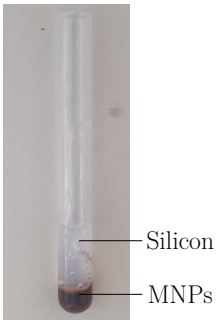

(c) Glass test tube with the MNP sample solution fixed with silicon.

Figure 5.23: Setup of the partical heaitng measurement with the phantom.

exhibits the best heating effect due to its highest iron concentration. According to Figure 5.25, the temperature of the hyperthermia insert increases significantly during the experiment. This confirms the results from the cooling capability test in chapter 4 that the maximum continuous heating time of the insert is limited.

5.6.2 Selective heating

Selective heating experiments are conducted to validate the localized MFH realized by the hyperthermia insert and the selection field of the MPI as well as determine the thermal resolution.

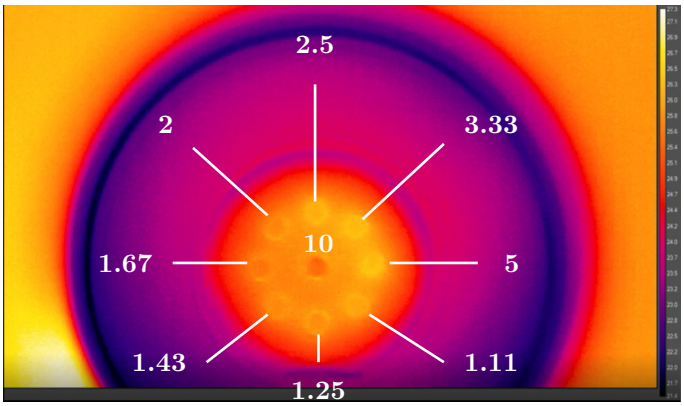

(a) $t = 0s$

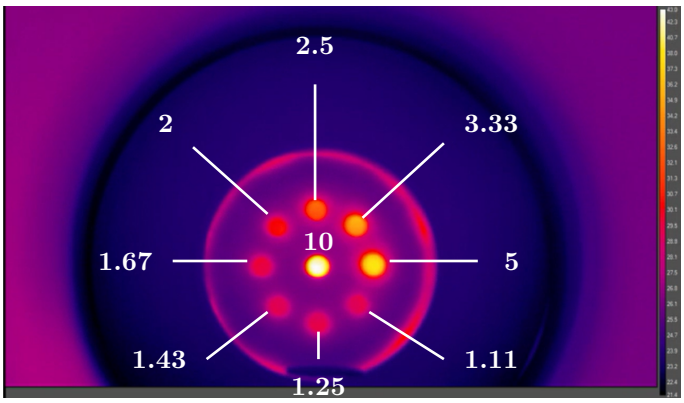

(b) $t = 40s$

Figure 5.24: Non selective heating of samples with different iron concentrations. The iron concentration of each sample is marked on the picture in units of mg(Fe)/mL. The sample with the highest concentration shows the best heating effect.

Selective heating of a phantom

In this experiment, the same phantom in the non-selective heating experiment is used. Nine identical samples of 27 µL undiluted Synomag-D 70 nm MNP are placed in the phantom. The integrated system is used to individually target each sample for 20 s. The heating starts from the sample at (0, 0, 15) and moves clock-wise, at last the selection field is removed and all samples are heated up. The selection field is set to 1.1 T/m, 1.1 T/m and 2.2 T/m for x, y and z direction in this experiment to target all the samples. The temperature of all samples at different time point is shown in Figure 5.26.

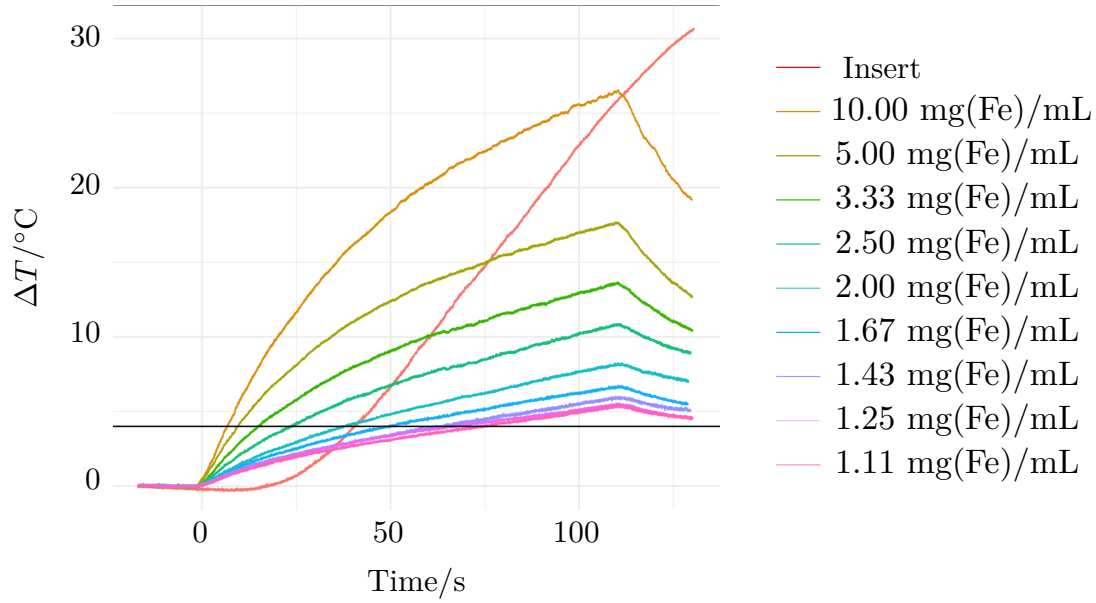

Figure 5.25: Temperature increase of the particle samples and the hyperthermia insert.The MFH field is on at 0 s. The black line marks the 4 K heating target using the hyperthermia insert.

Thermal resolution of selective heating

The thermal resolution of selective heating can be obtained from the SAR profile of a single vial sample measured at different positions with the gradient field. A 27 µL undiluted Synomag-D 70 nm MNP sample in a 3 mm × 3 mm × 3 mm vial is used for the measurement and moved by the robot along the x,y and z direction at 2 mm, 1 mm, 0.5 mm steps, respectively. At each location, the MFH is applied with a frequency of 714 kHz and a power of 300 W for 30 s and the temperature of the sample is recorded using a fiber optic thermometer (Fotempmk, Weidmann Optocon, Germany). The FFP is fixed at the origin of the MPI coordinate system for all measurements and the gradient field is 1.25/1.25/2.5 T/m for the x, y and z direction. Same localized MFH is applied on a 27 µL water sample as control. No temperature increase has been observed, confirming that Joule heating of the hyperthermia insert due to high current in the coil and subsequent conduction or convection heat transfer is not responsible for the heating observed within the particle samples. The data points are plotted as a function of position and fitted to a Gaussian functions in Figure 5.27. The full-width-at-half-maximum (FWHM) of the fitted curve is considered as the thermal resolution for the single vial sample, which are 4.4 mm, 4.7 mm,2.4 mm for the x, y and z direction.

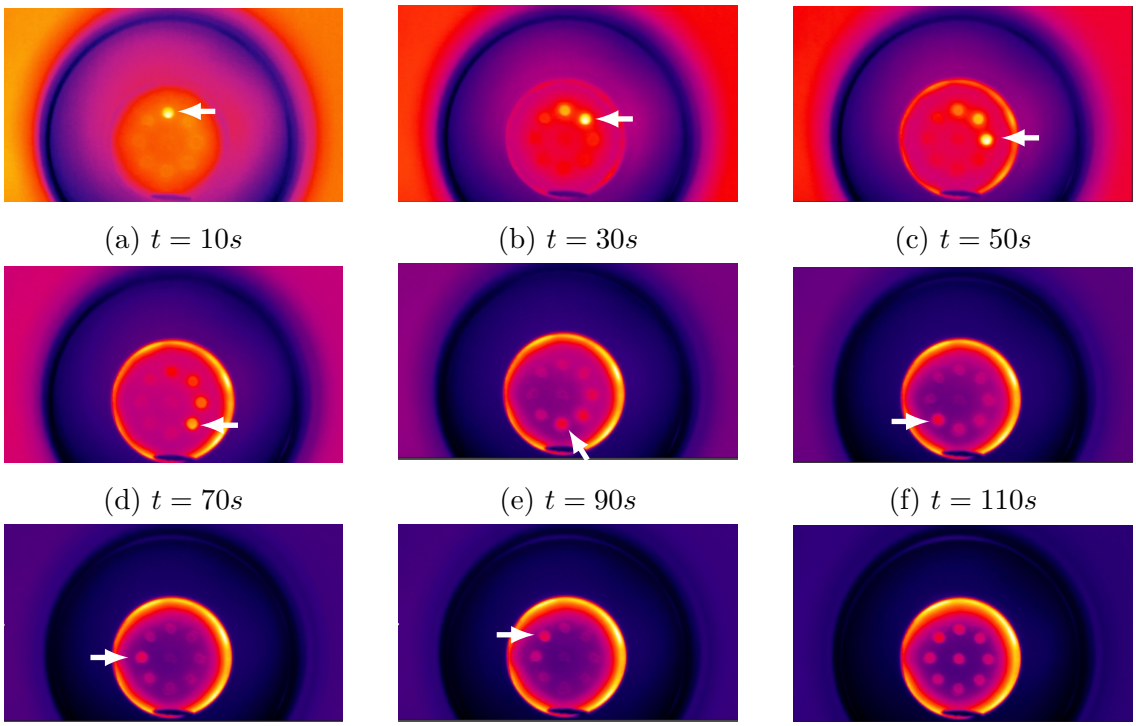

(a) $t = 10s$ (b) $t = 30s$ (c) $t = 50s$

(d) $t = 70s$ (e) $t = 90s$ (f) $t = 110s$

(g) $t = 130s$ (h) $t = 150s$ (i) $t = 170s$

Figure 5.26: Selective heating of particle samples at different positions. (a)-(h): The samples are heated in clock-wise sequency. (i) All samples are heated up. From 70 s the hyperthermia insert gets hot and a "ring" of its inner wall can be observed on the pictures. The color bar is given in Figure 5.24.

5.7 Continuous heating

As presented in chapter 4, the duration that hyperthermia insert can work continuously is limited. This is mainly due to the high temperature of the heating coil when working under high power. The temperature increase will change the parameters of the resonant circuit, which results in the mismatch of the hyperthermia insert. The load mismatch is reflected on the increasing reverse power seen by the RF power amplifier during the test. To protect the amplifier, the maximum reverse power is limited to 100 W. With the current cooling system, the temperature of the coil stays relative stable up to around 350 W. The reverse power is below 20 W when working continuously for more than 20 minutes. With higher power, the reverse power keeps increasing with the increasing temperature of the heating coil. The reverse power can be reduced by adjusting the send frequency. As discussed in chapter 4, the load impedance is frequency dependent.

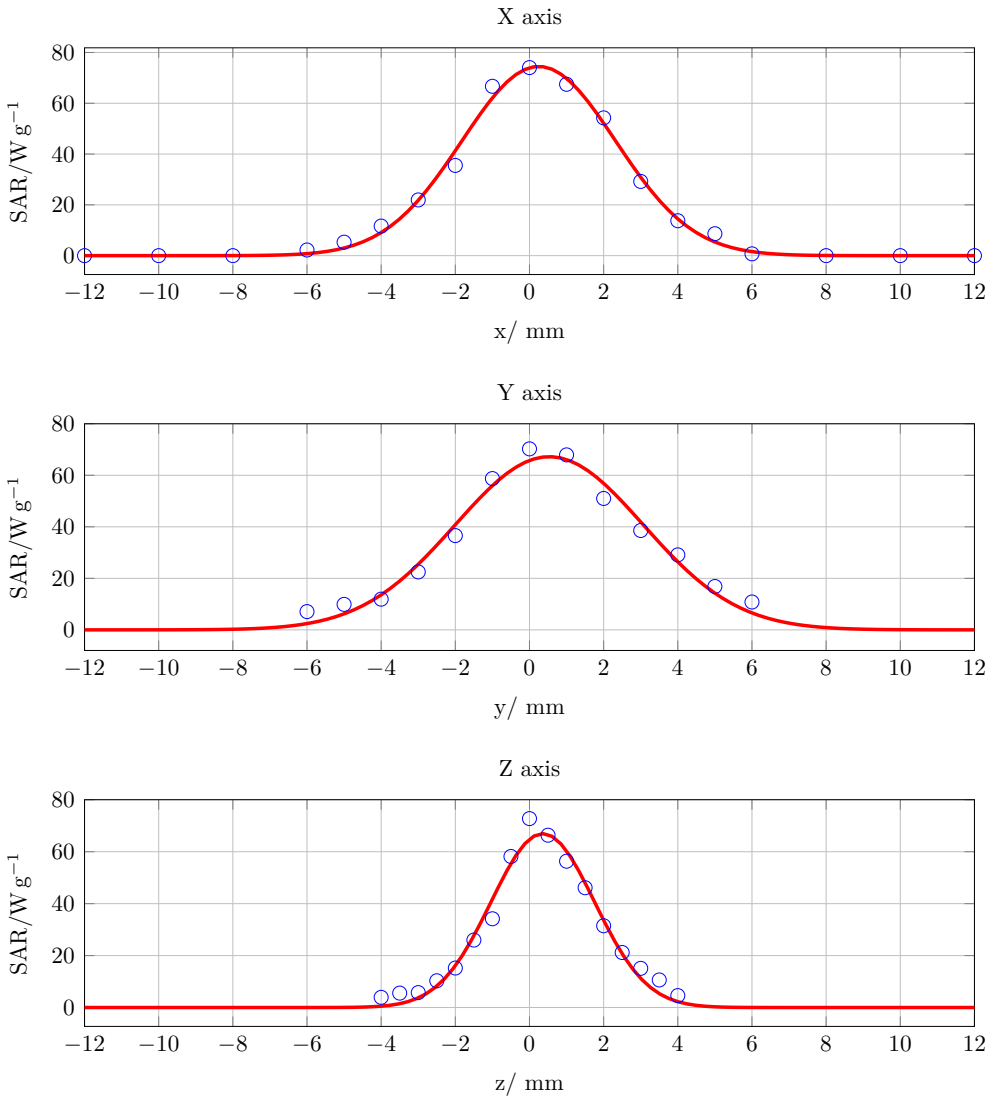

Figure 5.27: SAR profiles of the x, y and z axis. The FFP is fixed at (0, 0, 0). The measured values are marked with blue circles and the red curves are the fitted Gaussian functions. Due to the measurement errors, the SAR values at (0,0,0) are slightly different for each axis.

By shifting the send frequency to a higher value, the load mismatch is eliminated and the reverse power decreases. However, as can be seen in Figure 4.23, no plateau is reached during the heating cycle. Therefore, the frequency has to be continuously adjusted when the insert is working to keep the reverse power at a reasonable value. Another important factor that restricts the working time of the hyperthermia insert is the temperature of the inner tube of the insert. During the high power test, the hottest point can be observed at the inner tube where it

directly contacts the litz wire of the heating coil, which can reach 50 °C in 60 s. The inner tube is made of PMMA, whose mechanical behavior is temperature-dependent and should be kept under 70 °C for proper working [82, 83]. In the high power tests presented in the previous chapters, the temperature of the hyperthermia insert inner tube is monitored and kept under 60 °C. With the two restrictions, the longest time that the integrated hyperthermia insert can work continuously under 600 W is around 120 seconds. In the presented work, the hyperthermia insert is designed to work with duty cycles. Although the insert can work stably in this way for more than half an hour, this can not be considered as continuous heating since the particles are cooled down during the long cooling cycle. However, a continuous heating would be beneficial for many clinical applications, for example increasing the permeability of the blood brain barrier, to realize a more effective hyperthermia therapy by heating the tissue for a longer duration.

5.7.1 Heating requirement

Figure 5.28a shows the desired MNP heating effect of the hyperthermia insert when working continuously. After the hyperthermia insert is switched on, the MNPs are heated up immediately trough the magnetic field. Due to the heat exchange with the environment, the heating rate gradually slows down until an equilibrium is reached. The temperature of the plateau is the therapy temperature which should be around 4 to 6 K higher than the normal body temperature. The therapy duration should last 3 to 10 minutes. The hyperthermia insert has to work continuously during the whole process. An alternative is to have the "quasi-continuous heating" shown in Figure 5.28b. The concept is similar as the interleaved heating, where the hyperthermia insert works in duty cycles so the coil can cool down during the cooling cycles. The difference is that the cooling cycle has to be as short as possible to ensure that the MNP temperature stays in the range in which the therapy is effective. In other words, $\Delta t_1 << \Delta t_2$ and $T_{\text{Therapy1}} - T_{\text{Therapy2}} < 2\,\text{K}$.

5.7.2 Cooling optimization

To fulfill the heating requirement, the cooling system of the hyperthermia insert has to be further optimized to prevent coil overheat during the therapy. The cooling

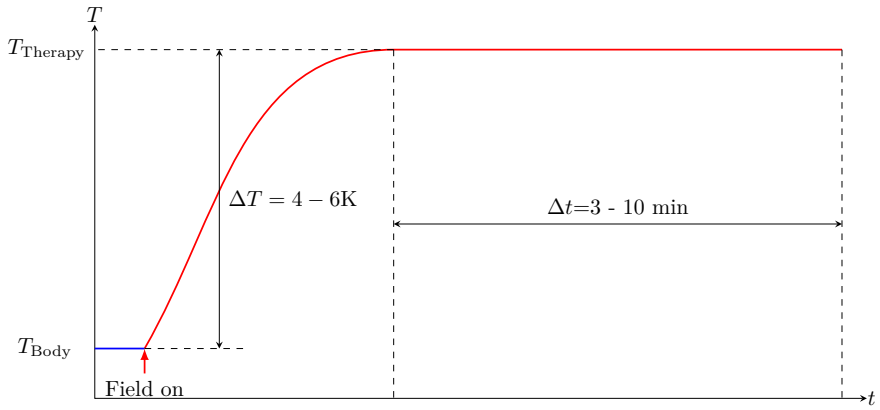

(a) Continuous heating requirement of the hyperthermia therapy.

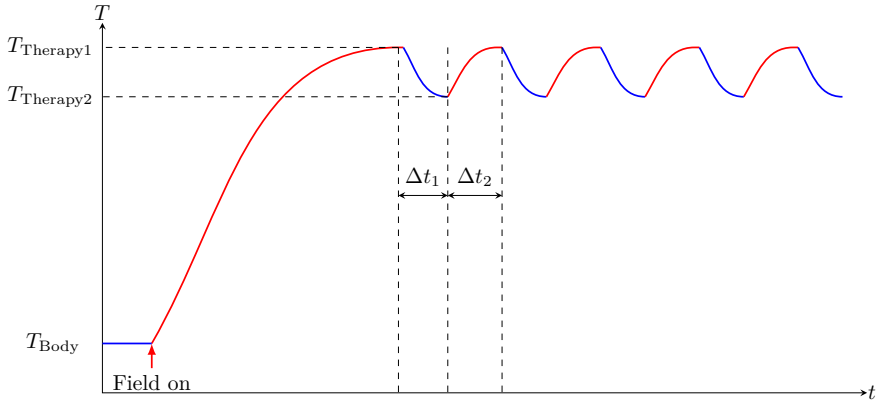

(b) Quasi-continuous heating achieved with interleaved heating - cooling cycles.

Figure 5.28: Heating requirement of the hyperthermia therapy. The red curve indicates the hyperthermia insert is on and the blue curve indicates the hyperthermia insert is off.

unit design has a great influence on the cooling efficiency. Modifications can be made to increase the coolant flow and the contact area between the litz wire and the coolant. However, the cost is high to re-design and manufacture the cooling unit. Therefore, within the frame of this work, the cooling effect is improved from the following two aspects.

Increasing cooling capacity

The cooling capacity Q' can be calculated with:

$$Q' = m' \cdot C_{\mathrm{p}} \cdot \Delta T \tag{5.2}$$

where m' is the mass flow rate of the coolant, C_p is the specific heat capacity of the coolant and ΔT is the change in temperature of the coolant between the inlet and outlet. Besides reducing the flow resistance of the cooling unit, the flow rate can be increased by applying higher pressure from the cooling pump. With the current MPI cooling system, the pressure can be temporarily increased to 1.5 bar by reducing the pressure of the drive field coil cooling, since the drive field is off when the hyperthermia insert is working. ΔT can be increased by changing the outlet temperature of the chiller. To avoid condensation of water in the MPI system, the MPI default coolant temperature is 16 °C. For the continuous heating test, it is reduced to 12 °C to improve the cooling efficiency.

Air cooling

Extra air cooling can be used to cool down the inner tube of the insert. With the current cooling unit design, only one side of heating coil has direct contact to the coolant while the other side contacts the inner tube. As a result, the contacting surface of the inner tube and the heating coil cannot be cooled properly by the coolant. The cold air carries away the heat conducted from the heating coil to the inner tube and keep the inner tube at a stable temperature. The effectiveness of the air cooling is influenced by the air flow rate, which is reduced by the phantom or the animal cassette placed in the hyperthermia insert. To test the scenario of animal experiments, a small rat animal cassette is placed inside the hyperthermia insert. The temperature of the hyperthermia insert inner tube during continuous heating is measured by a thermal camera. The outer diameter of the animal cassette and the hyperthermia insert bore diameter are 59 mm and 60 mm respectively, therefore the space for air cooling is quite limited. The hot spot observed in Figure 5.29a indicates that the cooling of the inner tube is not sufficient for continuous heating. Figure 5.29b shows the result measured with an animal cassette which has a smaller diameter at the front part. With more air flowing through, the temperature of the inner tube stays below 30 °C.

5.7.3 Continuous heating test

A continuous heating test is performed with the improved cooling system. The RF power amplifier is controlled by the MPI system and sends 600 W to the insert.

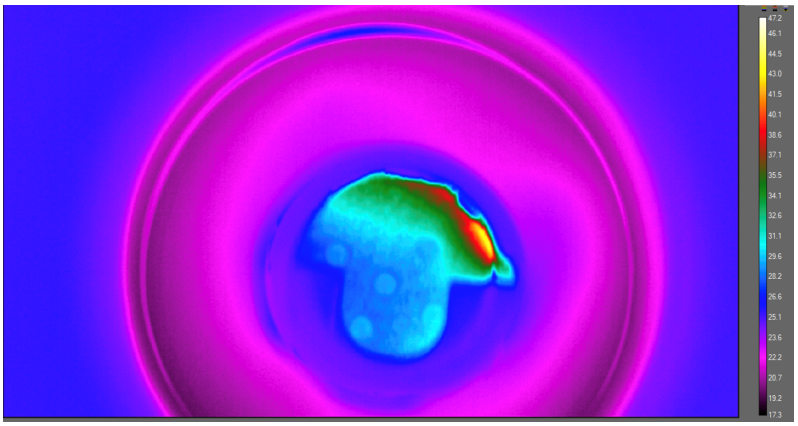

(a) Temperature of the hyperthermia insert with the original animal cassette.

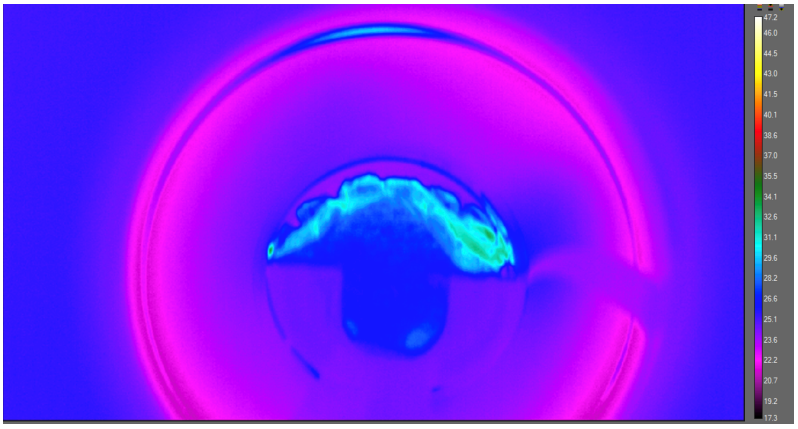

(b) Temperature of the hyperthermia insert with the diameter reduced animal cassette.

Figure 5.29: Temperature of the hyperthermia insert with animal cassette.

Synomag-D 70 nm samples with 0.5 mg/ml and 0.75 mg/ml iron concentration are heated up. The temperature of the hyperthermia insert inner tube and the particle sample is measured by the thermal camera. The quasi-continuous heating mode is tested with 20 s heating and 1 s cooling for 9 minutes. The continuous heating is tested for 11 minutes without any break. The temperature increase of the samples and the hyperthermia insert is shown in Figure 5.30.

In the quasi-continuous heating test, the sample temperature increases 4 K in approximately 4 minutes. A plateau is reached after approximately 5 minutes. The sample temperature decrease is less than 5 K during the 1 s cooling time and the temperature increase maintains above 4 K. Compared to the samples, the hyperthermia insert stays relatively cool at around 27 °C.

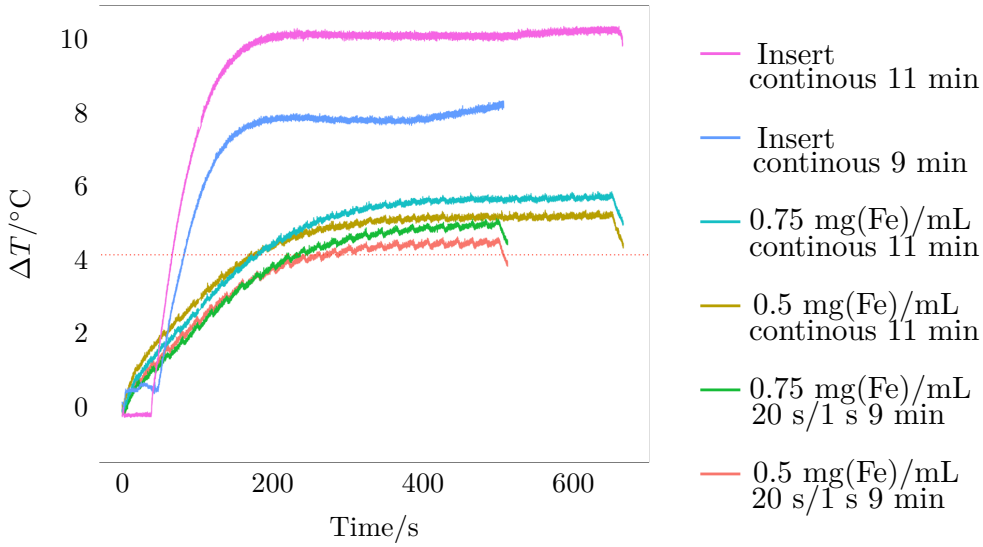

Figure 5.30: Temperature of the hyperhtermia inner wall and the samples during the continuous heating test. The red dashed line marks the 4 K temperature increase.

In the continuous heating test, the sample temperature increases 4 K in approximately 3 minutes. A plateau is reached after approximately 5 minutes. The sample temperature in plateau state is about 2 K higher than the quasi-continuous heating result. The hyperthermia insert inner wall is heated up to approximately 38 °C at the end of the test. The reverse power detected by the power amplifier is in the critical range in both tests.

5.8 Summary and discussion

In this section the hyperthermia insert is integrated and works properly in the preclinical MPI system, marking the realization of a MPI-MFH platform. 3D localized MFH is achieved with the platform with a thermal resolution of 4.4 mm, 4.7 mm, 2.4 mm for the x, y and z direction. The platform can be used for further exploring of localized MFH and unlock various researches in medical field.

The main components of the MFH system are installed and functionable except for the impedance matching network and the send filter. As planned in Figure 5.8, the impedance matching network should be installed in the enclosure of the scanner. Due to the high current and voltage across the circuit when the hyperthermia insert is active, the whole circuit should not be in the operational

area of the MPI scanner for the safety of operating personnel. Within the frame of this work, the impedance matching network can function normally but is not fully installed. The final installation of the send filter can only be finished after the retune of its center frequency. Nevertheless, the localized MFH is not affected by the absence of the send filter. Besides, the analog control of the RF power amplifier is not fully realized. The forward power and reverse power cannot be monitored by the MPI scanner. The MPI control unit has to be extended to have extra analog input ports for the signal from the amplifier. Another option is the digital control of the amplifier using serial connection, which provides the same functionality as the analog control. The advantage of digital control is that it provides the control of the send power frequency, which cannot be set using analog control. Furthermore, the temperature information of the RF amplifier and the impedance matching network is required to have a full temperature monitoring of the MFH system.

The compatibility of the hyperthermia insert is tested. It has to be noticed that the integration process is conducted with a different preclinical MPI scanner than in chapter 4. Despite the same design of both scanners, slight differences in their field profiles are expected. Consequently, the decoupling effect of the hyperthermia insert is evaluated again to ensure that the same coil topology can be used for both scanners. The promising decoupling effect shows that the consistency between the two scanners is good and no specific coil topology design for each individual scanner is required. High power test results proof that by the combination of using passive compensation and filtering, the sensitive low noise amplifier of the MPI system is protected against over voltage from the fast oscillating magnetic fields. If operated fast enough, blanking circuits which disconnect the low noise amplifier from the receive chain can be used as well.

The localized MFH using the MPI-MFH system is explored with MNPs. By moving the FFP, MNP samples placed at specific positions can be targeted and heated up selectively. The alignment of the FFP and the MNP sample is necessary for the precise selective heating, especially in z direction which has the highest thermal resolution. In the experiment, some samples are not heated up when moving the FFP to the expected position. To locate the actual position of the samples, the FFP is moved around the expected position until the heating effect of particles is observed. A possible source of misalignment is the manufacture imperfection of the phantom and the tilt of the phantom placement. In future experiments, an image

of the samples can be acquired using the MPI system to ensure proper alignment during therapy.

The SAR profiles are obtained for 3 directions. The shape is very similar to that of the 1D MPI PSF given that the same nonlinear saturation physics mediate both MPI and MFH. In this work, the SAR profiles are measured at each point only once. The vials used are 3 mm × 3 mm × 3 mm. Ideally, point sources should be used. More accurate SAR profiles could be obtained with smaller measurement step, sample volume and more measurement times. Besides, the control measurement with water sample is only performed at the center position, the measurement should be repeated at each point to eliminate the influence of environment heating. The measured SAR profiles are not symmetric to the 0 position, which potentially due to the inhomogeneity of the MFH field. Differing heat transfer conditions, thermal probe placement in the particle solution, and sample concentration changes due to evaporation could also have contributed to the observed variation.

From the SAR profiles the thermal resolution of the integrated system can be derived. The results obtained in section 5.6 is achieved with 8.4 mT MFH field strength and the maximum gradient (1.25/1.25/2.5 T/m) that the MPI scanner can provide. Higher thermal resolution can be realized with an enhanced gradient field [84]. There is a trade off between thermal resolution and heating efficiency due to the spatial localizing effect of the FFP. Lower gradients and higher MFH field strengths will allow for more efficient heating of a larger volume. The required thermal resolution in a clinical therapy context has to be defined by further research regarding the specific applications.

The capability of the hyperthermia insert of continuous heating is enhanced in this chapter without re-designing of the cooling unit. The heating requirements for opening the blood brain barrier are fulfilled with the proposed cooling concept. The chosen parameter of quasi-continuous heating can be further explored. In the frame of this work, up to 25 minutes heating with 40 seconds heating and 2 seconds cooling has successfully been tested.

6

Summary

The MPI-MFH platform combines the two modalities which both rely on the interaction of magnetic particles and oscillating magnetic fields. Localized MFH can be achieved by superimposing the selection field used for spatial encoding in MPI on the MFH field. The presented thesis constitutes an MPI-MFH theranostic platform realized by integrating a hyperthermia insert into a preclinical MPI scanner. Various aspects of the MPI-MFH system are examined and a localized MFH on a phantom is explored.

In chapter 1 and chapter 2, the background and theory principle related to the work of this thesis are presented. The physical properties enabling the MPI including the signal generation and spatial encoding are introduced. To understand the hardware components, the MPI signal chain and the analog filters are explained. Subsequently, the physical principle of MFH and the similarity to that of MPI are discussed. Furthermore, the clinical application of MFH in cancer treatment and brain drug delivery are introduced. The concept of combing MPI and MFH to form a theranostic platform is proposed and motivated by discussing the demand of localized MFH in medical applications. Finally, the challenge of hardware realization of the MPI-MFH system is discussed.

In chapter 3, the problem of coil topology optimization of the hyperthermia insert is stated. A metaheuristic algorithm is chosen to solve the problem. Two algorithms, PSO and DE are introduced and tested. To improve the result, a hybrid method is proposed based on the two algorithms and evaluated using benchmark functions. The hybrid method has shown a better performance than the original algorithms, and is used to optimize the coil topology of the hyperthermia insert.

In chapter 4, the coil topology found by the hybrid method is used for simulations, which provide information of important parameters of the hyperthermia insert. Prior to the design of the hyperthermia insert, a skeleton prototype is manufactured. The prototype is used to perform small signal measurements to validate the self-compensation effect of the coil. Based on the prototype design, the final design of the hyperthermia insert is obtained. In the manufacture of the hyperthermia insert, both subtractive and additive manufacturing are utilized to fulfill the electrical and mechanical requirements of different components. The completed MFH circuit is implemented with an impedance matching network and a RF power amplifier. To achieve the suitable field strength for MFH, a cooling system for the hyperthermia insert and the impedance matching network are implemented and tested under different power levels. The electric and magnetic characteristics, as well as the capability to heat particles of the hyperthermia insert have been evaluated. The presented hyperthermia insert is capable to generate a MFH field at around 700 kHz up to 10 mT and work with 60 s/240 s heating/cooling cycles.

In chapter 5, the hyperthermia insert is integrated into a preclinical MPI scanner. At first the signal chain of the MPI-MFH system is introduced. Besides the components introduced in chapter 4, two filters have to be designed and implemented. A specific plan of the hardware installation and risk analysis have been made, after that the components are installed in the MPI system. The fully installation of the impedance matching network and the send filter is not completed within the scope of this thesis. Following the installation, the MPI-MFH system is tested and evaluated. The installed hyperthermia insert and filters are evaluated by measuring the transfer functions and the residue MFH signal in the MPI receive chain. Furthermore, the inter-system communication is discussed and tested. The MPI system control of the power send to the hyperthermia insert and the monitor of the flow and coil temperature are realized while the signal input from the RF power amplifier is still incomplete. Finally, the MPI-MFH system is used to apply MFH on MNPs samples. Non-selective heating

without gradient field is conducted, proving the normal function of the hyperthermia insert after the integration process. The experimental demonstration of localized MFH is performed on the phantom by targeting samples placed at different positions. Only the sample at the FFP has shown temperature increase while the temperature of samples at other locations remains unchanged. The thermal resolution with 300 W MFH and 1.25/1.25/2.5 T/m gradient, are identified on the x, y and z axes. Further improvement of the cooling to realize continuous heating using the hyperthermia insert, in this thesis, quasi-continuous heating up to 25 minutes with 40 seconds heating and 2 seconds cooling has been tested.

7

Discussion and outlooks

Contents

7.1 Discussion

In the presented work, it has been shown that MPI and MFH can be combined, allowing localized magnetic hyperthermia with 4.4 mm, 4.7 mm, 2.4 mm for the x, y and z direction. The implemented MPI-MFH platform is proven to be capable of targeted heating samples placed at different positions. With an iron concentration of 10 mg/mL, SAR up to 190 W/g is achieved using Synomag-D 70 nm particles. The results are promising for the clinical applications such as the reversible opening of blood brain barrier.

Previous researches already showed the feasibility of the combination of MPI and MFH [75, 85]. Hensley et al. proposed a 1D FFL MPI-MFH platform with a

gradient of 2.35 T/m created by two rectangular permanent NdFeB magnets. A solenoid coil is used to generate the MFH field at 353 kHz up to 20 mT. Further, the setup equips with a gradiometric receive coil. Phantom experiments showed that a 7 mm heating resolution can be achieved with the setup. However, there are some limitation with the setup. First, the localized MFH is limited to 1D due to the 1D gradient field. Second, the use of permanent magnets results in an untunable the gradient strength. Finally, although a receive coil is implemented, the 3D MPI imaging of the phantoms was conducted with a separate MPI-only scanner. The advantage of the MPI-MFH platform presented in this work is that it makes use of the gradient field in x, y and z directions created by electromagnets of the MPI scanner. The MFH can be confined in a point (FFP) and moved in three dimension. If a large heating area is desired, the size of the FFR can be varied by reducing the gradient strength so that the FFP is rastered across a larger FOV. This allows a more flexible spatial selection and control of the targeted heating region for different applications. Moreover, with one single device, no registration of two systems is required.

Another work in combing MPI and MFH is done by Wells et al. [86] where the MPI scanner acts as a standalone platform to support the application of MFH. 400 µL Ferucarbotran samples with iron concentration of 935 mmol/L are heated with 3D image acquisition sequences of a commercial preclinical MPI scanner (MPI 25/20 FF, Bruker BioSpin MRI GmbH, Germany). The sample was shown to be heated by around 5 K over the first 2.5 minutes of field exposure. The localized MFH was investigated along the x axis of the MPI scanner, with 3D excitation and 2.5 T/m selection field, the FOV is 2 cm in x direction with measurable heating occurring up to 4 cm from the center of the FOV. The results showed the capability of MPI scanners in MFH. However, as the SAR is expected to increase with the frequency, the 25 kHz MPI frequency is not ideal for MFH, which led to a very low SAR when heating the MNPs with solely MPI scanner, which is a desired property of imaging. In practice, whether such high iron confrontation can be reached in vivo remains unknown and limits the application of the approach. The MPI-MFH platform presented in this work adopts 700 kHz for MFH which achieves a significantly higher SAR and therefore a better heating efficiency.

Theoretically, the MNPs can generate MPI signals and dissipated heat at the same time, which means the imaging and therapy can be carried out simultaneously. This is not achieved within the frame of this work since the LNAs are disconnected

physically in the phantom experiments to protect the electronics. Although the high power test proofs the residue MFH signal is within the maximum input level of the LNAs, further stability tests of the MFH system are required to protect the sensitive receive electronics from sudden high voltage signals. Simultaneous imaging and heating could be achieved using same frequency for MPI and MFH or developing a MPI system with two excitation frequencies [87]. However, both methods face the huge mechanical and electrical challenges to generate the suitable frequencies and manage with the high frequency harmonics for image reconstruction. Nevertheless, the requirement for imaging-guided treatment, i.e. providing particle distribution and temperature can be fulfilled by proper MPI-MFH sequence design and a fast switching between the two modalities. Besides, performing imaging and therapy sequentially has the advantage that a larger FOV can be used for imaging to have more information of the particle spatial distribution and temperature while a smaller FOV for the therapy in the region of interest to achieve accurate control of the heating area .

In this work, the MPI-MFH platform is validated on phantoms with MNP solutions. Theoretical model of the localized MFH with different MNPs is not covered in this work. To predict the behavior of particles in the magnetic field of the frequency and field strength for MFH, more works could be done to determine the suitable physical model for the simulation of the hysteresis loop of MNPs. Together with the field profile of the MPI scanner, the heat production during MFH can be estimated as a function of position along the FFP. The model provides a prediction of the heating effect with different MNPs, field strength and frequency. It should be noted that the heating in vivo may differ significantly from the presented results due to the cooling effect of blood flow, which removes heat from the site of hyperthermia. The MNPs circulation may result in reducing the heating effect as well. For clinical application, further experiments exploring the heating effect in more realistic scenarios e.g. with the influence of blood stream are necessary. The question of the dosage and targeting of the MNPs when conducting in vivo experiments need to be answered. The bio-heat equation [88] could be used to establish thermal models and predict the temperature increase of the tissue [89, 90, 91], the influence of blood flow can be taken into consideration by including the hemodynamic properties of the tissue under treatment [92, 93, 94]. To advance future clinical applications, the MNPs design can be further explored to synthesize particles with good performance in both MFH and MPI.

The presented MPI-MFH platform makes a step forward in combing the two modalities by allowing for MPI and localized MFH in all three spatial dimensions.The platform enables researches in various medical applications such as: tumor therapy, MFH treatment planning, and monitoring with MPI as well as thermal induced targeted drug delivery. Although the in-vivo experiment is beyond the capabilities and time frame of this work, it can be considered as a basis for numerous new therapeutic options.

7.2 Application of the MPI-MFH platform and outlooks

This thesis focuses on the hardware realization of the MPI-MFH platform. This section outlines the current state of the application of the MPI-MFH platform presented in this work and provides a forward-looking perspective on potential developments and medical applications of MPI-guided MFH.

7.2.1 MPI-based thermometry during therapy

The MPI-MFH platform can be extended to achieve simultaneous imaging and temperature mapping using the method proposed by Stehning et al. using a multi-color reconstruction approach [24]. The temperature information inside the body provided by MPI would be a perfect complementary evaluation modality for MFH. Two system matrices for a cold channel and a warm channel can be acquired and used for simultaneous, real-time, 3D spatially resolved temperature and concentration mapping.

To complete the therapeutic function of the MPI-MFH platform a therapy relying on hyperthermia can be designed. A concept of the MPI-MFH sequence is proposed and shown in Figure 7.1. The system is in therapy mode when applying hyperthermia treatment. In therapy mode, the hyperthermia insert is working, and the blanking of the drive field generators and the LNAs is enabled. In the complementary interval of the therapy mode, the system is in the imaging mode, where the image is acquired and the real-time temperature is then estimated. This reconstructed temperature controls the switching between image mode and

therapy mode.

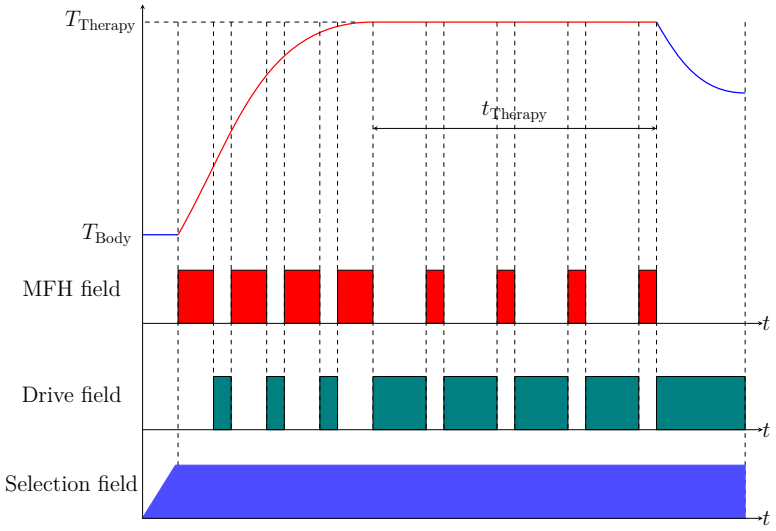

Figure 7.1: The concept of the MPI-MFH sequence. The MFH field and the MPI drive field is enable in turn while the selection field is enable throughout the imaging and therapy mode.

Buchholz et al. [95] applied an MPI-MFH sequence based on the proposed concept on MNP samples using the MPI-MFH platform to retrace the sample temperatures. MNP samples are heated by the MFH field in the therapy mode and MPI signals are acquired during the imaging mode. For every MPI-MFH cycle, MFH was applied for a duration of 5 s and image acquisition (MPI) was done over a duration of 1.1 s. Consequently, MPI-based temperature values were acquired every 6.6 s. The temperatures of the samples were recorded with a thermal camera and compared to the MPI-based temperature values obtained from the multi-color reconstruction. The MPI-reconstructed temperature profiles of the samples aligned with the data obtained from thermal camera measurements in general. It can be seen from Figure 7.2 that the MPI-MFH platform enables imaging, localized heating and non-invasive thermometry for MFH therapy.

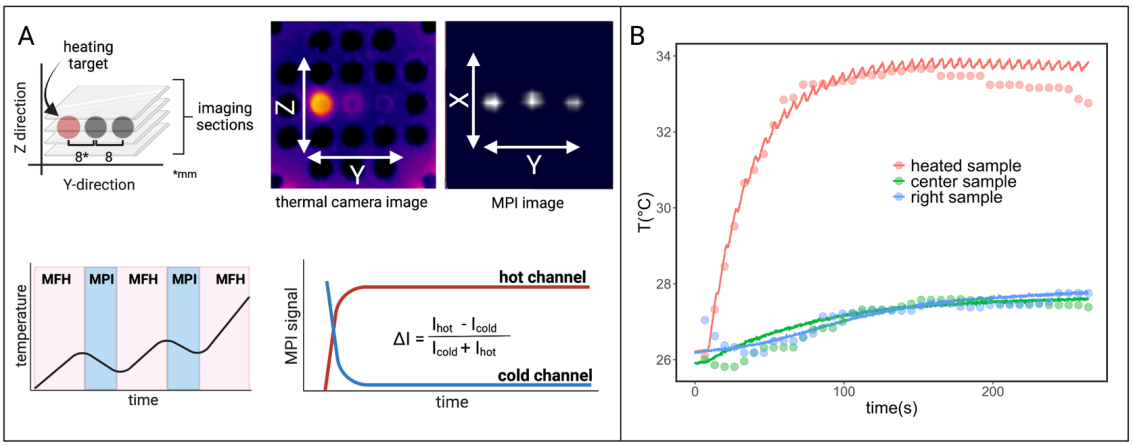

Figure 7.2: Interleaved MPI and localized MFH achieved with the MPI-MFH platform. (A) The MPI images are reconstructed for MPI-based thermometry (B) The reconstructed temperature results (dots) are compared to the thermal camera measured temperature results (solid lines).[95]

7.2.2 Preclinical applications and transition into clinical application

The presented MPI-MFH platform bears the great medical potential of combined MFH and MPI. It can be used for preclinical application studies on biological specimens and animal models.

Recently, an in-vivo pilot study has been carried out using the MPI-MFH platform to investigate localized MPI-based MFH in the rat brain for reversible opening of the blood-brain barrier [96]. MNP boli administered through the tail vein and localized hyperthermia is applied at the rat brain. Temperature increase in the brain was observed after the administration of the bolus, while the core body temperature remained stable. The study demonstrated that the combination of MFH and MNP administration led to a localized temperature increase in the brain, confirming the MFH effect of non-invasive and localized MFH application following systemic administration. However, in the in-vivo experiment, the temperature rise was modest and below the threshold for effective treatment, which is a key challenge of the usage of the MPI-MFH platform in clinical applications. The effectiveness of the treatment could be enhanced by increasing MNP concentrations in the target area, using particles optimized for MFH with high SAR and increasing the MFH field amplitude.

Another major difficulty which needs to be addressed to facilitate the transition of the MPI-MFH platform into clinical applications is the upscaling to human applications similar to MPI [8], since power demand increases severely for larger therapeutic volumes. The corresponding requirements for instrumentation are quite challenging. An intermediate step towards full size human MPI-guided MFH could be the application on smaller, specific body areas like limbs or head, e.g. treatment of brain tumors [97], bone metastases [98], osteosarcoma [99] or reversible opening of the blood-brain barrier for drug delivery [100] and theranostics for neurodegenerative diseases [101].

Publication list

[P1] H. Wei*, A. Behrends*, A. Neumann, A. C. Bakenecker, T. Friedrich , J. Franke, K. Sajjamark,O. Buchholz, S. Bär, U. G. Hofmann, M. Graeser, and T. Buzug, "Integrable Magnetic Fluid Hyperthermia Systems for 3D Magnetic Particle Imaging," *Nanotheranostics*, vol. 8, pp. 163–178, 2024. DOI:10.7150/ntno.90360

[P2] H. Wei, A. Behrends, T. Friedrich, and T. Buzug, "A heating coil insert for a preclinical mpi scanner," *International Journal on Magnetic Particle Imaging*, vol. 6, no. 2 Suppl 1, 2020. DOI:10.18416/IJMPI.2020.2009056

[P3] H. Wei, A. Behrends, T. Friedrich, and T. Buzug, "Using 3d printing to implement a hyperthermia insert for a preclinical mpi scanner," vol. 2, no. 1. Transactions on Additive Manufacturing Meets Medicine, 2020. DOI:10.18416/ammm.2020.2009032

[P4] H. Wei, J. Franke, O. Buchholz, A. Behrends, S. Bär, U. G. Hofmann, T. Buzug, and M. Graeser, T. Buzug, "xtending a commercial preclinical MPI scanner into an MPI-MFH platform using a hyperthermia insert," *International Journal on Magnetic Particle Imaging*, vol. 9, no. 1 Suppl 1, 2023. DOI:10.18416/IJMPI.2023.2303029

[P5] H. Wei, A. Behrends, T. Friedrich, and T. M. Buzug, "Implementation of a heating coil insert for a preclinical mpi scanner designed using depso," in *9th International Workshop on Magnetic Particle Imaging*, 2019.

[P6] O. Buchholz, K. Sajjamark, J. Franke, H. Wei, A. Behrends, C. Münkel, C. Grüttner, P. Levan, D. von Elverfeldt, M. Graeser, T. Buzug, S. Bär, and U. G. Hofmann, "In situ theranostic platform combining highly localized magnetic fluid hyperthermia, magnetic particle imaging, and thermometry in 3d," *Theranostics*, vol. 14, pp. 324–340, 2024. DOI:10.7150/thno.86759

[P7] M. Gräser, F. Wegner, J. Schumacher, M. Ahlborg, K. Gräfe, E. Aderhold, Y. B. Soares, K. Lüdtke-Buzug, A. Neumann, P. Stagge, H. Wei, J. Ackers, and T. M. Buzug, "Magnetic particle imaging," *Die Radiologie*, vol. 62, no. 6, pp. 496–503, 2022. DOI:10.1007/s00117-022-01011-9

[P8] A. Neumann, K. Gräfe, A. von Gladiss, M. Ahlborg, A. Behrends, X. Chen, J. Schumacher, Y. B. Soares, T. Friedrich, H. Wei, A. Malhorta, E. Aderhold, A. C. Bakenecker, K. Lüdtke-Buzug, and T. M. Buzug, "Recent developments in magnetic particle imaging," *Journal of Magnetism and Magnetic Materials*, vol. 550, 169037, 2022. DOI:10.1016/j.jmmm.2022.169037

[P9] A. Behrends, A. Bakenecker, M. Ahlborg, K. Gräfe, J. Schumacher, J. Stelzner, F. Wegner, A. Neumann, Y. Blancke Soares, K. Lüdtke-Buzug, X. Chen, H. Wei, A. Malhotra, T. Friedrich, and T. M. Buzug, "Magnetic particle imaging," in *Imaging Modalities for Biological and Preclinical Research: A Compendium*, ser. 2053-2563. IOP Publishing, 2021, vol. 2, pp. II.8–1 to II.8–10. DOI:10.1088/978-0-7503-3747-2ch12

Bibliography

[1] H. Arami, E. Teeman, A. Troksa, H. Bradshaw, K. Saatchi, A. Tomitaka, S. S. Gambhir, U. O. Häfeli, D. Liggitt, and K. M. Krishnan, "Tomographic magnetic particle imaging of cancer targeted nanoparticles," *Nanoscale*, vol. 9, pp. 18 723–18 730, 2017. DOI:10.1039/C7NR05502A

[2] X. Y. Zhou, Z. W. Tay, P. Chandrasekharan, E. Y. Yu, D. W. Hensley, R. Orendorff, K. E. Jeffris, D. Mai, B. Zheng, P. W. Goodwill, and S. M. Conolly, "Magnetic particle imaging for radiation-free, sensitive and high-contrast vascular imaging and cell tracking," *Current Opinion in Chemical Biology*, vol. 45, pp. 131–138, 2018, molecular Imaging / Chemical Genetics and Epigenetics. DOI:10.1016/j.cbpa.2018.04.014

[3] F. Griese, P. Ludewig, F. Thieben, N. Gdaniec, and T. Knopp, "Imaging and moving magnetic beads with magnetic particle imaging for targeted drug delivery," in *2018 IEEE 15th International Symposium on Biomedical Imaging (ISBI 2018)*, 2018, pp. 1293–1296. DOI:10.1109/ISBI.2018.8363808

[4] A. C. Bakenecker, A. von Gladiss, H. Schwenke, A. Behrends, T. Friedrich, K. Lüdtke-Buzug, A. Neumann, J. Barkhausen, F. Wegner, and T. M. Buzug, "Navigation of a magnetic micro-robot through a cerebral aneurysm phantom with magnetic particle imaging," *Scientific Reports*, vol. 11, no. 1, pp. 1–12, 2021. DOI:10.1038/s41598-021-93323-4

[5] B. Gleich and J. Weizenecker, "Tomographic imaging using the nonlinear response of magnetic particles," *Nature*, vol. 435, no. 7046, pp. 1214–1217, 2005. DOI:10.1038/nature03808

[6] T. C. Kranemann, T. Ersepke, and G. Schmitz, "Towards the integration of an mpi compatible ultrasound transducer," *International*

Journal on Magnetic Particle Imaging, vol. 3, no. 1, 2017. DOI:10.18416/ijmpi.2017.1703016

[7] P. Vogel, S. Lother, M. A. Rückert, W. H. Kullmann, P. M. Jakob, F. Fidler, and V. C. Behr, "Mri meets mpi: a bimodal mpi-mri tomograph," *IEEE Transactions on Medical Imaging*, vol. 33, no. 10, pp. 1954–1959, 2014. DOI:10.1109/TMI.2014.2327515

[8] M. Gräser, F. Thieben, P. Szwargulski, F. Werner, N. Gdaniec, M. Boberg, F. Griese, M. Möddel, P. Ludewig, D. van de Ven *et al.*, "Human-sized magnetic particle imaging for brain applications," *Nature Communications*, vol. 10, no. 1, pp. 1–9, 2019. DOI:10.1038/s41467-019-09704-x

[9] A. Jordan, R. Scholz, P. Wust, H. Fähling, and R. Felix, "Magnetic fluid hyperthermia (mfh): Cancer treatment with ac magnetic field induced excitation of biocompatible superparamagnetic nanoparticles," *Journal of Magnetism and Magnetic Materials*, vol. 201, no. 1-3, pp. 413–419, 1999. DOI:10.1016/S0304-8853(99)00088-8

[10] J. C. Bear, P. S. Patrick, A. Casson, P. Southern, F.-Y. Lin, M. J. Powell, Q. A. Pankhurst, T. Kalber, M. Lythgoe, I. P. Parkin *et al.*, "Magnetic hyperthermia controlled drug release in the gi tract: solving the problem of detection," *Scientific Reports*, vol. 6, no. 1, pp. 1–11, 2016. DOI:10.1038/srep34271

[11] L. Che Rose, J. C. Bear, P. D. McNaughter, P. Southern, R. B. Piggott, I. P. Parkin, S. Qi, and A. G. Mayes, "A spion-eicosane protective coating for water soluble capsules: Evidence for on-demand drug release triggered by magnetic hyperthermia," *Scientific Reports*, vol. 6, no. 1, pp. 1–5, 2016. DOI:10.1038/srep20271

[12] C. S. Kumar and F. Mohammad, "Magnetic nanomaterials for hyperthermia-based therapy and controlled drug delivery," *Advanced Drug Delivery Reviews*, vol. 63, no. 9, pp. 789–808, 2011. DOI:10.1016/j.addr.2011.03.008

[13] A. Yadollahpour and S. Hosseini, "Magnetic nanoparticle based hyperthermia: A review of the physiochemical properties and synthesis methods," *International Journal of Pharmaceutical Research and Allied Sciences*, vol. 5, pp. 242–246, 04 2016.

[14] D. Chang, M. Lim, J. A. C. M. Goos, R. Qiao, Y. Y. Ng, F. M. Mansfeld, M. Jackson, T. P. Davis, and M. Kavallaris, "Biologically targeted magnetic hyperthermia: Potential and limitations," *Frontiers in Pharmacology*, vol. 9, 2018. DOI:10.3389/fphar.2018.00831

[15] B. Thiesen and A. Jordan, "Clinical applications of magnetic nanoparticles for hyperthermia," *International Journal of Hyperthermia*, vol. 24, no. 6, pp. 467–474, 2008. DOI:10.1080/02656730802104757

[16] B. Kozissnik, A. C. Bohorquez, J. Dobson, and C. Rinaldi, "Magnetic fluid hyperthermia: advances, challenges, and opportunity," *International Journal of Hyperthermia*, vol. 29, no. 8, pp. 706–714, Dec. 2013. DOI:10.3109/02656736.2013.837200

[17] A. M. Derfus, G. von Maltzahn, T. J. Harris, T. Duza, K. S. Vecchio, E. Ruoslahti, and S. N. Bhatia, "Remotely triggered release from magnetic nanoparticles," *Advanced Materials*, vol. 19, no. 22, pp. 3932–3936, 2007. DOI:10.1002/adma.200700091

[18] L. Zonghuan, P. Malcolm, G. Zhanhu, G. Vladimir, C. Kumar, and L. Yuri, "Magnetic switch of permeability for polyelectrolyte microcapsules embedded with nanoparticles," *Langmuir*, vol. 21, no. 5, pp. 2042–2050, 2005. DOI:10.1021/la047629q

[19] J. Kost, J. Wolfrum, and R. Langer, "Magnetically enhanced insulin release in diabetic rats," *Journal of Biomedical Materials Research*, vol. 21, no. 12, pp. 1367–1373, 1987. DOI:10.1002/jbm.820211202

[20] A. E. Dunn, D. J. Dunn, M. Lim, C. Boyer, and N. T. K. Thanh, *Recent developments in the design of nanomaterials for photothermal and magnetic hyperthermia induced controllable drug delivery.* The Royal Society of Chemistry, 2013, vol. 63.

[21] J. Carrey, B. Mehdaoui, and M. Respaud, "Simple models for dynamic hysteresis loop calculations of magnetic single-domain nanoparticles: Application to magnetic hyperthermia optimization," *Journal of Applied Physics*, vol. 109, no. 8, 083921, 2011. DOI:10.1063/1.3551582

[22] E. Myrovali, N. Maniotis, T. Samaras, and M. Angelakeris, "Spatial focusing of magnetic particle hyperthermia," *Nanoscale Advances*, vol. 2, pp. 408–416, 2020. DOI:10.1039/C9NA00667B

[23] K. Murase, M. Aoki, N. Banura, K. Nishimoto, A. Mimura, T. Kuboyabu, I. Yabata *et al.*, "Usefulness of magnetic particle imaging for predicting the therapeutic effect of magnetic hyperthermia," *Open Journal of Medical Imaging*, vol. 5, no. 02, pp. 85–99, 2015. DOI:10.4236/ojmi.2015.52013

[24] C. Stehning, B. Gleich, and J. Rahmer, "Simultaneous magnetic particle imaging (mpi) and temperature mapping using multi-color mpi," *International Journal on Magnetic Particle Imaging*, vol. 2, no. 2, 2016. DOI:10.18416/ijmpi.2016.1612001

[25] S. Healy, A. F. Bakuzis, P. W. Goodwill, A. Attaluri, J. W. M. Bulte, and R. Ivkov, "Clinical magnetic hyperthermia requires integrated magnetic particle imaging," *Wiley interdisciplinary reviews. Nanomedicine and Nanobiotechnology*, vol. 14, no. 3, e1779, 2022. DOI:10.1002/wnan.1779

[26] I. Rubia-Rodríguez, A. Santana-Otero, S. Spassov, E. Tombácz, C. Johansson, P. De La Presa, F. J. Teran, M. d. P. Morales, S. Veintemillas-Verdaguer, N. T. K. Thanh, M. O. Besenhard, C. Wilhelm, F. Gazeau, Q. Harmer, E. Mayes, B. B. Manshian, S. J. Soenen, Y. Gu, A. Millan, E. K. Efthimiadou, J. Gaudet, P. Goodwill, J. Mansfield, U. Steinhoff, J. Wells, F. Wiekhorst, and D. Ortega, "Whither magnetic hyperthermia? a tentative roadmap," *Materials*, vol. 14, no. 4, 2021. DOI:10.3390/ma14040706

[27] E. R. Kandel, J. H. Schwartz, T. M. Jessell, S. Siegelbaum, A. J. Hudspeth, S. Mack *et al.*, *Principles of Neural Science*. McGraw-Hill New York, Health Professions Division, 2000, vol. 4.

[28] I. T. Papademetriou and T. Porter, "Promising approaches to circumvent the blood–brain barrier: progress, pitfalls and clinical prospects in brain cancer," *Therapeutic Delivery*, vol. 6, no. 8, pp. 989–1016, 2015. DOI:10.4155/tde.15.48

[29] S. N. Tabatabaei, H. Girouard, A. S. Carret, and S. Martel, "Remote control of the permeability of the blood–brain barrier by magnetic heating of nanoparticles: a proof of concept for brain drug delivery," *Journal of Controlled Release*, vol. 206, pp. 49–57, 2015. DOI:10.1016/j.jconrel.2015.02.027

[30] E. A. Kiyatkin and H. S. Sharma, "Permeability of the blood–brain barrier depends on brain temperature," *Neuroscience*, vol. 161, no. 3, pp. 926–939, 2009. DOI:10.1016/j.neuroscience.2009.04.004

[31] F. K. van Landeghem, K. Maier-Hauff, A. Jordan, K.-T. Hoffmann, U. Gneveckow, R. Scholz, B. Thiesen, W. Brück, and A. von Deimling, "Post-mortem studies in glioblastoma patients treated with thermotherapy using magnetic nanoparticles," *Biomaterials*, vol. 30, no. 1, pp. 52–57, 2009. DOI:10.1016/j.biomaterials.2008.09.044

[32] P. F. Thomsen and E. Willerslev, "Environmental dna–an emerging tool in conservation for monitoring past and present biodiversity," *Biological Conservation*, vol. 183, pp. 4–18, 2015. DOI:10.1016/j.biocon.2014.11.019

[33] N. Sheikov, N. McDannold, S. Sharma, and K. Hynynen, "Effect of focused ultrasound applied with an ultrasound contrast agent on the tight junctional integrity of the brain microvascular endothelium," *Ultrasound in Medicine & Biology*, vol. 34, no. 7, pp. 1093–1104, 2008. DOI:10.1016/j.ultrasmedbio.2007.12.015

[34] P. Prentice, A. Cuschieri, K. Dholakia, M. Prausnitz, and P. Campbell, "Membrane disruption by optically controlled microbubble cavitation," *Nature Physics*, vol. 1, no. 2, pp. 107–110, 2005. DOI:10.1038/s41467-019-09704-x

[35] P. Schlett, S. Mottaghi, O. Buchholz, and U. G. Hofmann, "First steps towards localized opening of the Blood-Brain-Barrier by IR laser illumination through the rodent skull," *Current Directions in Biomedical Engineering*, vol. 5, no. 1, pp. 211–214, 2019. DOI:10.1515/cdbme-2019-0054

[36] T. Knopp and T. M. Buzug, *Magnetic Particle Imaging: An Introduction to Imaging Principles and Scanner Instrumentation.* Springer Berlin Heidelberg, 2012.

[37] C. R. Sullivan and R. Y. Zhang, "Simplified design method for litz wire," 2014, pp. 2667–2674. DOI:10.1109/APEC.2014.6803681

[38] O. Bishop, "5-inductance," in *Understand Electronics (Second Edition)*, second edition ed., O. Bishop, Ed. Oxford: Newnes, 2001, pp. 49–57. DOI:10.1016/B978-075065319-0/50006-9

[39] J. Weizenecker, B. Gleich, J. Rahmer, H. Dahnke, and J. Borgert, "Three-dimensional real-time in vivo magnetic particle imaging," *Phys. Med. Biol.*, vol. 54, no. 5, pp. L1–L10, Mar. 2009. DOI:10.1088/0031-9155/54/5/L01

[40] M. G. Harisinghani, J. Barentsz, P. F. Hahn, W. M. Deserno, S. Tabatabaei, C. H. van de Kaa, J. de la Rosette, and R. Weissleder, "Noninvasive detection of clinically occult lymph-node metastases in prostate cancer," *New England Journal of Medicine*, vol. 348, no. 25, pp. 2491–2499, 2003, pMID: 12815134. DOI:10.1056/NEJMoa022749

[41] A. C. Bakenecker, M. Ahlborg, C. Debbeler, C. Kaethner, T. M. Buzug, and K. Lüdtke-Buzug, "Magnetic particle imaging in vascular medicine," *Innovative Surgical Sciences*, vol. 3, no. 3, pp. 179–192, 2018. DOI:10.1515/iss-2018-2026

[42] J. Haegele, J. Rahmer, B. Gleich, J. Borgert, H. Wojtczyk, N. Panagiotopoulos, T. M. Buzug, J. Barkhausen, and F. M. Vogt, "Magnetic particle imaging: Visualization of instruments for cardiovascular intervention," *Radiology*, vol. 265, no. 3, pp. 933–938, 2012, pMID: 22996744. DOI:10.1148/radiol.12120424

[43] Z. W. Tay, P. Chandrasekharan, B. D. Fellows, I. R. Arrizabalaga, E. Yu, M. Olivo, and S. M. Conolly, "Magnetic particle imaging: An emerging modality with prospects in diagnosis, targeting and therapy of cancer," *Cancers*, vol. 13, no. 21, 2021. DOI:10.3390/cancers13215285

[44] B. Zheng, T. Vazin, W. Yang, P. W. Goodwill, E. U. Saritas, L. R. Croft, D. V. Schaffer, and S. M. Conolly, "Quantitative stem cell imaging with magnetic particle imaging," in *2013 International Workshop on Magnetic Particle Imaging (IWMPI)*, 2013, pp. 1–1. DOI:10.1109/IWMPI.2013.6528323

[45] J. Borgert, J. D. Schmidt, I. Schmale, C. Bontus, B. Gleich, B. David, J. Weizenecker, J. Jockram, C. Lauruschkat, O. Mende, M. Heinrich, A. Halkola, J. Bergmann, O. Woywode, and J. Rahmer, "Perspectives on clinical magnetic particle imaging," *Biomedizinische Technik/Biomedical Engineering*, vol. 58, no. 6, pp. 551–556, 2013. DOI:10.1515/bmt-2012-0064

[46] T. Knopp, N. Gdaniec, and M. Möddel, "Magnetic particle imaging: from proof of principle to preclinical applications," *Physics in Medicine and Biology*, vol. 62, no. 14, pp. R124–R178, 2017. DOI:10.1088/1361-6560/aa6c99

[47] W. T. Coffey and Y. P. Kalmykov, *The Langevin Equation*, 3rd ed. World Scientific, 2012.

[48] T. Knopp and T. M. Buzug, *Magnetic Particle Imaging: An Introduction to Imaging Principles and Scanner Instrumentation*. Berlin, Heidelberg: Springer Berlin Heidelberg, 2012, pp. 11–70. DOI:10.1007/978-3-642-04199-0-2

[49] M. Palazzi, S. Maluta, S. Dall'Oglio, and M. Romano, "The role of hyperthermia in the battle against cancer," *Tumori*, vol. 96, no. 6, pp. 902–910, 2010. DOI:10.1177/548.6507

[50] R. K. Gilchrist, R. Medal, W. D. Shorey, R. C. Hanselman, J. C. Parrott, and C. B. Taylor, "Selective inductive heating of lymph nodes," *Annals of Surgery*, vol. 146, no. 4, pp. 596–606, 1957. DOI:10.1097/00000658-195710000-00007

[51] E. A. Périgo, G. Hemery, O. Sandre, D. Ortega, E. Garaio, F. Plazaola, and F. J. Teran, "Fundamentals and advances in magnetic hyperthermia," *Applied Physics Reviews*, vol. 2, no. 4, 041302, 2015. DOI:10.1063/1.4935688

[52] R. Hergt, W. Andra, C. G. D'Ambly, I. Hilger, and H. G. Schmidt, "Physical limits of hyperthermia using magnetite fine particles," *IEEE Transactions on Magnetics*, vol. 34, no. 5, pp. 3745–3754, 1998. DOI:10.1109/20.718537

[53] L. Néel, "Théorie du traînage magnétique des ferromagnétiques en grains fins avec applications aux terres cuites," *Annales Geophysicae*, vol. 5, pp. 99–136, 1949.

[54] W. F. Brown Jr, "Thermal fluctuations of a single-domain particle," *Physical Review*, vol. 130, no. 5, pp. 1677–1686, 1963. DOI:10.1103/PhysRev.130.1677

[55] R. J. Deissler, Y. Wu, and M. A. Martens, "Dependence of brownian and néel relaxation times on magnetic field strength," *Medical Physics*, vol. 41, no. 1, 012301, 2014. DOI:10.1118/1.4837216

[56] R. E. Rosensweig, "Heating magnetic fluid with alternating magnetic field," *Journal of Magnetism and Magnetic Materials*, vol. 252, pp. 370–374, 2002. DOI:10.1016/S0304-8853(02)00706-0

[57] P. Gas and A. Miaskowski, "Specifying the ferrofluid parameters important from the viewpoint of magnetic fluid hyperthermia," in *2015 Selected Problems of Electrical Engineering and Electronics (WZEE)*, 2015, pp. 1–6. DOI:10.1109/WZEE.2015.7394040

[58] M. Graeser, T. Knopp, P. Szwargulski, T. Friedrich, A. von Gladiss, M. Kaul, K. M. Krishnan, H. Ittrich, G. Adam, and T. M. Buzug, "Towards picogram detection of superparamagnetic Iron-Oxide particles using a gradiometric receive coil," *Scientific Reports*, vol. 7, no. 1, 6872, 2017. DOI:10.1038/s41598-017-06992-5

[59] R. Almeida, B. Manadas, C. Melo, J. Gomes, C. Mendes, M. Graos, R. Carvalho, A. Carvalho, and C. Duarte, "Neuroprotection by bdnf against glutamate-induced apoptotic cell death is mediated by erk and pi3-kinase pathways," *Cell Death & Differentiation*, vol. 12, no. 10, pp. 1329–1343, 2005. DOI:10.1038/sj.cdd.4401662

[60] A. Jordan, R. Scholz, K. Maier-Hauff, F. K. van Landeghem, N. Waldoefner, U. Teichgraeber, J. Pinkernelle, H. Bruhn, F. Neumann, B. Thiesen *et al.*, "The effect of thermotherapy using magnetic nanoparticles on rat malignant glioma," *Journal of Neuro-Oncology*, vol. 78, no. 1, pp. 7–14, 2006. DOI:10.1007/s11060-005-9059-z

[61] M. Abdel-Basset, L. Abdel-Fatah, and A. K. Sangaiah, "Chapter 10 - metaheuristic algorithms: A comprehensive review," in *Computational Intelligence for Multimedia Big Data on the Cloud with Engineering Applications*. Academic Press, 2018, pp. 185–231.

[62] K. Hussain, M. Salleh, S. Cheng, and R. Naseem, "Common benchmark functions for metaheuristic evaluation: A review," *International Journal on Informatics Visualization*, vol. 1, pp. 218–223, 2017. DOI:10.30630/joiv.1.4-2.65

[63] J. Kennedy and R. Eberhart, "Particle swarm optimization," in *Proceedings of ICNN'95-International Conference on Neural Networks*, vol. 4. IEEE, 1995, pp. 1942–1948. DOI:10.1109/ICNN.1995.488968

[64] D. Wang, D. Tan, and L. Liu, "Particle swarm optimization algorithm: an overview," *Soft Computing*, vol. 22, no. 2, pp. 387–408, 2018. DOI:10.1007/s00500-016-2474-6

[65] W. Hu and Z. S. Li, "A simpler and more effective particle swarm optimization algorithm," *Journal of Software*, vol. 18, no. 4, pp. 861–868, 2007. DOI:10.1360/JOS180861

[66] W. N. Chen, J. Zhang, Y. Lin, N. Chen, Z. H. Zhan, H. S. H. Chung, Y. Li, and Y. H. Shi, "Particle swarm optimization with an aging leader and challengers," *IEEE Transactions on Evolutionary Computation*, vol. 17, no. 2, pp. 241–258, 2012. DOI:10.1109/TEVC.2011.2173577

[67] R. Storn and K. Price, "Differential evolution–a simple and efficient heuristic for global optimization over continuous spaces," *Journal of Global Optimization*, vol. 11, no. 4, pp. 341–359, 1997. DOI:10.1023/A:1008202821328

[68] M. F. Ahmad, N. A. M. Isa, W. H. Lim, and K. M. Ang, "Differential evolution: A recent review based on state-of-the-art works," *Alexandria Engineering Journal*, vol. 61, no. 5, pp. 3831–3872, 2022. DOI:10.1016/j.aej.2021.09.013

[69] W. J. Zhang and X. F. Xie, "Depso: hybrid particle swarm with differential evolution operator," in *SMC'03 Conference Proceedings. 2003 IEEE International Conference on Systems, Man and Cybernetics. Conference Theme - System Security and Assurance (Cat. No.03CH37483)*, vol. 4, 2003, pp. 3816–3821 vol.4. DOI:10.1109/ICSMC.2003.1244483

[70] S. Agrawal, B. K. Panigrahi, and M. K. Tiwari, "Multiobjective particle swarm algorithm with fuzzy clustering for electrical power dispatch," *IEEE Transactions on Evolutionary Computation*, vol. 12, no. 5, pp. 529–541, 2008. DOI:10.1109/TEVC.2007.913121

[71] D. C. Meeker and M. Priboianu, "Finite element method magnetics," 2002. [Online]. Available: https://api.semanticscholar.org/CorpusID:124678764

[72] R. Crozier and M. Mueller, "A new matlab and octave interface to a popular magnetics finite element code," in *2016 XXII International Conference on Electrical Machines (ICEM)*, 2016, pp. 1251–1256. DOI:10.1109/ICELMACH.2016.7732685

[73] A. Gefen, N. Gefen, Q. Zhu, R. Raghupathi, and S. S. Margulies, "Age-dependent changes in material properties of the brain and braincase of the rat," *Journal of Neurotrauma*, vol. 20, no. 11, pp. 1163–1177, 2003, pMID: 14651804. DOI:10.1089/089771503770802853

[74] Z. Boekelheide, Z. A. Hussein, and S. Hartzell, "Electronic measurements in an alternating magnetic field for studying magnetic nanoparticle

hyperthermia: Minimizing eddy current heating," *IEEE Transactions on Magnetics*, vol. 52, no. 7, pp. 1–4, 2016. DOI:10.1109/TMAG.2016.2515051

[75] D. Hensley, Z. W. Tay, R. Dhavalikar, B. Zheng, P. Goodwill, C. Rinaldi, and S. Conolly, "Combining magnetic particle imaging and magnetic fluid hyperthermia in a theranostic platform," *Physics in Medicine & Biology*, vol. 62, no. 9, 3483, 2017. DOI:10.1088/1361-6560/aa5601

[76] F. Soetaert, S. K. Kandala, A. Bakuzis, and R. Ivkov, "Experimental estimation and analysis of variance of the measured loss power of magnetic nanoparticles," *Scientific Reports*, vol. 7, no. 1, 6661, 2017. DOI:10.1038/s41598-017-07088-w

[77] D. Zahn, J. Landers, J. Buchwald, M. Diegel, S. Salamon, R. Müller, M. Köhler, G. Ecke, H. Wende, and S. Dutz, "Ferrimagnetic large single domain iron oxide nanoparticles for hyperthermia applications," *Nanomaterials*, vol. 12, no. 3, 2022. DOI:10.3390/nano12030343

[78] V. Narayanaswamy, I. A. Al-Omari, A. S. Kamzin, B. Issa, and I. M. Obaidat, "Tailoring interfacial exchange anisotropy in hard-soft core-shell ferrite nanoparticles for magnetic hyperthermia applications," *Nanomaterials*, vol. 12, no. 2, 2022. DOI:10.3390/nano12020262

[79] O. A. Kulikov, M. N. Zharkov, V. P. Ageev, D. E. Yakobson, V. I. Shlyapkina, A. V. Zaborovskiy, V. I. Inchina, L. A. Balykova, A. M. Tishin, G. B. Sukhorukov, and N. A. Pyataev, "Magnetic hyperthermia nanoarchitectonics via iron oxide nanoparticles stabilised by oleic acid: Anti-tumour efficiency and safety evaluation in animals with transplanted carcinoma," *International Journal of Molecular Sciences*, vol. 23, no. 8, 2022. DOI:10.3390/ijms23084234

[80] S. Vaalma, J. Rahmer, N. Panagiotopoulos, R. L. Duschka, J. Borgert, J. Barkhausen, F. M. Vogt, and J. Haegele, "Magnetic particle imaging (mpi): Experimental quantification of vascular stenosis using stationary stenosis phantoms," *PLOS ONE*, vol. 12, no. 1, pp. 1–22, 2017. DOI:https://doi.org/10.1371/journal.pone.0168902

[81] D. Eberbeck, F. Wiekhorst, S. Wagner, and L. Trahms, "How the size distribution of magnetic nanoparticles determines their magnetic particle imaging performance," *Applied Physics Letters*, vol. 98, no. 18, 182502, 2011. DOI:10.1063/1.3586776

[82] Y. Yan, P. Zhou, H. Wang, and Y. Mao, "Thermal effect on poly(methyl methacrylate) (pmma) material removal in the micromilling process," *Polymers*, vol. 12, no. 9, 2020. DOI:10.3390/polym12092122

[83] A. A. Abdel-Wahab, S. Ataya, and V. V. Silberschmidt, "Temperature-dependent mechanical behaviour of pmma: Experimental analysis and modelling," *Polymer Testing*, vol. 58, pp. 86–95, 2017. DOI:10.1016/j.polymertesting.2016.12.016

[84] K. Sajjamark, J. Franke, H. Lehr, R. Pietig, and V. Niemann, "Spatial selectivity enhancement in magnetic fluid hyperthermia by magnetic flux confinement," *International Journal on Magnetic Particle Imaging*, vol. 7, no. 1, 2021. DOI:10.18416/IJMPI.2021.2103002

[85] Z. W. Tay, P. Chandrasekharan, A. Chiu-Lam, D. W. Hensley, R. Dhavalikar, X. Y. Zhou, E. Y. Yu, P. W. Goodwill, B. Zheng, C. Rinaldi, and S. M. Conolly, "Magnetic particle imaging-guided heating in vivo using gradient fields for arbitrary localization of magnetic hyperthermia therapy," *ACS nano*, vol. 12, no. 4, pp. 3699–3713, 2018. DOI:10.1021/acsnano.8b00893

[86] J. Wells, S. Twamley, A. Sekar, A. Ludwig, H. Paysen, O. Kosch, and F. Wiekhorst, "Lissajous scanning magnetic particle imaging as a multifunctional platform for magnetic hyperthermia therapy," *Nanoscale*, vol. 12, no. 35, pp. 18 342–18 355, 2020. DOI:10.1039/D0NR00604A

[87] P. W. Goodwill, G. C. Scott, P. P. Stang, and S. M. Conolly, "Narrowband magnetic particle imaging," *IEEE Transactions on Medical Imaging*, vol. 28, no. 8, pp. 1231–1237, 2009. DOI:10.1109/TMI.2009.2013849

[88] H. H. Pennes, "Analysis of tissue and arterial blood temperatures in the resting human forearm," *Journal of Applied Physiology*, vol. 1, no. 2, pp. 93–122, 1948. DOI:10.1152/jappl.1948.1.2.93

[89] M. M. Elwassif, Q. Kong, M. Vazquez, and M. Bikson, "Bio-heat transfer model of deep brain stimulation-induced temperature changes," *Journal of Neural Engineering*, vol. 3, no. 4, pp. 306–315, 2006. DOI:10.1088/1741-2560/3/4/008

[90] H. P. Kok, J. Gellermann, C. A. van den Berg, P. R. Stauffer, J. W. Hand, and J. Crezee, "Thermal modelling using discrete vasculature for thermal

therapy: A review," *International Journal of Hyperthermia*, vol. 29, no. 4, pp. 336–345, 2013. DOI:10.3109/02656736.2013.801521

[91] T. A. Le, M. P. Bui, and J. Yoon, "Theoretical analysis for wireless magnetothermal deep brain stimulation using commercial nanoparticles," *International Journal of Molecular Sciences*, vol. 20, no. 12, 2019. DOI:10.3390 /ijms20122873

[92] L. R. John, "Forward electrical transmission line model of the human arterial system," *Medical & Biological Engineering & Computing*, vol. 42, no. 3, pp. 312–321, 2004. DOI:10.1007/BF02344705

[93] Y. Lutz, R. Daschner, L. Krames, A. Loewe, O. Dössel, and G. Cattaneo, "Estimating local therapeutic hypothermia in case of ischemic stroke using a 1d hemodynamics model and an energetic temperature model," in *2019 41st Annual International Conference of the IEEE Engineering in Medicine and Biology Society (EMBC)*, 2019, pp. 3983–3986. DOI:10.1109/EMBC.2019.8856447

[94] L. Zarrinkoob, K. Ambarki, A. Wåhlin, R. Birgander, A. Eklund, and J. Malm, "Blood flow distribution in cerebral arteries," *J. Cereb. Blood Flow Metab.*, vol. 35, no. 4, pp. 648–654, Mar. 2015. DOI:10.1038/jcbfm.2014.241

[95] O. Buchholz, K. Sajjamark, J. Franke, H. Wei, A. Behrends, C. Münkel, C. Grüttner, P. Levan, D. von Elverfeldt, M. Graeser, T. Buzug, S. Bär, and U. G. Hofmann, "In situ theranostic platform combining highly localized magnetic fluid hyperthermia, magnetic particle imaging, and thermometry in 3d," *Theranostics*, vol. 14, pp. 324–340, 2024. DOI:10.7150/thno.86759

[96] O. Buchholz, S. Bär, J. Franke, H. Wei, C. Münkel, and U. G. Hofmann, "Theranostics based on mpi for brain interventions: an in vivo pilot study," *International Journal on Magnetic Particle Imaging*, vol. 10, no. 1 suppl 1, 2024, to appear.

[97] G. P. Skandalakis, D. R. Rivera, C. D. Rizea, A. Bouras, J. G. Jesu Raj, D. Bozec, and C. G. Hadjipanayis, "Hyperthermia treatment advances for brain tumors," *International Journal of Hyperthermia*, vol. 37, no. 2, pp. 3–19, 2020. DOI:10.1080/02656736.2020.1772512

[98] A. Matsumine, K. Takegami, K. Asanuma, T. Matsubara, T. Nakamura, A. Uchida, and A. Sudo, "A novel hyperthermia treatment for bone

metastases using magnetic materials," *International journal of clinical oncology*, vol. 16, no. 2, pp. 101–108, 2011. DOI:10.1007/s10147-011-0217-3

[99] M. B. Lodi, A. Fanti, G. Muntoni, and G. Mazzarella, "A multiphysic model for the hyperthermia treatment of residual osteosarcoma cells in upper limbs using magnetic scaffolds," *IEEE Journal on Multiscale and Multiphysics Computational Techniques*, vol. 4, pp. 337–347, 2019. DOI:10.1109/JMMCT.2019.2959585

[100] F. Zhang, C. L. Xu, and C. M. Liu, "Drug delivery strategies to enhance the permeability of the blood-brain barrier for treatment of glioma," *Drug design, development and therapy*, vol. 9, pp. 2089–2100, 2015. DOI:10.2147/DDDT.S79592

[101] F. Dilnawaz and S. K. Sahoo, "Therapeutic approaches of magnetic nanoparticles for the central nervous system," *Drug discovery today*, vol. 20, no. 10, pp. 1256–1264, 2015. DOI:10.1016/j.drudis.2015.06.008

List of abbreviations

AC alternating current
ADC analog to digital convertor
AMF alternating magnetic field
BBB blood brain barrier
BPF band-pass filter
CAD computer-aided design
CT computed tomography
DC direct current
ESL equivalent series inductance
ESR equivalent series resistance
FEM finite element method
FFL field-free line
FFP field-free point
FFR field-free region
FFT fast Fourier transform
FOV field of view
FWHM full width at half maximum
GBM glioblastoma
IR infrared
LNA low-noise amplifier
LDU large device unit
LPF low-pass filter
LRT linear response theory
MFH magnetic fluid hyperthermia
MPI magnetic particle imaging
MPS magnetic particle spectrometry
MRI magnetic resonance imaging
MNP magnetic nanoparticle
NWA network analyzer
PEEK polyetheretherketone
PMMA polymethyl methacrylate
POM polyoxymethylene
PSO particle swarm optimizazion
RF radio frequency
RMS root mean square
RTD resistance temperature detector
SAR specific absorption rate
SLA stereolithography
UV ultraviolet